Magneto-optical spectroscopy and coherent Raman studies of dilute magnetic semiconductors

Smith, Lowenna

Award date:
2007

Awarding institution:
University of Bath

MAGNETO-OPTICAL SPECTROSCOPY AND COHERENT RAMAN STUDIES OF DILUTE MAGNETIC SEMICONDUCTORS

Submitted by Lowenna Smith, University of Bath

for the degree of

Doctor of Philosophy

University of Bath

Department of Physics

December 2007

ProQuest LLC
789 East Eisenhower Parkway
P.O. Box 1346
Ann Arbor, MI 48106-1346

Abstract

Coherent Raman electron spin resonance (CRESR) and magneto-optical spectroscopy have been used to investigate the properties of diluted magnetic semiconductors, with particular focus on $Cd_{1-x}Mn_xTe$ based heterostructures. CRESR is a novel technique: incorporating the optical site selective nature and high sensitivity of spin-flip Raman spectroscopy (SFRS) with the high energy resolution of electron spin resonance (ESR). Initial characterisation of the samples is achieved using magneto-photoluminescence and -photoluminescence excitation spectroscopy. For example, the energy position of the excitonic states is obtained in good agreement with the literature and calculations. In bulk $Cd_{1-x}Mn_xTe$, if the excitation energy is tuned into resonance with these states, a range of spin-flip Raman signals are observed: conduction band electron spin-flip (ESF); electron paramagnetic resonance (PMR); and nearest & next nearest neighbour antiferromagnetically aligned Mn^{2+} pairs. In $Cd_{1-x}Mn_xTe/Cd_{1-x-y}Mn_xMg_yTe$ single quantum wells, nPMR spin-flip Raman signals are observed, originating from multiple simultaneous spin-flips within the ground state Zeeman multiplet of Mn^{2+} ions. Here, the number (n) of overtones as a function of angle, between the external magnetic field and the growth direction, is found to be consistent with theoretical predictions.

The core work of this thesis is the detection of Mn^{2+} electron paramagnetic resonance by CRESR. Coherent Raman signals are seen in optical resonance with free or weakly bound excitons, via the *sp-d* exchange interaction, in both bulk $Cd_{1-x}Mn_xTe$ and $Cd_{1-x}Mn_xTe/Cd_{1-x-y}Mn_xMg_yTe$ single quantum wells. In the former case, contributions from the hyperfine interaction (between the Mn^{2+} $3d^5$ electrons and the Mn^{2+} nucleus) and the cubic crystal field are resolvable. The observed deviations from the conventional Lorentzian lineshape are successfully explained by modulation and microwave resonant heating effects. With the CRESR setup, secondary signals can be detected: attributed to microwave-modulated magneto-reflectivity (MMMR). MMMR spectra are obtained for both CdTe and GaAs based structures.

Acknowledgements

I would like to begin by thanking Dr Daniel Wolverson and Prof John Davies for all their help and encouragement. In addition to the past and present members of the Optical Spectroscopy group, Dr Stephen Bingham, Dr Gazi Aliev and Dr Shanshan Zeng; it has been a lovely group to be a member of. Whilst not forgetting Harry Bone for all his assistance in the lab.

I would also like to thank everyone in Würzburg who made me feel so welcome during my two visits, and who have helped me in my research. In particular, I wish to thank Michael Lentze and Prof Jean Geurts.

Finally, I'd like to say a general thank you to my friends, family and Mark.

Contents

Chapter 1

Introduction to semiconductors and DMS

The first part of this chapter introduces the key electronic and magnetic properties of the main semiconductors investigated during this work. Section 1.1 begins by describing the physical traits of the semiconductor CdTe. This section forms an important basis for understanding the subsequent section (1.2) on diluted magnetic semiconductors (DMS) since CdTe is the host material for many of these ternary materials. The last part of the chapter gives a brief introduction into the field of spintronics (section 1.3): an important application for DMS.

1.1 Properties of CdTe

Cadmium telluride [1] is a well established II-VI compound semiconductor, with the first report of crystalline growth in 1947 [2]. Bulk CdTe is stable in the zinc-blende configuration. This is a cubic structure, where each atom is surrounded tetrahedrally by four atoms from the opposing group. At room temperature, it has a cubic lattice parameter of 6.481 Å [3]. The electronic structures of Cd and Te are $4d^{10}5s^2$ and $4d^{10}5s^25p^4$ respectively. Tetrahedral s-p^3 bonding is formed from the valence s electrons from Cd and the valence p electrons from Te.

The electronic band structure of CdTe is shown in Fig. 1.1. The conduction band

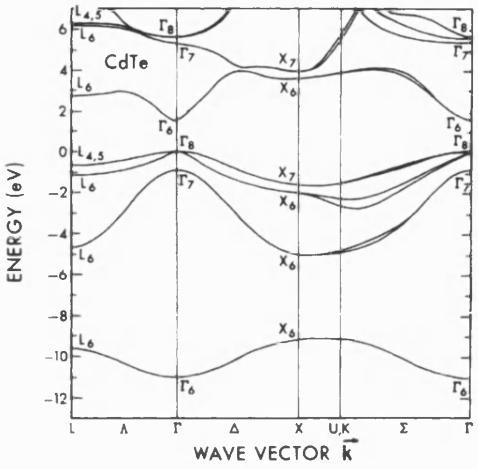

Figure 1.1: Electronic band structure (schematic) of CdTe. Taken from Ref. [4].

(CB) and valance band (VB) originate from the s and p states. CdTe is a direct-bandgap semiconductor and has the band extrema (CB and VB) positioned at the Γ point of the Brillouin zone. The valence band is sixfold degenerate: fourfold degenerate light- and heavy-hole band (Γ_8 symmetry); and twofold degenerate spin split-off band (Γ_7 symmetry). The conduction band is twofold degenerate, with Γ_6 symmetry. The bandgap energy ($E(\Gamma_8) - E(\Gamma_6)$) and the free exciton energy are equal to 1.606 eV [5, 6] and 1.596 eV [7] respectively; hence, the exciton binding energy is 10 meV. In CdTe, the effective masses (for k along 100) of the conduction band electron and the valence heavy- and light-holes, are $m_e/m_0 = 0.096$, $m_{hh}/m_0 = 0.81$ and $m_{lh}/m_0 = 0.12$ [8] respectively. It is common for the effective mass of holes to be expressed in terms of the Luttinger parameters γ_1 and γ_2: $m_0/m_{hh} = \gamma_1 - 2\gamma_2$ and $m_0/m_{lh} = \gamma_1 + 2\gamma_2$. For CdTe $\gamma_1 = 4.78$ and $\gamma_2 = 1.77$. The effective mass of carriers can be understood using $\mathbf{k} \cdot \mathbf{p}$ perturbation theory (appendix A).

The spin degeneracy of an electron is lifted in the presence of a magnetic field (the Zeeman effect). The energy difference between the two spin states ($m_S \pm 1/2$) is

$$\Delta E = g\mu_B B, \tag{1.1}$$

where g is the gyromagnetic ratio (g factor), μ_B is the Bohr magneton and B is the magnetic field. The Landé g factor is given by

$$g_0 = \frac{3}{2} + \frac{S(S+1) - L(L+1)}{2J(J+1)}, \tag{1.2}$$

where S, L and J are the spin, orbital and total angular momentum respectively. For free electrons ($L = 0$, $S = J = 1/2$) this is equal to $g_0 = 2$[1]. However, analogous to the effective mass, carriers in semiconductors have an effective g factor, which alters from 2 due to spin-orbit interactions. For an electron the g factor can deviate significantly from 2, and in some cases become negative. The isotropic g factor is effectively described by five-level $\mathbf{k} \cdot \mathbf{p}$ perturbation theory (appendix A). Current literature gives the following values for the conduction band electron g factor in CdTe: $g = -1.644 \pm 0.005$, spin-flip Raman spectroscopy [9]; $g = -1.676 \pm 0.007$, spin-flip Raman spectroscopy [10]; $g = -1.6803 \pm 0.0005$, electron spin resonance [11].

1.2 Diluted magnetic semiconductors

Diluted magnetic semiconductors [12] (DMS), or semimagnetic semiconductors, are compound semiconductors with magnetic ions occupying a proportion of the cation sites. They are characterised by a strong exchange interaction between the magnetic ions' electrons and the band carriers, which gives rise to a giant Zeeman splitting of the conduction and valence bands. The most extensively studied DMS take the form $A^{II}_{1-x}Mn_xTe^{VI}$, for example $Cd_{1-x}Mn_xTe$, $Cd_{1-x}Mn_xSe$, $Hg_{1-x}Mn_xTe$. Mn is a popular choice of magnetic ion, because samples with high ion concentrations can be grown. However, other transition metal ions have also been successfully incorporated, such as Co [13], Fe, V [10] and Cr. Recently, in addition to the II-VI ternaries, there has been great interest in the III-V ternaries, e.g. $Ga_{1-x}Mn_xAs$. This is due in part to their application to spintronics (section 1.3), where the spin as well as the charge of carriers is exploited. The work presented in this thesis primarily focuses on the archetypal DMS $Cd_{1-x}Mn_xTe$, therefore sections 1.2.1 and 1.2.2 use this material to demonstrate the electronic and magnetic properties of DMS.

[1] In fact the experimental value of the free electron g factor is slightly above 2, because it is the electron-photon moment which is measured.

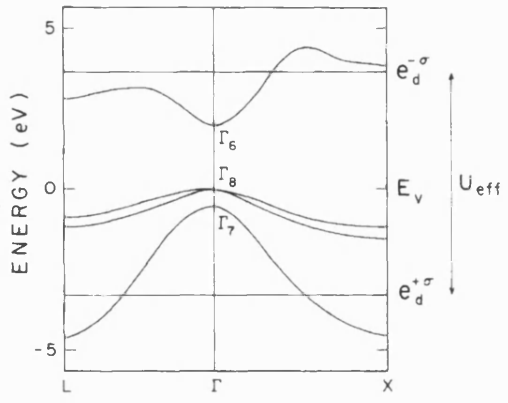

Figure 1.2: Band structure (schematic) of zinc-blende $A^{II}_{1-x}Mn_xTe^{VI}$ taken from Ref. [12]. The lines labeled $e_d^{+\sigma}$ and $e_d^{-\sigma}$ refer to the position of the occupied and unoccupied Mn $3d$ levels respectively.

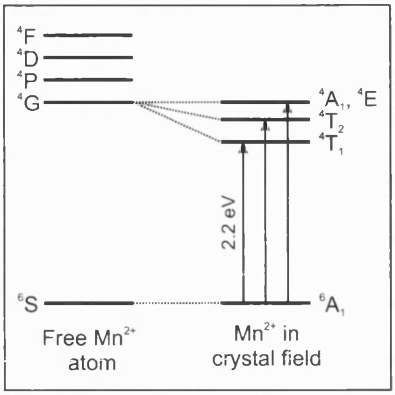

Figure 1.3: Schematic of the energy levels of the Mn^{2+} $3d^5$ shell in $Cd_{1-x}Mn_xTe$. The arrows indicate the intra-Mn transitions. Adapted from from Ref. [12]

1.2.1 Electronic properties of DMS

$Cd_{1-x}Mn_xTe$ has a composition range of $0 < x \leq 0.77$, and like its host material, CdTe, it forms a zinc-blende structure. The lattice parameter of the crystal closely follows Vegard's rule, with the mean cation-cation distance given by [14][15]

$$a = (4.587 - 0.105x)\ \text{Å}. \tag{1.3}$$

The manganese concentrations attainable are large considering that although epitaxial zinc-blende MnTe has been reported [16], MnTe naturally forms a hexagonal NiAs structure. This high ion concentration is possible because the Mn^{2+} $3d^5$ shell is exactly half filled. From Hund's rule all five spins are parallel ($S = 5/2$), so it is energetically unfavourable to add another electron of opposing spin. Therefore the $3d^5$ band is effectively a closed shell, making it easier for Mn^{2+} to replace the group II element, in this case Cd, which has a closed $4d^{10}$ shell. The group II valence s electrons and the group VI valence p electrons form tetrahedral s-p^3 bonding. Like the group II element, manganese contributes to these bonds with valence s electrons from its $4s^2$ orbital.

The band structure of $Cd_{1-x}Mn_xTe$ is shown schematically in Fig. 1.2. Like CdTe (section 1.1), it is a direct bandgap semiconductor, with the important band extrema centred at the Γ point. Superimposed on the figure are the energy levels of the majority (occupied) and minority (unoccupied) Mn^{2+} $3d^5$ states. These

are separated in energy by ≈ 7 eV. The Mn^{2+} $3d^5$ states form narrow bands due to hybridisation with the p orbitals. To a good first approximation there is a linear change in the energy gap of $Cd_{1-x}Mn_xTe$ with Mn^{2+} concentration [17]:

$$E_g(300\text{K}) = (1.528 + 1.316x)\text{ eV}, \quad (1.4)$$

$$E_g(4.2\text{K}) = (1.606 + 1.592x)\text{ eV}. \quad (1.5)$$

The first excited state of the Mn^{2+} ion is split into three levels by the tetrahedral crystal field, shown schematically in Fig. 1.3. The energy difference between the lowest of these three states ($^4T_1$) and the orbitally nondegenerate ground state ($^6A_1$) is 2.2 eV. For low Mn^{2+} concentrations this is significantly larger than the $Cd_{1-x}Mn_xTe$ bandgap.

1.2.2 Magnetic properties of DMS

This section explores the unique magnetic properties [18] of DMS that have contributed to the motivation for thirty years of extensive research.

The magnetic phase of a $A^{II}_{1-x}Mn_xTe^{VI}$ DMS is dependent upon its temperature and the concentration of magnetic ions [19]. A spin-glass (frozen) phase exists at low temperatures and (except for very low temperatures) for high magnetic ion concentrations ($x > 0.2$). At high temperatures, and/or for ion concentrations of $x < 0.2$, the material is in a paramagnetic phase. An antiferromagnetic phase has also been observed for $Cd_{0.3}Mn_{0.7}Te$. The $Cd_{1-x}Mn_xTe$ based structures used for this work have been measured whilst in the paramagnetic phase; therefore, the remainder of this section will only consider this phase.

In the dilute limit ($x < 0.01$) the magnetisation of the Mn^{2+} ions is given by

$$\begin{aligned} M &= -xN_0 g_{\text{Mn}} \mu_B \langle S_z \rangle \\ &= -xN_0 g_{\text{Mn}} \mu_B S B_S[g_{\text{Mn}} \mu_B SB/(k_B T)]. \end{aligned} \quad (1.6)$$

Here N_0 is the number of cations per unit volume, g_{Mn} is the g factor of Mn^{2+}, $\langle S_z \rangle$ is the average spin per Mn^{2+} site, $S(= 5/2)$ is the total spin angular momentum for a Mn^{2+} ion, B is the applied magnetic field, T is the temperature and B_S is

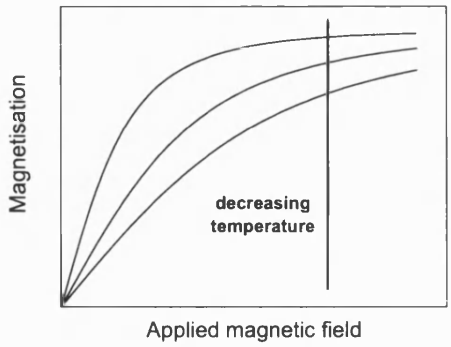

Figure 1.4: Plot of the magnetisation as a function of applied magnetic field for a range of temperatures.

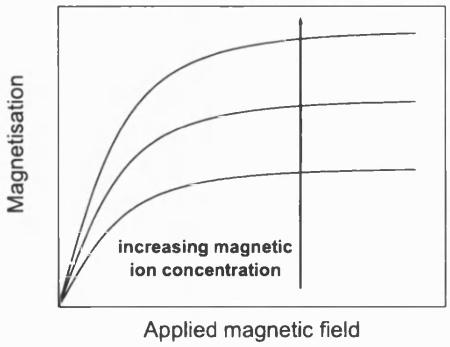

Figure 1.5: Plot of the magnetisation as a function of applied magnetic field for various ion concentrations.

the standard Brillouin function (Eq. 1.7).

$$B_S(y) = \frac{2S+1}{2S}\coth\left(\frac{2S+1}{2S}y\right) - \frac{1}{2S}\coth\left(\frac{1}{2S}y\right). \tag{1.7}$$

Away from the dilute limit, Eq. 1.6 is no longer sufficient to describe the magnetisation, due to antiferromagnetic Mn^{2+}-Mn^{2+} interactions. As the Mn^{2+} concentration increases Mn ions will start to form pairs or complexes that have no net magnetic moment, thus reducing the percentage of Mn^{2+} that contributes to the magnetisation. This is taken into account by replacing x and T with the phenomenological fitting parameters $\bar{x}$ (effective Mn^{2+} concentration) and $T_{\text{eff}} = T + T_0$ (effective temperature) to give

$$M = -\bar{x}N_0 g_{\text{Mn}}\mu_B S B_S[g_{\text{Mn}}\mu_B SB/(k_B T_{\text{eff}})]. \tag{1.8}$$

The dependence of the magnetisation on the temperature and magnetic ion concentration is shown in Fig. 1.4 and Fig. 1.5 respectively.

The magnetic properties of DMS are strongly influenced by the exchange interaction: both the *sp-d* exchange between Mn^{2+} ions and band carriers, and the *d-d* exchange between two Mn^{2+} ions. The latter Mn^{2+}-Mn^{2+} exchange interaction is a two step process mediated by the anion, i.e. *d-p-d* exchange. The nearest neighbour exchange (represented by the integral J) and the next nearest neighbour exchange (represented by the integral J_{NNN}) are both antiferromagnetic (typically $J \approx 5J_{NNN}$). The energy of states belonging to a pair of nearest

neighbour Mn^{2+} ions are given by

$$E = -J[S_T(S_T + 1) - \tfrac{35}{2}] + g_{\mathrm{Mn}}\mu_B mB. \tag{1.9}$$

Here S_T is the total spin of the pair, an integral factor from $0 \ldots 5$; the magnetic quantum number m takes integral values from $-S_T \ldots S_T$.

Evidence of nearest neighbour exchange processes can be observed at high magnetic fields ($B > 10$ T) [20, 21, 22]. $S_T = 0$ is the ground state of a pair of Mn^{2+} ions for magnetic fields up to $B_1 = -2J/g_{\mathrm{Mn}}\mu_B$, after this $S_T = 1$ & $m = -1$ takes over as the ground state, i.e. the Zeeman interaction becomes sufficiently strong to decouple the Mn^{2+} pairs. Consequently, above B_1 there will be an additional contribution to the magnetisation from the Mn^{2+} pairs. Likewise at $2B_1$, $S_T = 2$ & $m = -2$ will become the ground state, leading to a further increase in the magnetisation. In fact, there are five magnetisation steps corresponding to $S_T = 1 \ldots 5$ ($m = -1 \ldots -5$) at magnetic fields given by

$$B_n = nB_1 = -n\frac{2J}{g_{\mathrm{Mn}}\mu_B}. \tag{1.10}$$

These step like increases in the magnetisation can be used to give a direct measurement of J. Experimentally, it is observed that J_{NNN} and further neighbour exchange interactions lead to deviations from Eq. 1.9 ($B_2 < 2B_1$) [23]. Larger complexes (e.g. triples) can contribute more smaller steps in the magnetisation, although they have a lower probability of forming.

The *sp-d* exchange interaction is responsible for the giant Zeeman effects that typify DMS [24]. The exchange component of the Hamiltonian is

$$H_{\mathrm{ex}} = \sum_{\mathbf{R}_i} J^{sp-d}(\mathbf{r} - \mathbf{R}_i)\mathbf{S}_i \cdot \sigma, \tag{1.11}$$

where J^{sp-d} is *sp-d* exchange coupling constant, $\mathbf{r}$ and $\mathbf{R}_i$ are the coordinates of the band electron and the Mn^{2+} ion respectively, and $\mathbf{S}_i$ and σ are the spin operators for the Mn ion and the band electron respectively. It is possible to simplify this expression, because the electron's electronic wavefunction extends over a large number of Mn ion lattice sites, using the following two approximations. Firstly, the molecular field approximation allows $\mathbf{S}_i$ to be replaced by a thermal average taken over all Mn ions $\langle \mathbf{S} \rangle$ (for the paramagnetic system $\langle \mathbf{S} \rangle = \langle S_z \rangle$). Secondly, $J^{sp-d}(\mathbf{r} - \mathbf{R}_i)$ can be replaced by $xJ^{sp-d}(\mathbf{r} - \mathbf{R})$, where $\mathbf{R}$ is the set

of coordinates of all cation lattice sites. The exchange Hamiltonian now has the periodicity of the lattice and is given by

$$H_{\text{ex}} = \sigma_z \langle S_z \rangle x \sum_{\mathbf{R}} J^{sp-d}(\mathbf{r} - \mathbf{R}). \tag{1.12}$$

A s-like electron in a parabolic Γ_6 conduction band will have an energy of

$$E = E_g + (l + \tfrac{1}{2})\hbar\omega_c + m_s(g_e\mu_B B - N_0\alpha x\langle S_z\rangle). \tag{1.13}$$

Here E_g is the energy gap, l is the Landau level, ω_c is the cyclotron frequency, m_s ($\pm 1/2$) is the magnetic quantum number of the electron, g_e is the intrinsic g factor of the band electron (appendix A) and α is the exchange integral for the s-like electrons. As in Eq. 1.6 and Eq. 1.8, $\langle S_z \rangle$ can be replaced by a modified Brillouin function, yielding

$$E = E_g + (l + \tfrac{1}{2})\hbar\omega_c + m_s(g_e\mu_B B - N_0\alpha x_{\text{eff}} S B_S[g_{\text{Mn}}\mu_B SB/(k_B T_{\text{eff}})]). \tag{1.14}$$

Typically, $N_0\alpha x_{\text{eff}} S B_S[g_{\text{Mn}}\mu_B SB/(k_B T_{\text{eff}})] \gg g_e\mu_B B$; hence, the magnetic field induced conduction band splitting is dominated by the Brillouin term. A similar expression exists for the p-like Γ_8 valence band,

$$E = (l + \tfrac{1}{2})\hbar\omega_c + m_J(\kappa\mu_B B - \tfrac{1}{3}N_0\beta x_{\text{eff}} S B_S[g_{\text{Mn}}\mu_B SB/(k_B T_{\text{eff}})]), \tag{1.15}$$

where $N_0\beta$ is the exchange integral for the p-like electrons and κ is the Luttingter parameter. The band is fourfold degenerate, with m_J taking values $\pm 3/2$, $\pm 1/2$.

The exchange integrals α and β are defined as:

$$\alpha = \langle S|J^{sp-d}|S\rangle, \tag{1.16}$$

$$\beta = \langle X|J^{sp-d}|X\rangle, \tag{1.17}$$

and N_0 is the number of unit cells per unit volume. For $Cd_{1-x}Mn_xTe$, the sp-d exchange constants $N_0\alpha$ and $N_0\beta$ are equal to 0.22 eV and -0.88 eV respectively, independent of Mn concentration [25]. More generally, for the $A^{II}_{1-x}Mn_xTe^{VI}$ ternaries, $N_0\alpha$ and $N_0\beta$ have opposite sign and $|N_0\alpha| < |N_0\beta|$. Two physical processes are required to explain the origin of these values [26]. First, there is a positive contribution to the exchange constant, originating from the $1/r$ poten-

tial interaction between the band electron and the Mn^{2+} d electrons. This is a ferromagnetic interaction with the spin of the electron tending to align itself with the spin of the Mn^{2+} ion. Second, there is a negative contribution, originating from the hybridisation of the s and p band electrons with Mn^{2+} $3d^5$ states. At the Γ point, symmetry forbids the s-d hybridisation but p-d hybridisation is allowed. The latter is an antiferromagnetic process, and has a larger contribution compared to the potential interaction. $N_0\alpha$ relates to the Γ_6 band — s-like at the Γ point — therefore only the positive $1/r$ potential interaction contributes to its value. Conversely, $N_0\beta$ relates to the Γ_8 band — p-like at the Γ point — so, in addition to this positive component, there is a much larger negative component originating from the p-d hybridisation.

1.3 Spintronics

The term spintronics, first coined by S.A. Wolf in 1996 at DARPA[2], refers to a new branch of electronics that aims to exploit the spin state as well as the charge of carriers. Applications include nonvolatile magnetic random access memory (MRAM) [27], the spin field effect transistor [28] (SFET), the spin transistor, circularly-polarised light-emitting diode [29, 30], quantum bits (qubits) [31] and quantum entanglers. Although some of these, such as MRAM, are beginning to reach the stage of commercial devices, most are either prototypal or hypothetical devices and it is unclear whether all will become commercial components. It is not within the scope of this introduction to discuss the full field of spintronics research; for more information the reader is referred to the many reviews and articles available [32, 33].

The discovery of giant magnetoresistance (GMR) in 1988 [34, 35] is considered to mark the start of spintronics. GMR structures are composed of a nonmagnetic material sandwiched between two ferromagnetic materials. External magnetic fields are used to change the relative alignment of the magnetisations in the two ferromagnetic layers. The resistance is low when the magnetisations are parallel and high when they are antiparallel. This type of two layered structure is commonly referred to as a "spin valve". Arrays of such devices can be used to produce nonvolatile MRAM, where memory is preserved even when the power

[2]Defense Advanced Research Projects Agency

supply is removed. Each spin valve can be considered to be a magnetic bit, with the two resistance states corresponding to 0 and 1. Alternatively, MRAM arrays can comprise of magnetic tunnel junctions (MTJ) [27], which consist of a thin insulating layer, again, sandwiched between two ferromagnetic layers. Here, applying a voltage bias allows carriers to tunnel across the insulating layer. As in the GMR, spin valves two different resistance values are found for parallel and antiparallel magnetisations.

Nonvolatile MRAM systems are based around ferromagnetic metals but, for some devices, DMS are a much more appropriate material; for example, the circularly-polarised light-emitting diode. These devices require the injection of spin polarised electrons via a spin aligner [36] into a nonmagnetic layer. The efficiency of this spin injection is dependent upon the ratio of resistances in the magnetic and nonmagnetic materials. Therefore, using a metallic spin aligner to inject electrons through into a semiconductor LED structure leads to small spin injection efficiencies, unlike DMS spin aligners which offer no such drawback.

High spin injection efficiencies have been achieved by *Fiederling* [29, 30] et al using the II-VI DMS $Be_xMn_yZn_{1-x-y}Se$ as a spin aligner. The application of an external magnetic field along the growth direction leads to a giant Zeeman splitting of the conduction band states (section 1.2); the electrons will preferentially occupy the energetically more favourable -1/2 spin subband. These electrons are injected into a GaAs/GaAlAs p-i-n diode where they recombine with unpaired holes. If it is assumed that all the electrons are in the -1/2 state, then there are only two possible recombinations allowed by optical selection rules ($\Delta m_j = \pm 1$). The interband matrix elements for the heavy hole states ($\pm 3/2$) are three times that of the light hole states ($\pm 3/2$) (appendix A); hence, the σ^+ transition is three times more likely than the σ^- transition. The emitted light will be circularly polarised with a degree of polarisation equal to $(\sigma^- - \sigma^+)/(\sigma^- + \sigma^+)$, which can be used to calculate the spin injection efficiency of the device. Injection efficiencies of up to 90% have been measured.

So far the circularly-polarised light-emitting diode discussed has been based on II-VI DMS technology. As highlighted in the previous section, these are generally very well understood materials and so are ideal for fundamental studies in this area. However, the major drawback of II–VI devices is they will only show significant paramagnetism at low temperatures ($\sim$2 K). Alternatively, III-V DMS

may be made ferromagnetic with Curie temperatures up to ~170 K, but have different problems associated with them. Currently, there is much interest in the III-V DMS $Ga_{1-x}Mn_xAs$, a naturally p-type material (section 4.3). This is a problem because holes tend lose their spin polarisation faster than electrons due to the larger spin-orbit coupling in the valence band. However, spin injection efficiencies of 80% have been achieved using a $Ga_{1-x}Mn_xAs$ spin aligner, when the device is designed to allow the conduction band electrons to (Zener) tunnel into the LED structure [37].

The research into the spintronic devices considered so far is at the stage of producing working devices, but other areas of the field are far less advanced. For example, the development of quantum bits (qubits) for quantum computing applications. A conventional bit has two states 0 and 1, whereas a qubit can exist in a superposition of these two states where it is neither 0 or 1. One of the possible ways of achieving an optically-addressable qubit is by utilising the spin of an electron, which has two states (up or down). This has led to research into DMS quantum dots, with the aim to have a single magnetic ion within each dot.

1.4 Summary

The fundamental properties of CdTe have been outlined in section 1.1. This includes values for key parameters: such as the bandgap energy, the lattice parameter, the effective masses of carriers and the effective g factors. Following on from this, sections 1.2.1 and 1.2.2 have reviewed the electronic and magnetic properties of DMS, with particular focus on $Cd_{1-x}Mn_xTe$. The latter has a zinc-blende structure, and a Mn^{2+} concentration in the range of $0 < x \leq 0.77$. Its lattice constant and energy gap have a linear dependence on magnetic ion concentration. The magnetic properties of DMS are strongly influenced by the exchange interaction (both *sp-d* and *d-d* exchange). Steps in the magnetisation at high magnetic fields can be attributed to Mn^{2+}-Mn^{2+} pair (*d-d* exchange) interactions. The *sp-d* exchange interaction between the band electrons and the Mn^{2+} d electrons gives rise to giant Zeeman effects. This can be effectively modelled with a modified Brillouin function. Much of the interest in DMS is fuelled by their applicability to the field of spintronics. A short introduction to this topic has been given in section 1.3.

Chapter 2

Raman scattering in semiconductors

Currently, Raman scattering in semiconductors is used as part of a range of experimental techniques to investigate their vibrational and optical properties. The Raman effect is introduced in section 2.1, by reviewing the basic theory behind vibrational Raman spectroscopy: the classic method most associated with Raman scattering. In sections 2.2 and 2.3 the two key Raman techniques upon which this work is based are outlined: spin-flip Raman spectroscopy (SFRS) and coherent Raman electron spin resonance (CRESR). In both cases, example spectra centred on CdTe-based nonmagnetic heterostructures are presented.

2.1 Raman spectroscopy

The Raman effect is the inelastic scattering of light with matter; first observed by C.V. Raman in 1928 [38]. In conventional (vibrational) Raman spectroscopy the light is scattered by phonon modes [39, 40]. The scattering mechanism can either involve a loss in energy (Stokes process), or a gain in energy (anti-Stokes process). These processes must conserve both energy and momentum:

$$\hbar\omega_{\mathrm{L}} = \hbar\omega_{\mathrm{out}} \pm \hbar\omega_{\mathrm{phon}}, \tag{2.1}$$

$$\hbar\mathbf{k}_{\mathrm{L}} = \hbar\mathbf{k}_{\mathrm{out}} \pm \hbar\mathbf{k}_{\mathrm{phon}}. \tag{2.2}$$

Here ω_{L} ($\mathbf{k}_{\mathrm{L}}$), ω_{out} ($\mathbf{k}_{\mathrm{out}}$) and ω_{phon} ($\mathbf{k}_{\mathrm{phon}}$) are the frequencies (wavevectors) of the incoming photon, outgoing photon and phonon mode respectively.

Initially, vibrational Raman scattering is considered classically using the simple case of a diatomic molecule. The oscillating electric field ε of the incoming photon (with a frequency ν_l) induces a fluctuating electric dipole μ_i in the molecule of the same frequency:

$$\mu_i = \alpha\varepsilon = \alpha\varepsilon_0 \cos(2\pi\nu_l t). \tag{2.3}$$

Here α is the polarisability of the molecule and ε_0 is the electric field strength. Assuming simple harmonic motion, a molecule vibrating with a frequency ν_v has a polarisability given by

$$\alpha = \alpha_0 + \left(\frac{\partial\alpha}{\partial q_v}\right)_0 q_v = \alpha_0 + \left(\frac{\partial\alpha}{\partial q_v}\right)_0 q_0 \cos(2\pi\nu_v t), \tag{2.4}$$

where, α_0 is the equilibrium polarisability, and q_0 and q_v are the equilibrium position and the position at time t of the molecule respectively. Combining Eq. 2.3 and Eq. 2.4 yields

$$\mu_i = \alpha_0\varepsilon_0 \cos(2\pi\mu_l t) + \frac{1}{2}\left(\frac{\partial\alpha}{\partial q_v}\right)_0 \varepsilon_0 q_0 \{\cos[2\pi(\nu_l+\nu_v)t] + \cos[2\pi(\nu_l-\nu_v)t]\}. \tag{2.5}$$

Here the first, second and third terms describe Rayleigh (elastically) scattered, Raman (anti-Stokes) scattered and Raman (Stokes) scattered light respectively.

The quantum mechanical approach takes into account the quantised nature of the molecule's vibrational energy levels, given by

$$E_{\mathrm{v}} = h\nu\left(n_{\mathrm{v}} + \frac{1}{2}\right). \tag{2.6}$$

Here ν is the frequency of the vibration and n_{v} is the vibrational quantum number, which takes an integer value. The light is Rayleigh scattered if the incoming and outgoing photons induce electric dipole transitions that begin and end at the same energy level. When the incoming photon induces a transition which starts at an energy level that is lower (higher) in energy than the end of the transition which results in the outgoing photon, the light is Stokes (anti-Stokes) shifted.

There is a strong enhancement of the vibrational Raman signal when the excitation energy ($\hbar\omega_{\mathrm{L}}$) is equal to the energy separation (E_{ex}) of the electronic excited

state from the vibrational state. This is clearly shown by the scattering cross section [41]

$$\frac{\mathrm{d}\sigma}{\mathrm{d}\Omega} \propto f^2 \left(\frac{e^2}{mc^2}\right)^2 \frac{\omega_\mathrm{R}}{\omega_\mathrm{L}} \frac{(\hbar\omega_\mathrm{L})^2}{(E_\mathrm{ex} - \hbar\omega_\mathrm{L})^2 + (\Gamma/2)^2}, \tag{2.7}$$

where f is the oscillator strength, ω_R is the frequency of the Raman shifted light and Γ is a phenomenological damping parameter. The use of tunable excitation sources leads to optical site-selective experiments, where the incoming photon can be tuned into a series of excited states.

2.2 Spin-flip Raman spectroscopy

Spin-flip Raman spectroscopy (SFRS) [42], as the name suggests, is the inelastic scattering of light via a spin-flip. This was first considered nearly forty years after Raman's original discovery by Yafet [43], who extended Wolff's [44] initial proposal of Raman scattering from Landau levels. The spin-flip of conduction band electrons in InSb, observed shortly afterwards [45], gave the first experimental evidence for such a process. Since then, SFRS has remained a popular method for investigating the electronic properties of semiconductors, due to the technique's high sensitivity and site-selective nature.

2.2.1 Theory of SFRS

The spin-flip scattering mechanism for a simple two level degenerate system, for example a free or bound electron, is shown in Fig. 2.1. The applied magnetic field splits the two electron spin states ($|1\rangle$ and $|2\rangle$) in energy by

$$\Delta E = m_S g \mu_B B(\uparrow) - m_S g \mu_B B(\downarrow) = g \mu_B B, \tag{2.8}$$

where m_S is the magnetic quantum number, μ_B is the Bohr magneton, B is the applied magnetic field, g is the effective g factor and $\uparrow$ ($\downarrow$) refers to a spin up (down) electron. In the Stokes process (Fig. 2.1 (a)), a photon of appropriate energy can excite an electron from the lower of the two spin states ($|1\rangle$) to an optically excited state ($|3\rangle$). Likewise, an electron in this excited state ($|3\rangle$) can recombine with a hole in the higher of the two spin states ($|2\rangle$) and emit a

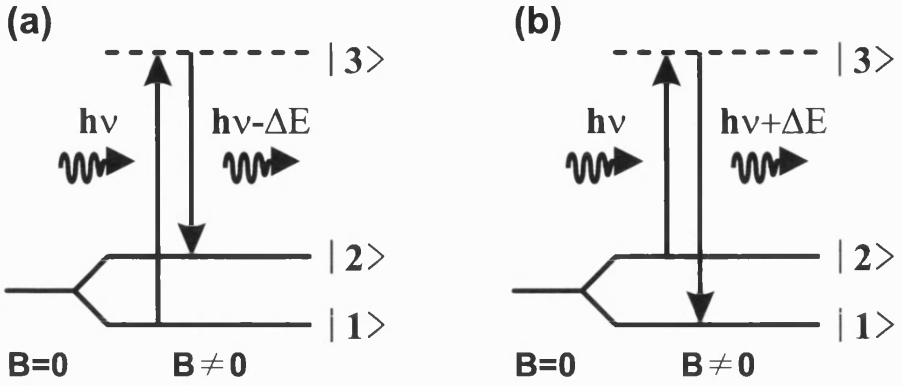

Figure 2.1: Spin-flip Raman scattering mechanism: a) Stokes process; b) anti-Stokes process.

photon. The energy difference between incoming and outgoing photons is equal to the spin splitting of states $|1\rangle$ and $|2\rangle$. There is a strong enhancement of the spin-flip Raman signal when the laser energy is tuned into resonance with the excited state (Eq. 2.7), i.e. the incoming photon energy $h\nu = E_{|3\rangle} - E_{|1\rangle}$. The anti-Stokes process (Fig. 2.1 (b)) is similar, except the incoming (outgoing) transition occurs between spin states $|2\rangle$ ($|1\rangle$) and $|3\rangle$.

The SFRS experiments presented here, unless stated otherwise, have all been carried out in Voigt geometry ($\mathbf{B} \perp \mathbf{k}$). A photon polarised parallel to the applied magnetic field (π) can be absorbed or emitted from energy states where there is no change in angular momentum in the magnetic field direction ($\Delta m = 0$). Similarly, a photon polarised perpendicular to the applied magnetic field (σ) can be absorbed or emitted from energy states where there is an angular momentum change of one in the magnetic field direction ($\Delta m = \pm 1$). The difference in angular momentum between the electron spin states is $(1/2) - (-1/2) = 1$. Angular momentum must be conserved by the scattering process; therefore, incoming and outgoing photons are cross polarised ($z(\pi, \sigma)\bar{z}$ or $z(\sigma, \pi)\bar{z}$)[1].

2.2.2 Experimental Setup for SFRS

Samples are submersed in liquid He and cooled to a nominal temperature of 1.5 K. The cryostat contains a split-coil superconducting magnet capable of generating fields up to 6 T, and can be rotated through 90° to allow experiments in

[1]Using Porto notation, i.e. $a(b, c)d$, where a (d) is the direction of the ingoing (outgoing) light and b (c) is the direction of polarisation of the incident (emitted) light.

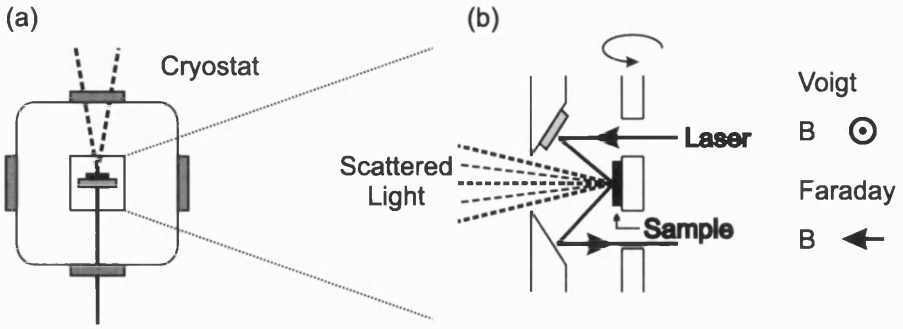

Figure 2.2: Schematic of laser beam path and light scattering inside the cryostat for SFRS: a) top view; b) side view.

both the Voigt ($\mathbf{B} \perp \mathbf{k}$) and the Faraday configurations ($\mathbf{B} \parallel \mathbf{k}$). The excitation source is an Ar^+-ion pumped titanium sapphire laser, giving a tunable wavelength range of 700–1000 nm. The path of the laser beam through the cryostat is shown schematically in Fig. 2.2. This setup significantly reduces the amount of elastically scattered laser light that is passed through the spectrometer. The design of the sample holder enables samples to be rotated in the direction shown in Fig. 2.2 (b), allowing angle dependent data to be acquired. A polariser and analyser, before and after the cryostat respectively, are used in the crossed polarisation configuration. Scattered light is focussed onto the entrance slit of a Jobin Yvon (S 3000) triple grating spectrometer. This is comprised of two sections. First, a premonochromator (DHR 320): a double monochromator with a focal length of 320mm. Second, a single monochromator (THR 1000), which has a focal length of 1m. The latter has an interchangeable grating: either 1800 gr/mm or 300 gr/mm. Connected to the spectrometer is a choice of two detectors: a liquid nitrogen cooled CCD camera or a single photon counting photomultiplier.

A proportion of the spin-flip Raman data has been acquired at the University of Würzburg. Their system uses a 7.5/9 T split-coil magnet, a Dilor XY triple grating spectrometer and a CCD detector. The excitation source is an Ar^+-ion pumped dye laser (Pyridine 2). It is stated in the figure heading when this is the case.

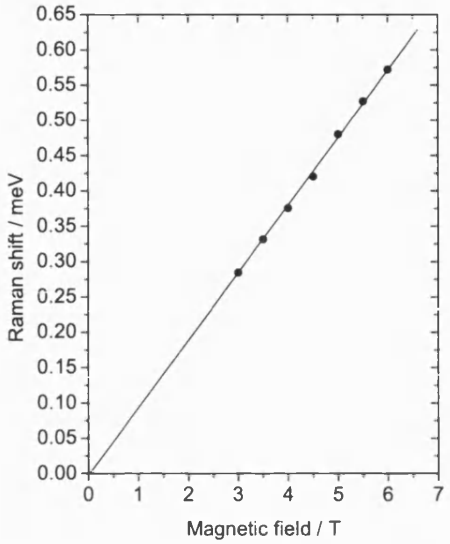

Figure 2.3: Spin-flip Raman shift of the conduction band electron in a CdTe epilayer (#292, appendix C), with respect to the applied magnetic field. Data points are the average energy positions of Stokes and anti-Stokes components. Solid line is a linear fit to the data points, with $g = -1.651 \pm 0.010$.

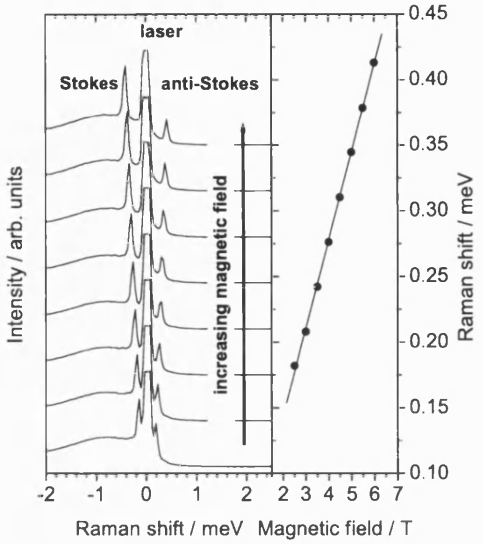

Figure 2.4: Left) SFRS spectra for a 58 Å wide CdTe/$Cd_{0.80}Mg_{0.20}$Te SQW (#305A, appendix C). Spectra have been normalised to the laser energy. Right), average spin-flip Raman shift of the Stokes and anti-Stokes signal. Solid line is a linear fit to the data points, with $g = -1.16 \pm 0.01$. Data acquired at the University of Würzburg.

2.2.3 Spin-flip Raman Spectroscopy of CdTe

The electron spin-flip Raman shift in CdTe, as a function of applied magnetic field, is plotted in Fig. 2.3. The sample has a 2 μm layer of CdTe on an InSb substrate (#292, appendix C). The average of the Stokes and anti-Stokes components has been taken to improve the accuracy in fitting the laser position. Applying Eq. 2.8 gives $g = -1.676 \pm 0.010$, or $g = -1.651 \pm 0.010$ if zero Raman shift at zero magnetic field is assumed. This is in good agreement with the literature values (section 1.1). The excitation energy is tuned to 1.598 eV; therefore it is in optical resonance with a free or weakly bound exciton [46].

Figure 2.4 shows the spin-flip Raman spectra for an electron in a 58 Å wide CdTe/$Cd_{0.80}Mg_{0.20}$Te single quantum well (SQW). Here the magnetic field is applied perpendicular to the growth axis of the quantum well (Voigt geometry). Both the Stokes component (loss in energy) and the anti-Stokes component (gain in energy) are clearly observed. The sample is grown on a GaAs (100) substrate, with a CdTe (4.5 μm) buffer layer, a CdMgTe (1 μm) buffer layer, 300 Å barriers

and a 500 Å capping layer. The electron g factor is found to be $g = -1.16 \pm 0.01$, significantly different from the bulk value.

The observed deviation of the g factor from its bulk value is well known in quantum well structures [5, 9, 47]. The wavefunctions of the carriers in the well penetrate into the barrier, so there are contributions to the g factor from both the well and barrier material. Confinement and strain modify the energy gap of the quantum well, and split the light- and heavy-hole states at zero magnetic field (chapter 5). There is a reduction in point symmetry of the quantum well (D_{2d}) compared to the bulk value (T_d), leading to an anisotropy in the electron g factor. When the magnetic field is parallel to the growth axis of the quantum well the g factor ($g^e_{\parallel}$), is described, using five-level $\mathbf{k} \cdot \mathbf{p}$ theory (appendix A), by the expression [9][48]

$$g^e_{\parallel} \approx g_0 \left[1 - \frac{E_p}{3} \left(\frac{1}{E_{\rm ex}} - \frac{1}{E_{\rm ex} + \Delta_0} \right) - \frac{E'_p}{3} \left(\frac{1}{E(\Gamma^C_7) - E_{\rm ex}} - \frac{1}{E(\Gamma^C_8) - E_{\rm ex}} \right) + C' + \frac{2}{9} \frac{\sqrt{E_p E'_p} \Delta^-}{E(\Gamma^C_7) - E_{\rm ex}} \left(\frac{1}{E_{\rm ex}} + \frac{2}{E_{\rm ex}} + \Delta_0 \right) \right], \tag{2.9}$$

where $E_{\rm ex}$ is the heavy-hole exciton energy. It is assumed the quantum well system takes the same values for the band parameters as for bulk CdTe [9, 48, 49]: $E_p = 21$ eV, $E'_p = 5.1$ eV, $\Delta_0 = 0.93$ eV, $\Delta^- = -0.16$ eV, $E(\Gamma^C_7) = 5.6$ eV, $E(\Gamma^C_8) = 5.3$ eV, $C' = -0.02$. The anisotropic electron g factor, for the magnetic field perpendicular to the growth axis ($g^e_{\perp}$) [9]

$$g^e_{\perp} \approx \frac{E_p}{E^2_{\rm ex}} \Delta_{\rm lh-hh} - g^e_{\parallel}, \tag{2.10}$$

where $\Delta_{\rm lh-hh}$ is the energy splitting of light- and heavy-holes states.

Using the methods outlined in detail in chapter 5, the heavy-hole free exciton energy of this quantum well is calculated to be 1.653 eV. This is in good agreement with the photoluminescence[2] data shown in Fig. 2.5. Here, the energy separation between free (X) and donor bound (D^0, X) excitons is 3.7 meV, consistent with the literature values [50, 51, 52]. The same calculation gives a value of 25 meV for the light- and heavy-hole energy splitting. These values are substituted into Eq. 2.9 and Eq. 2.10 to obtain $g^e_{\perp} = -1.26$. The discrepancy between this and the experimental value ($g^e_{\perp} = -1.16 \pm 0.01$) is most likely due to strain in the

[2]Acquired with the same experimental setup as for SFRS

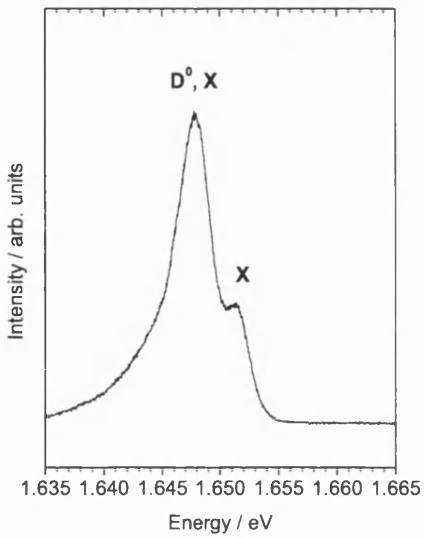

Figure 2.5: Photoluminescence spectrum, originating from the donor bound (D^0,X) and free (X) excitons, for a 58 Å wide $CdTe/Cd_{0.80}Mg_{0.20}Te$ SQW at zero magnetic field. Data acquired at the University of Würzburg.

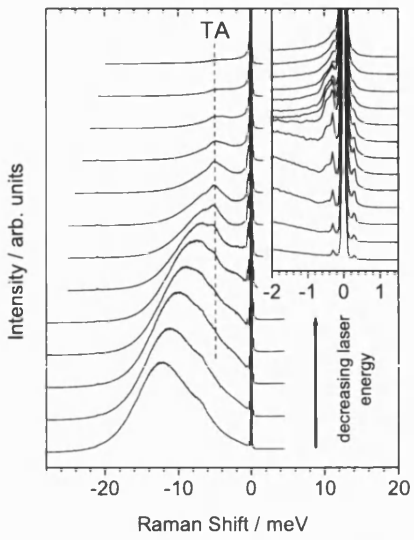

Figure 2.6: Spin-flip Raman spectra for a series of excitation energies, for a 32 Å wide $CdTe/Cd_{0.80}Mg_{0.20}Te$ single quantum well (#305A, appendix C), at a magnetic field of 6 T. The dashed line is a guide for the eye. Data acquired at the University of Würzburg.

sample, originating from the lattice mismatch between adjacent materials. The strain Hamiltonian for a strain tensor ϵ in the z direction is

$$\mathbf{H}_{\mathrm{Str}} = \epsilon \left(J_z^2 - \frac{1}{3} J^2 \right), \tag{2.11}$$

where J is total angular momentum operator. The strain will increase the splitting of the light- and heavy hole energy states, and thus will decrease $g_\perp^e$ in the well.

Figure 2.6 shows the laser energy resonance profile for a narrower (32 Å wide) $CdTe/Cd_{0.80}Mg_{0.20}Te$ quantum well, at an applied magnetic field of 6 T and for excitation energies ranging from 1.728 eV – 1.715 eV. The donor bound exciton energy, obtained from photoluminescence data, is 1.715 eV. This is consistent with a calculated heavy-hole free exciton energy (chapter 5) of 1.719 eV. In the inset of Fig. 2.6 two spin-flip signals are clearly resolvable. The peak at lower energy (-0.31 meV) is the conduction band electron discussed previously. This has a measured and calculated (using Eq. 2.9 and Eq. 2.10) g factor of $g_\perp^e = -0.89 \pm 0.01$ and $g_\perp^e = -0.98$ respectively. Again, the calculation overestimates the g factor

by not taking into account effects due to strain. The broader of the two peaks (-0.44 meV) is due to the spin-flip of a heavy-hole exciton [9]. This has a g factor of $g_{\perp}^{\mathrm{ex}} = 1.27 \pm 0.01$[3], at 6 T. From this, the heavy-hole g factor can be calculated using

$$g_{\perp}^{\mathrm{hh}} = g_{\perp}^{\mathrm{ex}} + g_{\perp}^{e}, \tag{2.12}$$

to give $g_{\perp}^{\mathrm{hh}} = 0.38$. Magnetic field dependent measurements of these signals were not possible, because the two signals cannot be resolved at low values of the magnetic field. The peak denoted TA in Fig. 2.6 is a vibrational Raman signal, attributed to the transverse acoustic phonon mode [53, 54].

2.3 Coherent Raman electron spin resonance

Spin-flip Raman spectroscopy has been shown in previous sections to be an important and popular technique for the investigation of the electronic properties of semiconductors. Unfortunately the energy resolution of this method is limited by diffraction grating-based spectrometers and laser linewidths; the energy resolution of SFRS is $\sim$ 0.04 meV (with the CCD), which is comparable to the linewidth of the electron (nonmagnetic semiconductors) and paramagnetic resonance (DMS) spin-flip Raman peaks ($\sim$ 0.05 meV). A well established alternative is electron spin resonance (ESR). This has the benefit of much higher energy resolution, but lacks the optical selectivity of SFRS and has much lower sensitivity. Coherent Raman electron spin resonance (CRESR) is a novel spectroscopic method, that incorporates both SFRS and ESR to give a method with optical selectivity, high sensitivity[4] and high energy resolution.

The section begins by introducing spin precession and outlining the theory of ESR. Both are essential for understanding CRESR, especially as conventional ESR theory is used in the analysis of coherent Raman ESR line shapes. Subsections 2.3.1 and 2.3.2 describe the principles and experimental arrangement of CRESR respectively. Here the fundamental differences between ESR and CRESR are clearly highlighted. The section ends with a look at a typical coherent Raman spectrum for a nonmagnetic semiconductor.

[3]The sign convention has been assumed from the literature.

[4]Discussed at the end of chapter 5.

2.3.1 Spin precession

An electron with orbital angular momentum $\mathbf{L}$, will have an magnetic dipole moment μ associated with it [55], such that

$$\mu = \gamma \mathbf{L}. \tag{2.13}$$

Here γ is the gyroscopic ratio and μ is parallel to $\mathbf{L}$. If the electron is within a magnetic field $\mathbf{B}$, the energy of its magnetic moment is

$$E = -\mu \cdot \mathbf{B}. \tag{2.14}$$

This is at a minimum when μ is parallel to $\mathbf{B}$; hence, there is a torque $\mathbf{G}$ acting to align the magnetic moment along the direction of the magnetic field. This is given by

$$\mathbf{G} = \mu \times \mathbf{B}. \tag{2.15}$$

Remembering, $\mathbf{G}$ is equal to the rate of change of angular momentum, Eq. 2.15 can be rewritten as

$$\frac{\mathrm{d}\mu}{\mathrm{d}t} = \gamma \mu \times \mathbf{B}. \tag{2.16}$$

This shows the change in magnetic moment is perpendicular to the magnetic moment and the magnetic field. Hence, it follows that μ will precess around $\mathbf{B}$. Equation 2.16 describes the precession for a single electron, but in a semiconductor it is more useful to think in terms of the magnetisation $\mathbf{M}$, the magnetic moment per unit volume:

$$\frac{d\mathbf{M}}{dt} = \gamma \mathbf{M} \times \mathbf{B}. \tag{2.17}$$

For a magnetic field B_z aligned along the z axis, and a magnetic dipole moment initially at an angle θ to B_z (Fig. 2.7), μ will precess with a frequency of

$$\omega_{\mathrm{L}} = \gamma B_z, \tag{2.18}$$

where ω_{L} is known as the Larmor precession frequency.

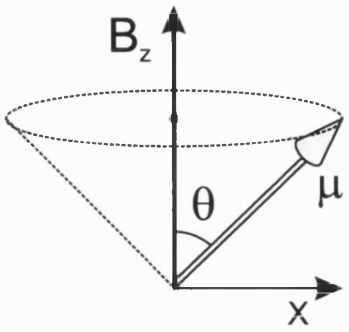

Figure 2.7: A magnetic moment μ will precess around a magnetic field B_z at the Larmor precession frequency ω_{L}.

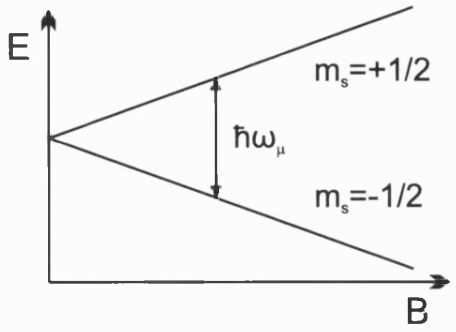

Figure 2.8: Energy level (schematic) of a two level degenerate system as a function of magnetic field.

2.3.2 Electron spin resonance

Electron spin resonance (ESR), also known as electron paramagnetic resonance (EPR), is the traditional way of measuring g factors (appendix A) directly. The general principles are analogous to nuclear magnetic resonance (NMR), except in ESR a microwave field is used to study spin states of electrons, as oppose to the radio frequency field used to investigate nuclear spin states in NMR. Hence, texts on both ESR and NMR are recommended [56, 57, 58].

In the ESR experiment, an oscillating microwave field, with small amplitude B_x, is applied to a sample perpendicular to a static magnetic field B_0, which is parallel to the z axis. In the simplest case, for electrons within these fields, the magnetic resonance condition is fulfilled when the energy of the microwave photon ($\hbar\omega_\mu$) is equal to the energy of the spin splitting (Fig. 2.8):

$$\hbar\omega_\mu = g\mu_{\mathrm{B}}B_0. \tag{2.19}$$

Under this condition (if $N_+ < N_-$) a magnetic dipole transition is induced between the spin states, where N_+ and N_- are the occupations of states $m_S = +1/2$ and $m_S = -1/2$ respectively. The absorption of microwave energy is monitored, whilst either varying the microwave frequency and keeping the magnetic field strength fixed, or conversely varying the magnetic field and keeping the microwave frequency fixed. The latter is more common, because in general the magnetic field can be varied over a much larger range.

Without a relaxation mechanism for the electrons, the microwave absorption

would become saturated when $N_+ = N_-$, since induced emission would equal the absorption. In semiconductors, energy is lost to the crystalline environment through electron-phonon interactions. This has an associated spin-lattice relaxation time T_{sl}, defined as the time taken for the spin system to return to thermal equilibrium after the system is perturbed. This is taken into account in the modified form of Eq. 2.17, the Bloch equations [59]:

$$\frac{\mathrm{d}M_x}{\mathrm{d}t} = \gamma(\mathbf{M}\times\mathbf{B})_x - \frac{M_x}{T_2} = \gamma M_y B_0 - \frac{M_x}{T_2}, \tag{2.20}$$

$$\frac{\mathrm{d}M_y}{\mathrm{d}t} = \gamma(\mathbf{M}\times\mathbf{B})_y - \frac{M_y}{T_2} = \gamma(M_z B_x - M_x B_0) - \frac{M_y}{T_2}, \tag{2.21}$$

$$\frac{\mathrm{d}M_z}{\mathrm{d}t} = \gamma(\mathbf{M}\times\mathbf{B})_z + \frac{M_0 - M_z}{T_1} = -\gamma M_y B_x - \frac{M_0 - M_z}{T_1}. \tag{2.22}$$

Here $\gamma = -g_e\mu_B/\hbar$, $\mathbf{B_x}(t) = B_{x0}\cos(\omega t) = 2B_1\cos(\omega t)$ and $\mathbf{B} = \mathbf{B_0} + \mathbf{B_x}(t)$. The relaxation time is represented by two separate components: T_1 and T_2. T_1, sometimes referred to as the longitudinal relaxation time, is related to the component of the magnetisation which is parallel to the static magnetic field ($B_0 \parallel z$); therefore, it is an inelastic process. T_2, the transverse relaxation time, is associated with the magnetisation in the x-y plane. This can involve elastic processes due to either spin-spin interactions or an inhomogeneous g factor.

The alternating magnetic field B_x can be considered to be the superposition of two rotating fields, one clockwise and the other counterclockwise, of amplitude B_1. Near magnetic resonance the component that rotates in the opposite direction to the precession of the magnetic moment can be neglected, leaving a single rotating component. A magnetic moment with $g_e > 0$ will precess in the opposite direction from one with $g_e < 0$, but there will always be a component of the microwave field that will be rotating in the direction of precession. Equations 2.20 – 2.22 are solved by converting to a reference frame which rotates about the z axis at the microwave frequency:

$$\frac{\mathrm{d}M'_x}{\mathrm{d}t} = (\omega - \omega_0)M'_y - \frac{M'_x}{T_2}, \tag{2.23}$$

$$\frac{\mathrm{d}M'_y}{\mathrm{d}t} = -(\omega - \omega_0)M'_x - \frac{M'_y}{T_2} + \gamma B_1 M'_z, \tag{2.24}$$

$$\frac{\mathrm{d}M'_z}{\mathrm{d}t} = -\gamma B_1 M'_y - \frac{M'_z - M_0}{T_1}. \tag{2.25}$$

Here $\omega_0 = -\gamma B_0$ is the spin resonance frequency and M_0 is the magnetisation when the system is in thermal equilibrium with zero microwave transitions. In

the stationary state ($dM'/dt = 0$), the following solutions to equations 2.23 – 2.25 are found:

$$M'_x = \frac{\gamma B_1(\omega_0 - \omega)T_2^2}{1 + (\omega_0 - \omega)^2 T_2^2 + \gamma^2 B_1^2 T_1 T_2} M_0, \tag{2.26}$$

$$M'_y = \frac{\gamma B_1 T_2}{1 + (\omega_0 - \omega)^2 T_2^2 + \gamma^2 B_1^2 T_1 T_2} M_0, \tag{2.27}$$

$$M'_z = \frac{1 + (\omega_0 - \omega)^2 T_2^2}{1 + (\omega_0 - \omega)^2 T_2^2 + \gamma^2 B_1^2 T_1 T_2} M_0. \tag{2.28}$$

Transformation from the reference frame back to the laboratory frame is given by

$$\mathbf{M} = \begin{pmatrix} M_x \\ M_y \\ M_z \end{pmatrix} = \begin{pmatrix} M'_x \cos(wt) + M'_y \sin(wt) \\ -M'_x \sin(wt) + M'_y \cos(wt) \\ M'_z \end{pmatrix}. \tag{2.29}$$

The transverse magnetisation contains two components, M'_x and M'_y, separated in phase by 90°, and can be rewritten as

$$M_x = (\chi' \cos(\omega t) + \chi'' \sin(\omega t)) B_1. \tag{2.30}$$

Here χ' and χ'' are the dispersive and absorptive components of the complex magnetic susceptibility: $\chi = \chi' - i\chi''$. Assuming there is no saturation, i.e. $\gamma^2 B_1^2 T_1 T_2 \ll 1$, these are equal to:

$$\chi' = \frac{M'_x}{2B_1} = \frac{\gamma(\omega - \omega_0)T_2^2 M_0}{2[1 + (\omega - \omega_0)^2 T_2^2]}, \tag{2.31}$$

$$\chi'' = \frac{M'_y}{2B_1} = \frac{\gamma T_2 M_0}{2[1 + (\omega - \omega_0)^2 T_2^2]}. \tag{2.32}$$

Both the absorption (χ'') and dispersion (χ') components are plotted, as a function of $(\omega - \omega_0)T_2$, in Fig. 2.9. For a homogeneous ESR line the absorptive part has a Lorentzian lineshape. It is important to remember that the solutions to the Bloch equations are only valid in the stationary state; therefore, the magnetic field must be scanned slowly to avoid "passage" effects.

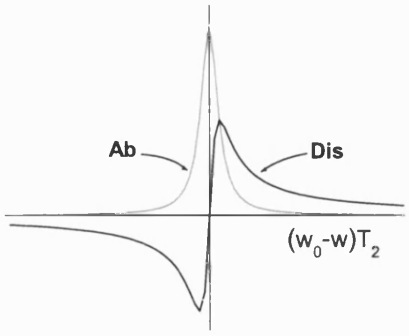

Figure 2.9: Absorption (Ab) and dispersion (Dis) lineshape for a homogeneous ESR line.

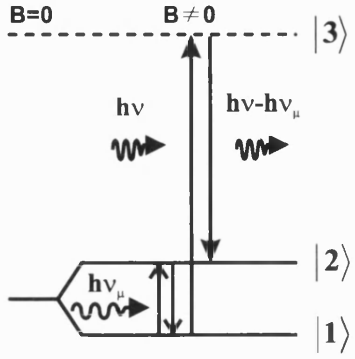

Figure 2.10: Scattering mechanism (schematic) for coherent Raman ESR.

2.3.3 Coherent Raman ESR

The scattering mechanism for the coherent Raman electron spin resonance (CRESR) experiment is shown schematically in Fig. 2.10, for a simple three level system. Here $|1\rangle$ and $|2\rangle$ are the spin states for $S = 1/2$ particle and $|3\rangle$ is an excited state of higher energy. As in standard ESR (subsection 2.3.2) a microwave magnetic field B_1 (x direction), of fixed frequency ν_μ, is applied to the sample perpendicular to a slowly swept magnetic field B_0 (z direction). When the spin resonance condition (Eq. 2.19) is met, a coherence is induced between states $|1\rangle$ and $|2\rangle$. In addition, the CRESR method has a laser beam is focused onto the sample (y direction). Optical resonance occurs when the photon energy $\hbar\nu$ is equal to the energy difference $E_{|3\rangle} - E_{|1\rangle}$. Under this condition, the laser field will induce a coherence between states $|1\rangle$ and $|3\rangle$. When both spin and optical resonance is achieved simultaneously, states $|2\rangle$ and $|3\rangle$ are coherent.

The emitted Raman light is temporally and spatially coherent, assuming the laser and microwave fields are homogenous over the area of the sample irradiated by the laser, and is therefore a beam. The reflected laser excitation beam and the copropagating Raman wave beat with one another in a fast photodiode (optical heterodyne detection). The sample is simultaneously excited with σ and π polarised light. This is achieved by modulating the laser between left and right circular polarisations. In doing this, the Raman and reflected excitation E-vectors are not orthogonal and can constructively interfere. Analogous to ESR, CRESR gives an absorptive- and dispersive-like signal.

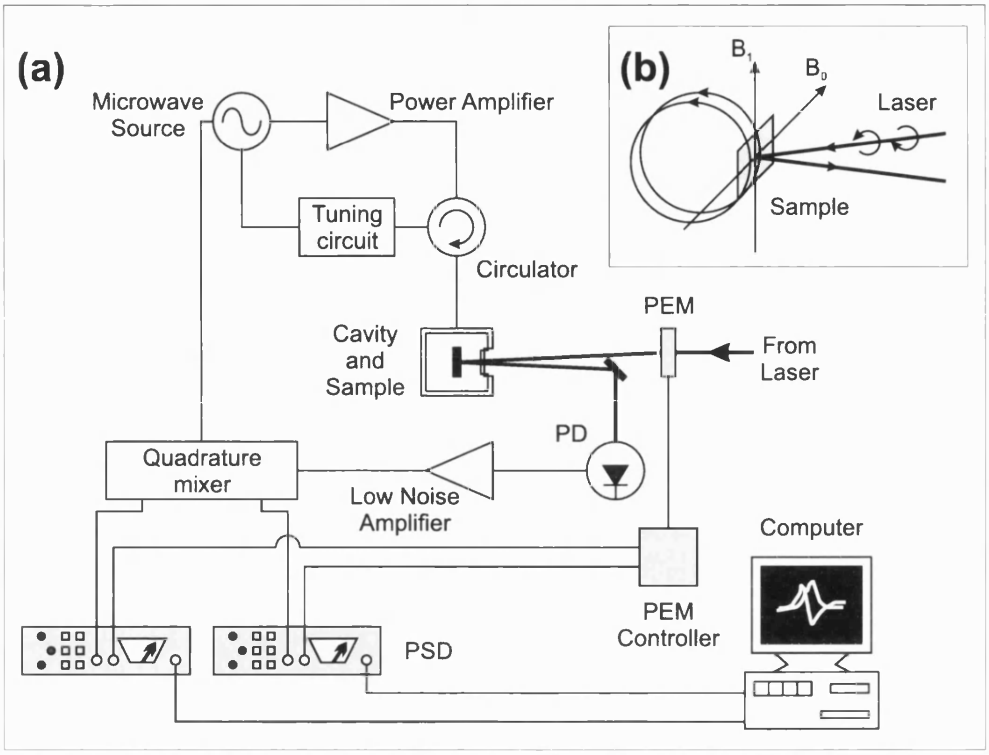

Figure 2.11: a) Experimental configuration (schematic) for CRESR. The phase sensitive detector, photodiode and the photo elastic modulator have been abbreviated to PSD, PD, and PEM respectively. b) Magnetic fields present inside the microwave cavity: magnetic field due to the superconducting magnet B_0; and microwave magnetic field B_1.

2.3.4 Experimental arrangement for CRESR

A schematic of the experimental setup required for CRESR experiments is shown in Fig. 2.11 (a). Microwaves are supplied to a TE_{012} mode rectangular microwave cavity resonator, via either a coaxial cable (13.7 GHz system) or waveguide (33.7 GHz system). The cavity is engineered to maximise the microwave magnetic field B_1 at the position of the sample (Fig. 2.11 (b)). A feedback system is used to keep the frequency of the microwave source equal to the cavity resonance frequency, as follows. The microwave signal is modulated at a frequency of the order of a hundred Hertz. This allows the reflected microwave signal from the resonator to be monitored using lock-in detection. If the cavity resonance has decreased (increased) in frequency, a negative (positive) error signal is produced, causing a decrease (increase) in the source frequency. At the front of the cavity there is a narrow slit, allowing the laser beam to be reflected off the sample's surface. The cavity and sample are placed inside the cryostat of a 3 T split-coil superconducting magnet, and cooled, using liquid helium, to a temperature of

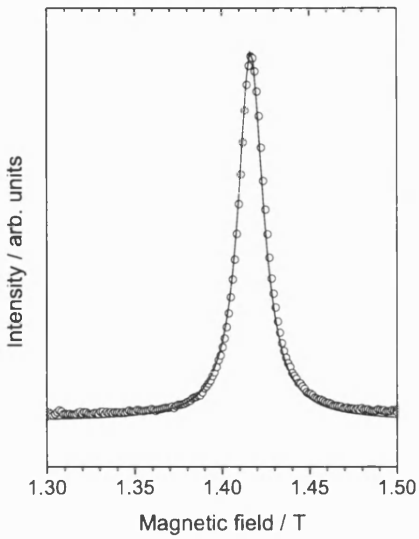

Figure 2.12: CRESR spectrum (absorptive component) for a 301 Å wide $CdTe/Cd_{0.80}Mg_{0.20}Te$ SQW (#305A, appendix C): experimental data (open circles) and simulated data (line).

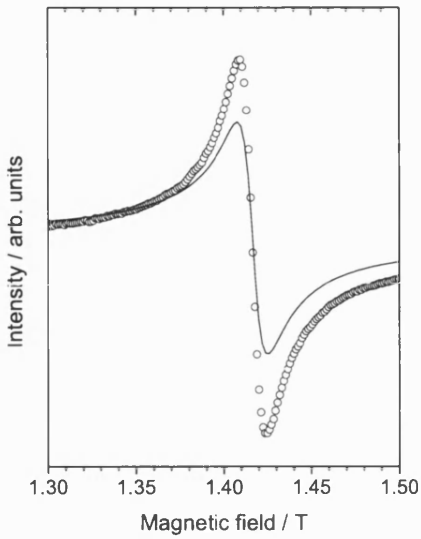

Figure 2.13: CRESR spectrum (dispersive component) for a 301 Å wide $CdTe/Cd_{0.80}Mg_{0.20}Te$ SQW (#305A, appendix C): experimental data (open circles) and simulated data (line).

1.7 K. The magnet supplies a magnetic field B_0, perpendicular to both B_1 and the laser beam. The microwave and laser frequency are kept fixed, whilst B_0 is slowly swept.

The optical excitation source is, as with SFRS, an Ar^+-ion pumped titanium sapphire laser; modulated, using a photo elastic modulator (PEM), between left and right circularly polarised light, at a frequency of 50 kHz. The reflected laser and emitted Raman beam are focussed onto a high-speed InGaAs Schottky photodiode. The microwave reference signal is mixed in phase, and 90° out of phase, with the resultant microwave beat signal in the quadrature mixer. This allows simultaneous measurement of both the absorption and dispersion components. These components are modulated at the PEM frequency, and are detected by standard lock-in detection.

2.3.5 Typical CRESR spectra

The absorptive and dispersive components of the coherent Raman-detected ESR signal, for a 301 Å wide $CdTe/Cd_{0.80}Mg_{0.20}Te$ single quantum well, are shown in

Fig. 2.12 and Fig. 2.13 respectively. Simulation, based on a Lorentzian ($f(x) = 1/(1+x^2)$), reproduces the lineshape of both components well. However, there is a difference in intensity between the simulated and experimental components of the dispersion part, a sign of microwave saturation effects. Microwave saturation limits the signal intensity of the absorption component, but the signal intensity of the dispersion component remains unaffected; hence, when microwave saturation occurs there is a change in the absorption and dispersion signal intensity ratio. The laser energy is tuned to 1.596 eV, which is comparable with a calculated exciton bandgap (chapter 5) of 1.599 eV for the heavy-hole exciton. These values are very close to the free exciton energy of bulk CdTe (section 1.1), which is consistent with a quantum well of this width. The signal is centred at a magnetic field of 1.471 T, with a microwave frequency of 33.4 GHz, and corresponds to an electron g factor of $g = |1.62 \pm 0.01|$. Again, this compares well with the theoretical value of $g = -1.59$, calculated using Eq. 2.10 (subsection 2.2.3).

2.4 Summary

Throughout this chapter, Raman scattering has been shown to be an important mechanism in a range of experimental techniques, used in the investigation of the properties of semiconductors. Spin-flip Raman spectroscopy (section 2.2) is an effective, and sensitive, method for directly obtaining the effective g factors in a given heterostructure. In addition, the use of tunable excitation sources allows optically site-selective experiments to be performed. Subsection 2.2.3 clearly demonstrates this for CdTe/$Cd_{1-y}Mg_yTe$ single quantum wells. Unfortunately though, spin-flip Raman's resolution is limited by the laser linewidth. This is not the case for coherent Raman electron spin resonance (section 2.3), which combines the advantages of SFRS with the high energy resolution of ESR.

CRESR is still a relatively unknown experimental technique in the semiconductor field. Only two semiconductors, both nonmagnetic, have been investigated using a Coherent Raman method: CdS [60, 61] (without heterodyne detection); and ZnSe [62] (the first application to a semiconductor which incorporated heterodyne detection). The work presented in this, and subsequent chapters, greatly increases this list, showing successful applications to the following nonmagnetic and semimagnetic semiconductors: CdTe/$Cd_{1-y}Mg_yTe$ QW (this chapter), bulk

$Cd_{1-x}Mn_xTe$ (chapter 3), $Cd_{1-x}Mn_xTe/Cd_{1-x-y}Mg_yMn_xTe$ QW (chapter 5). In the latter case, the sensitivity of the coherent Raman method is discussed in relation to conventional ESR.

Chapter 3

Optical spectroscopy of bulk CdMnTe

For the first application of the CRESR method to a diluted magnetic semiconductor, the archetypal material $Cd_{1-x}Mn_xTe$ was chosen, specifically bulk $Cd_{0.995}Mn_{0.005}Te$. The optical and magnetic properties of $Cd_{1-x}Mn_xTe$ have been summarised in detail in section 1.2. Photoluminescence (PL) and photoluminescence excitation (PLE) spectroscopy have been used to determine both the energy dependence and the magnetic field dependence of excitonic transitions in this sample (section 3.1). When the excitation source is tuned to the energy of the free exciton, several spin-flip Raman signals are observed: conduction band electron spin-flip (subsection 3.2.1) and electron paramagnetic resonance (PMR) Mn^{2+} ions (subsection 3.2.2). Magnetic field dependent measurements of the former provide an accurate value of the effective Mn^{2+} ion concentration. If the laser is tuned higher in energy, the spin-flip of antiferromagnetically aligned Mn^{2+} pairs is observed (subsection 3.2.3). From this, nearest and next-nearest neighbour exchange constants can be determined.

The PL, PLE and SFRS experiments lay the foundations for understanding the main result of this chapter: coherent Raman-detected PMR of Mn^{2+} in CdTe (section 3.3). This is detected in optical resonance with a free or weakly bound exciton, with both a 13.7 GHz and 33.7 GHz microwave source (section 3.3). With the 33.7 GHz setup it is possible to resolve contributions from both the hyperfine interaction, between Mn^{2+} $3d^5$ electrons and the manganese nucleus,

and the cubic crystal field (subsection 3.3.1). This additional structure is not resolvable in the spin-flip Raman-detected PMR signal. The absorption component of the coherent Raman detected PMR signal is found to deviate significantly from the standard Lorentzian lineshape, due to microwave resonant heating effects. The relative intensity and phase dependence of the CRESR lineshape on the optical excitation energy is analysed in detail in subsection 3.3.3. Simulation of this data requires all optically allowed Raman processes (Fig. 3.9) to be taken into consideration. In subsection 3.3.4 the microwave power dependence is investigated. The microwaves in the cavity heat the sample; therefore, a change in microwave power will change the temperature of the spin system. This leads to a change in the energy of the exciton states because of the temperature sensitivity of the Brillouin function (Eq. 1.14 and Eq. 1.15), and hence is found to alter the optical resonance conditions.

Throughout this section the optical selectivity, good energy resolution and high sensitivity of the CRESR technique are clearly demonstrated.

3.1 Optical characterisation

The photoluminescence (PL) spectrum of bulk $Cd_{0.995}Mn_{0.05}Te$ is shown in Fig. 3.1. This is acquired using the SFRS setup described in subsection 2.2.2. The three peaks in the high energy region (marked (c)), shown in more detail in the inset, can be attributed to the free, acceptor bound and donor bound excitons respectively. The free exciton energy (1.6038 eV) compares well to the calculated value (Eq. 1.5) of 1.6036 eV, assuming an exciton binding energy of 10 meV (subsection 1.2.1) and an effective Mn^{2+} ion concentration of 0.0048 (subsection 3.2.1). The measured energy separation of the free exciton from the donor and acceptor bound exciton states is 5 meV and 8 meV respectively. This is in good agreement with the literature [7, 50, 51].

The photoluminescence peak marked (b) is due to donor-acceptor (DA) pair emission [63]. This is separated in energy from peak (a) by 20 meV (170 cm^{-1}), the energy of an LO phonon in CdTe [64], so (a) is a LO phonon replica of (b). Recombination of an electron on a donor and a hole on an acceptor is possible if

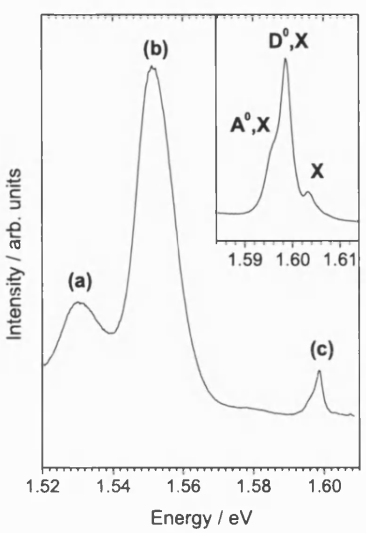

Figure 3.1: Photoluminescence spectra for bulk $Cd_{0.995}Mn_{0.05}Te$ at zero magnetic field: a) donor-acceptor pair + LO phonon; b) donor-acceptor pair; and c) free, donor bound and acceptor bound excitons. Inset magnifies region (c).

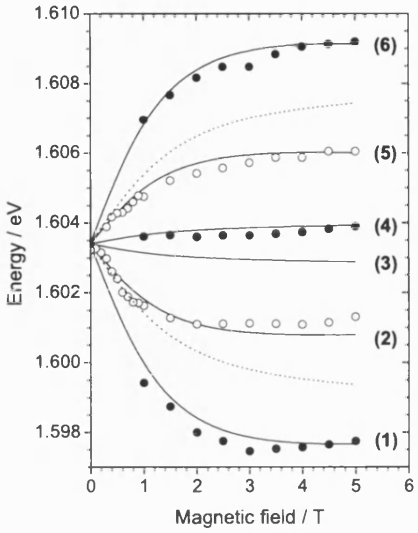

Figure 3.2: PLE data as a function of magnetic field in the Voigt configuration, for π (open circles) and σ (closed circles) transitions. Solid and dashed line denote optically allowed and forbidden transitions respectively. Numbers refer to transitions in Fig. 3.4.

their wave functions overlap. The energy of the emitted photon is [42]

$$\hbar\omega_{\mathrm{DA}} = Eg - E^{\mathrm{b}}_{\mathrm{D}^0} - E^{\mathrm{b}}_{\mathrm{A}^0} + \frac{e^2}{4\pi\varepsilon\varepsilon_0 r_{\mathrm{DA}}} - m\hbar\omega_{\mathrm{LO}}, \tag{3.1}$$

where Eg is bandgap energy, and $E^{\mathrm{b}}_{\mathrm{D}^0}$ and $E^{\mathrm{b}}_{\mathrm{A}^0}$ are the electron and hole binding energies to their respective centres. The fourth term is the Coulomb energy of the ionised centres after recombination: dependent upon the distance r_{DA} between the two centres. The final term gives the shift in energy due to a number m of LO phonons. DA pair emission is characterised by a blue shift with increasing excitation intensity. This is because as the laser power increases more centres become occupied; therefore, the average distance between them decreases, leading to larger a Coulomb term.

The photoluminescence excitation data for this sample, as a function of magnetic field, is shown in Fig. 3.2. The data is acquired using the same magnet, cryostat and scattering geometry as used for SFRS (subsection 2.2.2). The magnetic field is in the Voigt configuration ($\mathbf{B} \perp \mathbf{k}$). The incoming laser is modulated using a mechanical chopper, so lock-in detection can be used, and the laser is

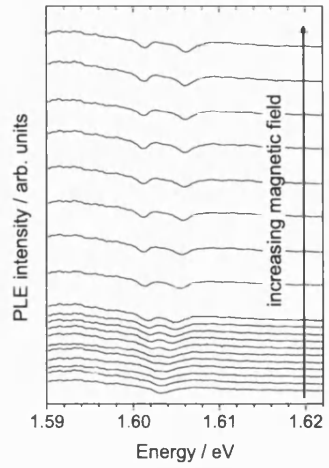

Figure 3.3: Typical PLE spectra obtained when monitoring DA pair emission. The excitation source is π polarised.

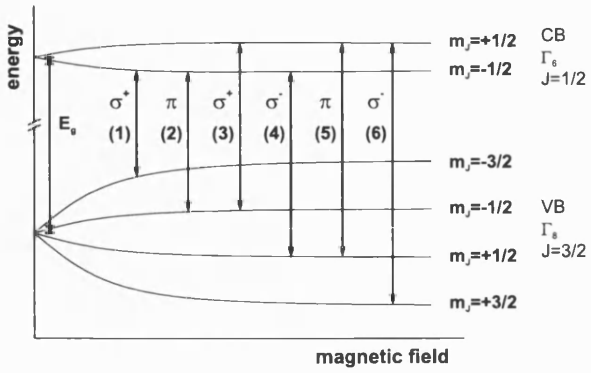

Figure 3.4: The Γ_6 conduction band (CB) and the Γ_8 valence band (VB) states, for $Cd_{1-x}Mn_xTe$, as a function of magnetic field. The numbered arrows indicate the allowed electric dipole transitions.

either polarised parallel (π) or perpendicular (σ) to the applied magnetic field. The luminescence is focussed onto the slit of a single grating monochromator spectrometer (similar to a SPEX minimate), which in this case is centred on the energy of the DA pair. As the laser is tuned through the excitonic region, the intensity of the DA pair luminescence is monitored, using an avalanche photodiode (APD).

The DA pair luminescence is strong and well separated in energy from the excitonic transitions of interest, therefore is ideal for PLE measurements. However, this leads to minima in the PLE spectra at energies relating excitonic transitions (Fig. 3.3), as opposed to the usual maxima observed, when monitoring the low energy side of the excitonic PL bands. This is because when the laser is in resonance with a transition, recombination between conduction and valence bands increases; therefore, there are fewer carriers available to occupy the donor and acceptor states. The PLE data gives a value of 1.6034 eV for the excitonic bandgap, in agreement with the PL and calculated value. The magnetic field dependence of the PLE signals is calculated from Eq. 1.14 and Eq. 1.15. For the free exciton, this gives six allowed transitions (Fig. 3.2, solid lines), two π transitions ($\Delta m = 0$) and four σ transitions ($\Delta m = \pm 1$), and two forbidden transitions (Fig. 3.2, dotted lines) with $\Delta m = \pm 2$. The allowed transitions (numbered 1 to 6) are shown schematically in Fig. 3.4. The calculation fits the experimental data well, although it was not possible to resolve the two central σ transitions ((3) and

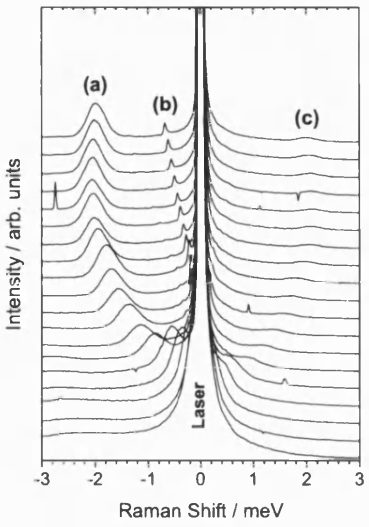

Figure 3.5: Spin-flip Raman spectra of bulk $Cd_{0.995}Mn_{0.05}Te$ for a series of magnetic fields, ranging from 0 T (bottom) to 6 T (top): a) electron spin-flip (Stokes); b) PMR (subsection 3.2.2); and c) electron spin-flip (anti-Stokes). The data has been normalised to the laser energy.

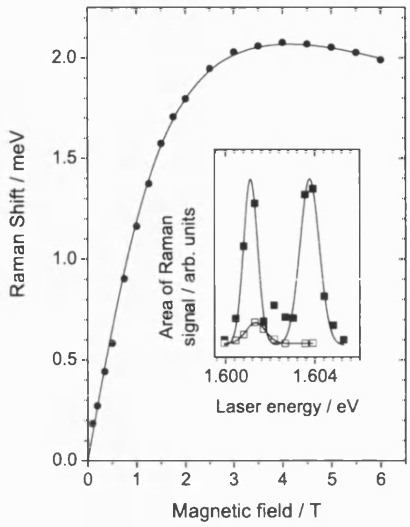

Figure 3.6: Raman shift of electron spin-flip signal, in $Cd_{0.995}Mn_{0.05}Te$, as a function of magnetic field (points). Fitted (line) with: $\bar{x} = 0.0048$ and $T_{\text{eff}} = 2.85$ K. Inset shows the signal's optical resonance profile at 0.5 T: Stokes (closed circles); and anti-Stokes (open circles).

(4)).

3.2 SFRS in CdMnTe

The bulk $Cd_{0.995}Mn_{0.05}Te$ sample produces strong spin-flip Raman signals. The optical resonance profile and magnetic field dependence of these signals provides the framework for the subsequent CRESR experiments.

3.2.1 Electron spin-flip

The Stokes and anti-Stokes (Fig. 3.5 (a) and (c)) components of the electron spin-flip Raman (ESF) signal [65, 66] are clearly observed in bulk $Cd_{0.995}Mn_{0.05}Te$. The average Raman shift of the two components is plotted (points) in Fig. 3.6. The magnetic field dependence of the band electron Zeeman splitting follows a

modified Brillouin curve, due to the *sp-d* exchange interaction (subsection 1.2.2). The energy separation of the two spin states is calculated using the expression

$$\Delta E_e = g_e \mu_B B - N_0 \alpha x_{\text{eff}} S B_S[g_{\text{Mn}} \mu_B S B/(k_B T_{\text{eff}})], \tag{3.2}$$

where $g_e = -1.67$ (from SFRS experiments), $g_{\text{Mn}} = 2$ (subsection 3.2.2), $N_0\alpha = 0.22$ eV [25] and $S = 5/2$. This provides a very good fit to the Raman shift (Fig. 3.6 (line)), assuming an effective Mn^{2+} concentration $\bar{x}$ of 0.0048 and effective temperature T_{eff} of 2.85 K. Above 4 T the energy splitting starts to decrease, due to the intrinsic Zeeman splitting of CdTe ($g_e \mu_B B$).

The inset of Fig. 3.6 shows the optical resonance profile of the ESF signal at 0.5 T, for the Stokes and anti-Stokes components, in other words, the relative intensity of the Raman peak as a function of laser energy. The Stokes component has two main resonance peaks at 1.6038 eV and 1.6011 eV. The higher energy peak is likely to be in resonance with the central σ transitions of the free exciton, because the scattering geometry is $z(\sigma, \pi)\bar{z}$. The second peak is either in resonance with the outer σ transition of the free exciton or the central σ transitions of a donor bound exciton.

3.2.2 Mn^{2+} paramagnetic resonance

The Raman line labeled (b) in Fig. 3.5 originates from the spin-flip of Mn^{2+} $3d^5$ electrons in CdTe, known as the electron paramagnetic resonance (PMR) signal. The Raman shift of this signal is plotted (points) in Fig. 3.7. A linear fit (line) gives $g = 1.99 \pm 0.01$, in agreement with the spin-flip Raman experiments of *Petrou* et al [67], who find $g = 2.01 \pm 0.01$. In the paramagnetic phase, the Mn^{2+}-Mn^{2+} exchange interaction energy (subsection 1.2.2) is less than the thermal energy kT; hence, Mn^{2+} ions behave independently of one another. The ground state of the $3d^5$ electrons has zero orbital angular momentum ($L = 0$), and spin orbital angular momentum $S = J = 5/2$. Since $L = 0$ there is no spin-orbit interaction, and g_{Mn} is equal to the Landé g factor (≈ 2).

The excitation energy is tuned to an energy of 1.6031 eV, in resonance with the free exciton energy (section 3.1), not the first excited state of the Mn^{2+} ion (Fig. 1.3), which is at a much higher energy of 2.2 eV. The Mn^{2+} $3d^5$ electrons and

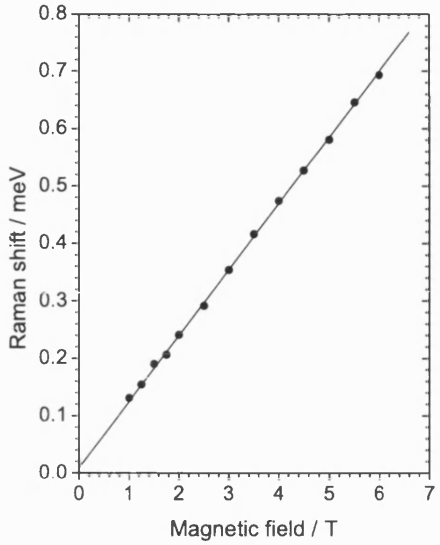

Figure 3.7: The Raman shift of Mn^{2+} PMR line (points) in CdTe as a function of magnetic field. Solid line is a linear fit to the data points, with $g = 1.99 \pm 0.01$.

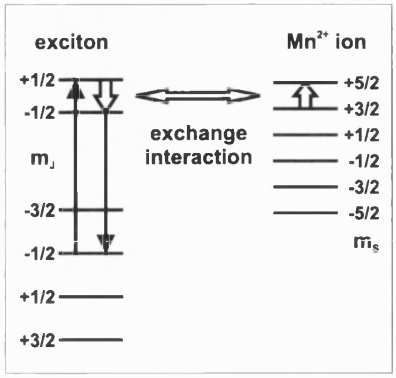

Figure 3.8: Raman mechanism (schematic) for Mn^{2+} PMR signal: left) free or weakly bound exciton, right) sixfold degenerate ground state of the Mn^{2+}.

band carriers are connected via the *sp-d* exchange interaction (subsection 1.2.2). The exchange Hamiltonian (Eq. 1.11) is dependent upon the term $\mathbf{S} \cdot \sigma$, where $\mathbf{S}$ and σ are the spin operators of the Mn^{2+} ion and the band carriers respectively. This term is described by [67]

$$\mathbf{S} \cdot \sigma = S^z \sigma^z + \frac{1}{2} S^+ \sigma^- + \frac{1}{2} S^- \sigma^+, \tag{3.3}$$

where S^z and σ^z are the spin operators along the z direction, and $S^\pm$ and $\sigma^\pm$ are the raising and lowering operators of the Mn^{2+} ion and the band carriers respectively. The second (third) term of Eq. 3.3 raises (lowers) the spin of the Mn^{2+} ion and simultaneously lowers (raises) the spin of the band carrier, as follows:

$$|m_S\rangle_{Mn^{2+}} |m_J\rangle \rightarrow |m_S + 1\rangle_{Mn^{2+}} |m_J - 1\rangle, \tag{3.4}$$

$$|m_S\rangle_{Mn^{2+}} |m_J\rangle \rightarrow |m_S - 1\rangle_{Mn^{2+}} |m_J + 1\rangle. \tag{3.5}$$

Here m_S and m_J are the magnetic quantum numbers of the Mn^{2+} ion and the band carriers respectively.

One of the possible Raman mechanism for the PMR process is shown in Fig. 3.8. In this case, there is a simultaneous spin-flip of a conduction band electron

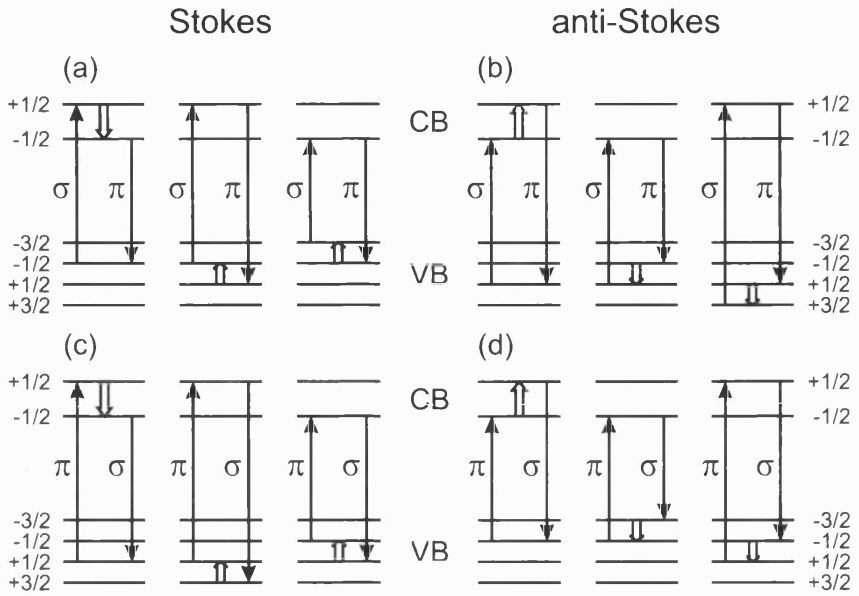

Figure 3.9: The Raman mechanism, in the Voigt geometry (B⊥k), for the Mn^{2+} PMR line involving the band carriers: a) Stokes ($\hat{\sigma}$, $\hat{\pi}$); b) anti-Stokes ($\hat{\sigma}$, $\hat{\pi}$); c) Stokes ($\hat{\pi}$, $\hat{\sigma}$); and d) anti-Stokes ($\hat{\pi}$, $\hat{\sigma}$). Single arrows represent virtual electronic dipole transitions between the conduction (CB) and valence (VB) band states, labeled by the quantum number m_J. Double arrows show the carrier spin-flip induced by the *sp-d* exchange interaction. Adapted from *Petrou* et al [67].

($\Delta m_J(\mathrm{e}) = -1$) and the Mn^{2+} ion ($\Delta m_S(\mathrm{Mn}^{2+}) = +1$), via the exchange interaction (Eq. 3.4). The incoming and outgoing photons are in resonance with the free exciton states. Here the spin-flip of the Mn^{2+} ion is between states $|3/2\rangle$ and $|5/2\rangle$, but it could equally occur between any two adjacent levels of the Zeeman multiplet. In total there are six Stokes ($|m_S\rangle_{\mathrm{Mn}^{2+}} \rightarrow |m_S + 1\rangle_{\mathrm{Mn}^{2+}}$) and six anti-Stokes ($|m_S\rangle_{\mathrm{Mn}^{2+}} \rightarrow |m_S - 1\rangle_{\mathrm{Mn}^{2+}}$) Raman processes allowed, shown in Fig. 3.9. These Raman mechanisms can either involve a conduction band electron spin-flip ($\Delta m_J(\mathrm{e}) = \pm 1$) or a valence band hole spin-flip ($\Delta m_J(\mathrm{h}) = \pm 1$). Both will induce a simultaneous spin-flip of the Mn^{2+} ion ($\Delta m_S(\mathrm{Mn}^{2+}) = \mp 1$).

An overtone of the Mn^{2+} PMR line (2PMR) is observed at twice the Raman shift of the PMR signal (Fig. 3.11 (a)). The Raman mechanism for 2PMR involves the spin-flip of two carriers ($\Delta m_J = \pm 2$), which induces two Mn^{2+} $3d^5$ electron spin-flips ($\Delta m_S = \mp 2$), via the *sp-d* exchange interaction. As can be seen in Fig. 3.10, the Raman process can either involve the spin-flip of two electrons, two holes or a single electron and a hole. Instead of two successive $3d^5$ electron spin-flips within the same Mn^{2+} ion, a Raman mechanism involving the spin-flip of two Mn^{2+} ions is much more likely. The polarisation selection rules for the

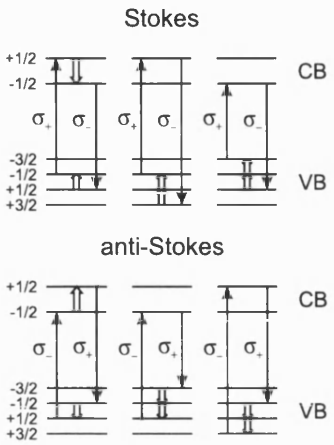

Figure 3.10: The Raman mechanism for the Stokes and anti-Stokes components of the Mn^{2+} 2PMR line involving a hole and an electron spin-flip. Adapted from *Petrou* et al [67].

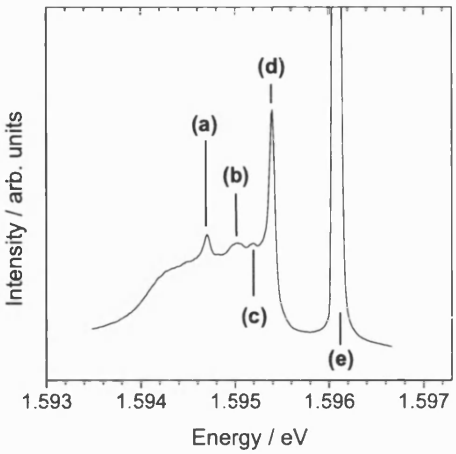

Figure 3.11: Spin-flip Raman spectra for bulk $Cd_{0.995}Mn_{0.05}Te$ at 6 T: a) 2PMR; b) 2J (nearest neighbour exchange); c) PMR + $2J_{NNN}$ (next nearest neighbour exchange); d) PMR; and e) laser.

Stokes and anti-Stokes components are (σ_+, σ_-) and (σ_-, σ_+) respectively. The spectra in Fig. 3.11 has been taken in the $z(\sigma, \pi)\bar{z}$ configuration, so the 2PMR line strictly should be forbidden. However, several examples of the 2PMR Raman line in this "forbidden" geometry can be found throughout the literature [67, 68].

3.2.3 Mn^{2+} pair spin-flip

The peak labeled (b) in Fig. 3.11, is attributed to the spin-flip of antiferromagnetically aligned Mn^{2+} pairs [69]. In this process, a spin-flip of a $3d^5$ electron in one ion changes the total spin of the pair from the ground state ($S_T = 0$) to the first excited state ($S_T = 1$). This shown schematically in Fig. 3.12 (a). The associated change in energy is magnetic field independent and can be calculated from Eq. 1.9, assuming $\Delta m = 0$ (the magnetic quantum number of the pair), to give

$$\Delta E_{\text{pair}} = -2J, \tag{3.6}$$

where J is the nearest neighbour exchange integral (subsection 1.2.2). The energy shift of the Mn^{2+} pair line is 1.09 meV; therefore, $|J/k_B| = 6.3$ K. This is consistent with current literature values: $J/k_B = -6.2 \pm 0.2$ K [70] and $J/k_B = -6.3 \pm 0.3$ K [23].

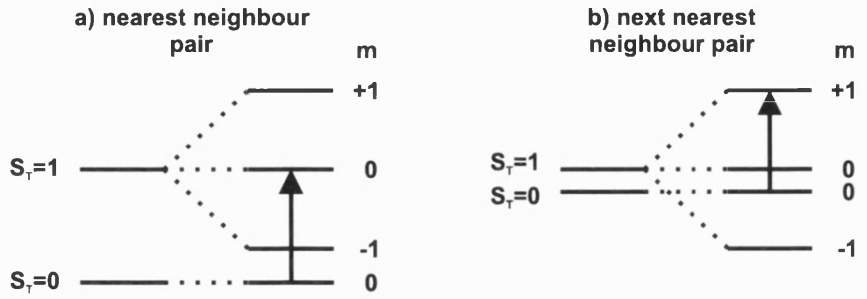

Figure 3.12: Spin-flip transitions in Mn^{2+} pairs at $B \neq 0$: a) nearest neighbour pair ($\Delta S_T = 1$, $\Delta m = 0$), b) next nearest neighbour pair ($\Delta S_T = 1$, $\Delta m = 1$).

Analogous to the PMR signal (subsection 3.2.2), the process is exciton induced, via the *sp-d* exchange interaction. Since $\Delta m = 0$, there must be no net change in magnetic quantum number of the band carrier ($\Delta m_J = 0$), i.e. incoming and outgoing photons must have identical polarisations. Therefore, like the 2PMR Raman signal, this Raman line should not be observed in the $z(\sigma, \pi)\bar{z}$ configuration. The incoming photon has an energy of 1.5961 eV; the laser could either be in resonance with the central states of the acceptor bound exciton or the lower energy states of the donor bound exciton.

The lower energy peak (c) is most likely due to the spin-flip of next nearest neighbour Mn^{2+} pairs, between the ground state $S_T = 0$ and $m = 0$ and the excited state $S_T = 1$ and $m = +1$, shown schematically in Fig. 3.12 (b). The energy separation between these two levels is

$$\Delta E_{\mathrm{NNN}} = -2J_{\mathrm{NNN}} - g_{\mathrm{Mn}}\mu_B B, \tag{3.7}$$

where J_{NNN} is the next nearest neighbour exchange integral. The Raman shift of this peak at 6 T is 0.69 meV, leading to $|J_{\mathrm{NNN}}/k_B| = 1.25$ K. This is comparable with the work of *Larson* et al [23], who find a value of $J_{\mathrm{NNN}}/k_B = -1.9 \pm 1.1$ K, from steps in the magnetic field dependent magnetisation.

3.3 Coherent Raman-detected PMR

This section focuses on coherent Raman-detected electron paramagnetic resonance in bulk $Cd_{0.995}Mn_{0.05}Te$ [71, 72]. This is the first application of the CRESR technique to a diluted magnetic semiconductor. At the start of the section the hy-

perfine interaction and cubic crystal field effects are introduced (subsection 3.3.1). Contributions from both of these effects are required to satisfactorily reproduce the coherent Raman lineshape (subsection 3.3.2). The relative intensity and phase of the signal is found to be dependent upon the laser energy and the microwave power: explored in detail in subsections 3.3.3 and 3.3.4 respectively.

3.3.1 Hyperfine and crystal field effects

The hyperfine interaction, is the interaction between electronic and nuclear magnetic dipole moments [55, 57]. This can either be thought of as the interaction between the nuclear magnetic moment and the magnetic field at the nucleus produced by the electronic magnetisation, or conversely, the interaction between electronic magnetisation and the magnetic field due to the nuclear magnetic moment. The hyperfine Hamiltonian is

$$H_{\text{hy}} = A\mathbf{I} \cdot \mathbf{J}, \tag{3.8}$$

where A is a material dependent parameter. $\mathbf{I}$ and $\mathbf{J}$ are the nuclear and electronic total angular momentum components respectively. These couple to form a new set of energy states with total angular momentum $\mathbf{F} = \mathbf{I} + \mathbf{J}$. The quantum number F takes values

$$F = (J + I), (J + I - 1), \ldots, |J - I|, \tag{3.9}$$

each of which is $2F + 1$ degenerate, with an energy of

$$E_F = \frac{1}{2}A[F(F + 1) - J(J + 1) - I(I + 1)]. \tag{3.10}$$

In the weak external magnetic field limit, where the Zeeman energy is smaller than the hyperfine energy ($g_J\mu_B\mathbf{J} \cdot \mathbf{B} < A\mathbf{I} \cdot \mathbf{J}$), the energy of each level is equal to $E_F + m_F g_F \mu_B B$. This is shown schematically for the hyperfine interaction between the Mn^{2+} $3d^5$ electrons ($\mathbf{J} = \mathbf{S} = 5/2$) and Mn^{2+} nucleus ($\mathbf{I} = 5/2$) in Fig. 3.13.

In a strong external magnetic field ($A \ll g_J\mu_B B$), the Back-Goudsmit region, the precession of the electronic magnetic dipole moment about the external magnetic field B is independent of the nuclear magnetic moment. This precession produces

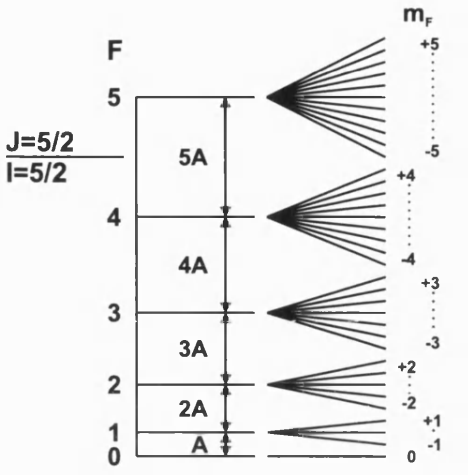

Figure 3.13: The Zeeman multiplet (schematic) for the hyperfine interaction between the Mn^{2+} $3d^5$ electrons ($\mathbf{J} = \mathbf{S} = 5/2$) and the Mn^{2+} nucleus ($\mathbf{I} = 5/2$), in the weak magnetic field case ($g_{\mathrm{Mn}}\mu_B \mathbf{B} \cdot \mathbf{J} < A\mathbf{J} \cdot \mathbf{I}$).

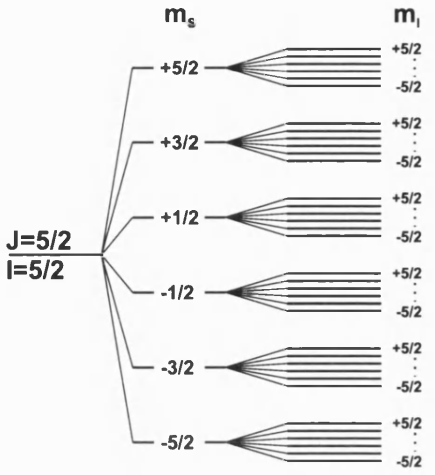

Figure 3.14: Schematic of the hyperfine splitting of the Mn^{2+} $3d^5$ electron states ($\mathbf{J} = \mathbf{S} = 5/2$), due to interaction with the Mn^{2+} nucleus ($\mathbf{I} = 5/2$), in the strong magnetic field case ($A \ll g_{\mathrm{Mn}}\mu_B B$).

a magnetic field B_e ($\parallel B$) at the nucleus, hence the nuclear magnetic moment precesses about a magnetic field $B + B_e$. In the same way, the precession of the nuclear magnetic moment produces a magnetic field B_n ($\parallel B$), so the electronic magnetic moment precesses about a magnetic field $B + B_n$. If B is along the z axis, then the magnetic hyperfine energy is

$$Am_I m_J \equiv g_J \mu_B m_J B_n \equiv g_I \mu_B m_I B_e, \tag{3.11}$$

where g_J (g_I) is the electronic (nuclear) g factor and m_J (m_I) is the electronic (nuclear) magnetic quantum number.

The total energy of the system is

$$E = g_J \mu_B m_J B + A m_I m_J - g_I \mu_B m_I B, \tag{3.12}$$

where the first term is the electronic Zeeman energy (Eq. 1.1), the second term is the hyperfine energy and the third term is the nuclear Zeeman energy. Typically the nuclear Zeeman energy is significantly smaller than the first two terms, allowing it to be neglected and Eq. 3.13 to be rewritten as

$$E = g_J \mu_B m_J (B + B_n). \tag{3.13}$$

Figure 3.14 shows the energy splitting of the Mn^{2+} ion ground state, in the strong

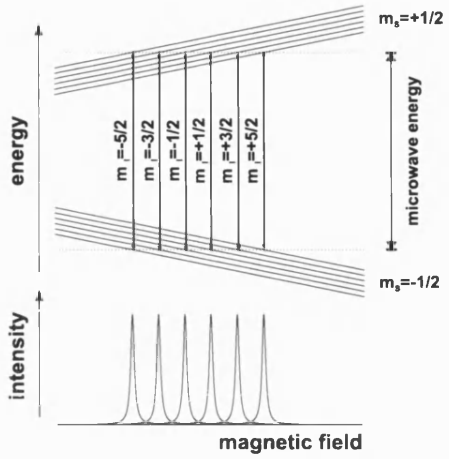

Figure 3.15: The hyperfine interaction between the Mn^{2+} $3d^5$ electrons and the Mn^{2+} nucleus leads to six equally spaced coherent Raman lines (absorption part shown).

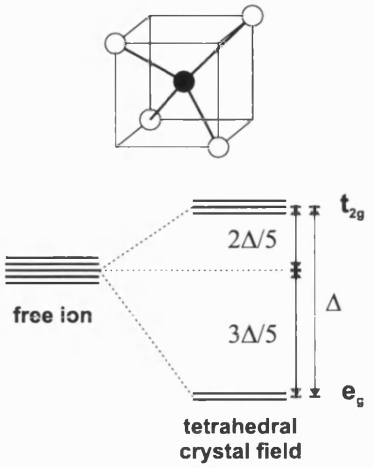

Figure 3.16: The cubic crystal field splitting in a tetrahedral environment. Adapted from Ref. [55].

magnetic field limit. Each of the six energy levels (m_S) of the Zeeman multiplet is split into a further six equally spaced levels (m_I) by the hyperfine interaction with the Mn^{2+} nucleus.

Assuming, during the Raman process there is no change in the nuclear spin ($\Delta m_I = 0$), there are six allowed spin transitions between adjacent m_S states ($\Delta m_S = \pm 1$), with energy

$$\begin{aligned} \Delta E &= (m_S + 1) g_{\mathrm{Mn}} \mu_B B + (m_S + 1) m_I A - m_S g_{\mathrm{Mn}} \mu_B B - m_I A \\ &= g_{\mathrm{Mn}} \mu_B B + m_I A. \end{aligned} \tag{3.14}$$

The change in energy is independent of m_S, so for clarity Fig. 3.15 shows the $\Delta m_I = 0$ transitions only between the $m_S = +1/2$ and $m_S = -1/2$ levels. For any fixed microwave energy, the CRESR PMR signal will consist of six equally spaced hyperfine components, separated in magnetic field by

$$\Delta B = \frac{A}{g_{\mathrm{Mn}} \mu_B}. \tag{3.15}$$

The separation is independent of the magnetic field and is shown for the absorption component in Fig. 3.15.

In addition to the hyperfine interaction, the Mn^{2+} $3d^5$ electron states are also perturbed by the cubic crystal field [55, 57]. The crystal field is the electric field

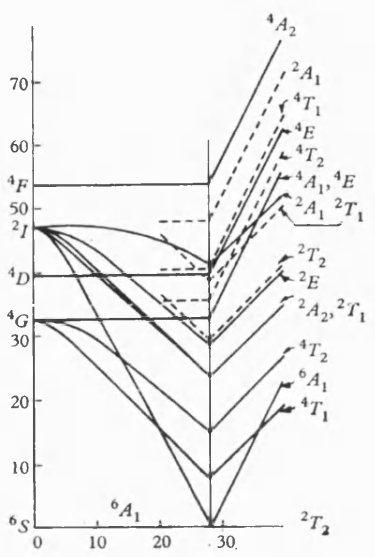

Figure 3.17: Tanabe and Sugano diagram [73] for the Mn^{2+} $3d^5$ band: energy (y-axis) against Δ (x-axis), both in units of $B = 860$ cm^{-1} (the Racah parameter). Taken from Ref. [74].

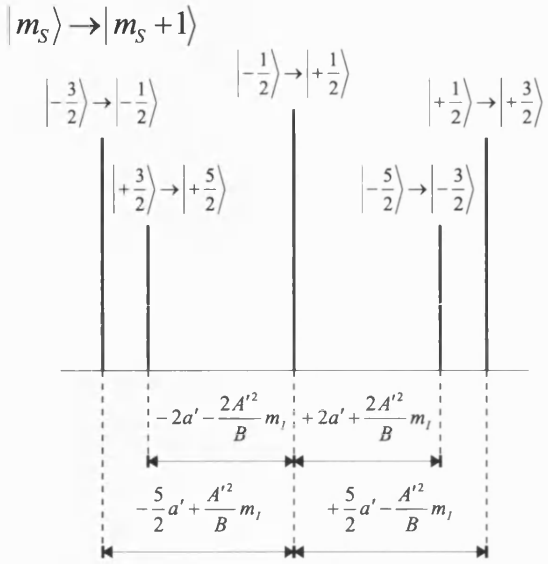

Figure 3.18: For a given m_I, the relative peak positions of the five CRESR lines split by the cubic crystal field. $A' = A/g_{\mathrm{Mn}}\mu_B$ and $a' = a/g_{\mathrm{Mn}}\mu_B$. Adapted from Ref. [75].

produced by the surrounding atoms. The Mn^{2+} d orbitals can be divided into two groups: the t_{2g} orbitals (d_{xy}, d_{xz} and d_{yz}), which point between the x, y and z axis; and the e_g orbitals, containing the d_{z^2} orbital (which points along the z axis) and the $d_{x^2-y^2}$ orbital (which has lobes pointing along the x and y axis). The crystal field emanates predominately from the p orbitals of neighbouring atoms, which point along the x, y and z axis (p_x, p_y and p_z). $Cd_{1-x}Mn_xTe$ is tetrahedrally bonded; therefore, the t_{2g} orbitals have a greater overlap with the p orbitals compared with the e_g orbitals. Hence, the t_{2g} orbitals are raised in energy and the e_g orbitals are lowered in energy. The t_{2g} and e_g orbitals are separated in energy by the parameter Δ (Fig. 3.16).

The simple model shown in Fig. 3.16 is fine for a single electron, but breaks down when considering more than one electron. As shown previously in subsection 1.2.1 (Fig. 1.3), the free ion Mn^{2+} has a ^6S ground state and excited states ^4G, ^4P ... etc. The application of a cubic crystal field changes $^6S \rightarrow {}^6A_1$, which is an orbital singlet, i.e. not split. However, the excited states are split by the crystal field in a manner which relates to the splitting Δ that occurs for a single electron. This behaviour was discussed by *Tanabe* and *Sugano* [73], the result is shown in Fig. 3.17, which shows how the free ion states are split in the presence of an

octahedral and tetrahedral crystal field.

The cubic crystal field is described by the Hamiltonian

$$H_{\rm cf} = a\left(S_x^4 + S_y^4 + S_z^4 - \frac{3}{5}S^4\right), \tag{3.16}$$

where a is the cubic field coefficient. The effect of the cubic crystal field is to split each of the six hyperfine lines into a further five lines, giving a total of thirty transitions [75]. For each of the six (m_I) sets of five crystal field lines, the magnetic field shift from the central component ($|m_S = -1/2\rangle \rightarrow |m_S = +1/2\rangle$) is (as given by [75])

$$|m_J\rangle \rightarrow |m_J + 1\rangle$$

$$\left|-\frac{3}{2}\right\rangle \rightarrow \left|-\frac{1}{2}\right\rangle; \quad \Delta B = -\frac{5}{2}\frac{a}{g_{\rm Mn}\mu_B} - \frac{5}{16}\frac{a^2}{g_{\rm Mn}^2\mu_B^2} + \frac{A^2 m_I}{g_{\rm Mn}^2\mu_B^2 B}, \tag{3.17}$$

$$\left|+\frac{3}{2}\right\rangle \rightarrow \left|+\frac{5}{2}\right\rangle; \quad \Delta B = -\frac{2a}{g_{\rm Mn}\mu_B} - \frac{2A^2 m_I}{g_{\rm Mn}^2\mu_B^2 B}, \tag{3.18}$$

$$\left|-\frac{5}{2}\right\rangle \rightarrow \left|-\frac{3}{2}\right\rangle; \quad \Delta B = +\frac{2a}{g_{\rm Mn}\mu_B} + \frac{2A^2 m_I}{g_{\rm Mn}^2\mu_B^2 B}, \tag{3.19}$$

$$\left|+\frac{1}{2}\right\rangle \rightarrow \left|+\frac{3}{2}\right\rangle; \quad \Delta B = +\frac{5}{2}\frac{a}{g_{\rm Mn}\mu_B} - \frac{5}{16}\frac{a^2}{g_{\rm Mn}^2\mu_B^2} - \frac{A^2 m_I}{g_{\rm Mn}^2\mu_B^2 B}. \tag{3.20}$$

The a^2 terms produce a negligible contribution to the shift, therefore can be ignored. The relative peak positions of the resultant coherent Raman crystal field components for a single hyperfine line are shown in Fig. 3.18. Based on the relative probability of each transition, the relative intensities of these peaks are in the ratio of $9 : 8 : 5$.

3.3.2 CRESR PMR spectra

The electron paramagnetic resonance of Mn^{2+} ions in cadmium telluride has been detected by coherent Raman ESR, using both a 13.7 GHz [71, 72] and a 33.7 GHz microwave source, as seen in Fig. 3.19 and Fig. 3.20 respectively. The simulated spectra, in both figures, are the resultant sum of thirty Lorentzian components, with the appropriate relative intensities, due to the hyperfine interaction between the Mn^{2+} $3d^5$ electrons and the Mn^{2+} nucleus, and the cubic crystal field (subsection 3.3.1). The coefficients $A/g_{\rm Mn}\mu_B = 5.9$ mT and $a/g_{\rm Mn}\mu_B = 3$ mT are used,

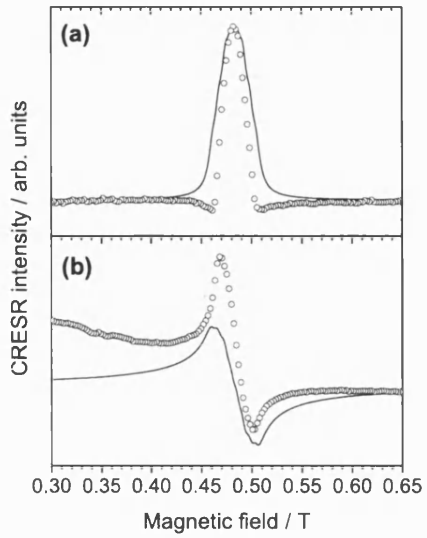

Figure 3.19: Coherent Raman-detected Mn^{2+} PMR signal (circles) in CdTe with a 13.7 GHz microwave source: a) absorptive-like component; b) dispersive-like component. The fit (lines) includes all thirty hyperfine and crystal field components.

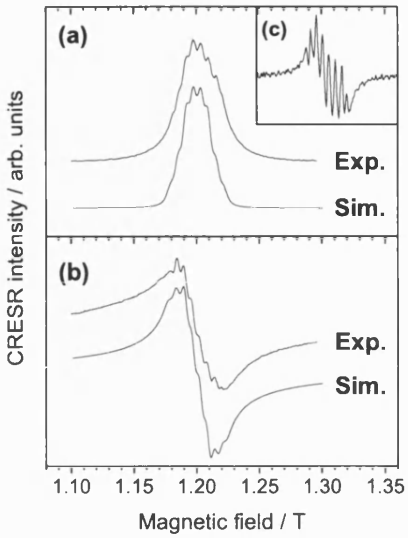

Figure 3.20: Experimental (exp.) and simulated (sim.) CRESR paramagnetic resonance signals in (Cd,Mn)Te detected with a microwave frequency of 33.7 GHz: a) absorptive-like component; b) dispersive-like component; and c) derivative of absorption signal.

consistent with the literature values [75]. The best fit to the experimental data is found when the full width at half maximum (FWHM) of each Lorentzian is 9 mT (13.7 GHz) and 7.5 mT (33.7 GHz). The higher FWHM of the 13.7 GHz data is due to the significantly higher microwave power used. The individual peaks are clearly resolvable in the 33.7 GHz spectra, emphasised by the first derivative of the absorption component (Fig. 3.20 (c)), where the hyperfine and crystal field structure is visibly larger than the noise level. It would not be possible to see this additional structure using spin-flip Raman spectroscopy.

In Fig. 3.19 (13.7 GHz data) there are obvious discrepancies between simulated and experimental data. The broad peak at low magnetic fields, most prominent in the dispersion component, is due to microwave modulated reflectivity effects [76]. The negative components of the absorption signal are due to overlapping Raman processes of opposing sign. These effects are explained in detail in chapter 4 and subsection 3.3.3 respectively. The spectra are centered at a magnetic field of 0.483 T (13.7 GHz) and 1.201 mT (33.7 GHz), leading to $g_{\mathrm{Mn}} = 2.03 \pm 0.03$ and $g_{\mathrm{Mn}} = 2.01 \pm 0.01$ respectively. The 13.7 GHz spectra has a much larger background signal and a faster magnetic field (B_0) scan rate, leading to a larger

error in the g factor obtained using this spectra compared with the 33.7 GHz spectra.

3.3.3 Optical resonance profile

The dependence of the coherent Raman-detected PMR signal on the excitation energy is shown in Fig. 3.21 (microwave frequency of 13.7 GHz) and Fig. 3.22 (microwave frequency of 33.7 GHz). For both frequencies, the signal is enhanced in the energy range of the free or weakly bound exciton (section 3.1). Photoluminescence excitation data of the excitonic states (Fig. 3.2) gives an energy range of 1.6015 eV – 1.6053 eV and 1.5995 eV – 1.6073 eV at 0.5 T and 1.2 T respectively. The Raman scattering mechanism (Fig. 3.23) is analogous to the one described for the spin-flip Raman PMR signal (subsection 3.2.2). At magnetic resonance the energy of the microwave photon is equal to the energy splitting of the Mn^{2+} $3d^5$ states (E_{PMR}). Incoming and outgoing photons are in resonance with excitonic states, not the first excited state of the Mn^{2+} ion, which is at a much higher energy (2.2 eV). In Fig. 3.23, the conduction band electron spin-flip ($\Delta m_J = -1$) is coupled to a spin-flip Mn^{2+} $3d^5$ electron band ($\Delta m_J = +1$) via the s-d exchange interaction (Eq. 3.3). In equivalent Raman processes (Fig. 3.9), the p-d exchange interaction couples the Mn^{2+} $3d^5$ electron flips to hole spin-flips in the valence band. In all these mechanisms, to produce the coherent Raman signal, spatial and temporal coherence must be conserved by the exchange interaction (represented by the arrow in Fig. 3.23).

Many of the spectra in Fig. 3.21 and Fig. 3.22 clearly deviate from the typical Lorentzian lineshape. This is particularly prominent at an excitation energy of 1.6000 eV and a microwave frequency of 33.7 GHz, where there appears to be a "dip" in the centre of the spectrum. These deviations can be explained in part by resonant heating effects [77]. At magnetic resonance there is a depolarisation of the Mn^{2+} ions, leading to a reduction in the conduction and valence band spin splitting (Eq. 1.14 and Eq. 1.15). This is shown in the magnetic field dependent plot of the exciton energy levels (Fig. 3.23 (left)). As the magnetic field is swept through magnetic resonance, the optical resonance conditions for the excitonic transitions will be continually changing. For a fixed excitation energy, the coherent Raman signal intensity will have a magnetic field dependence due to the optical resonance conditions, in addition to the spin resonant conditions.

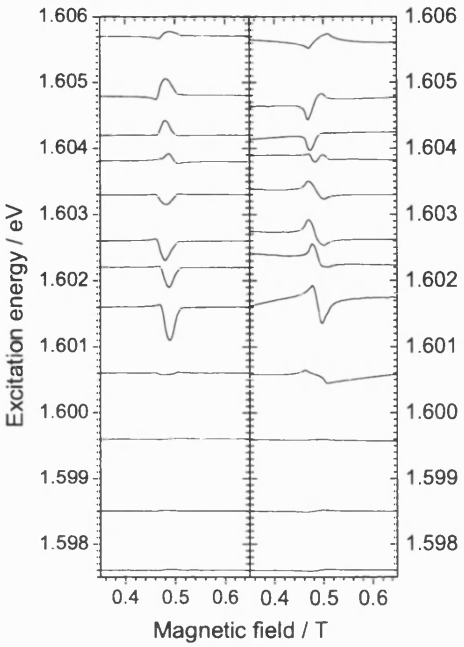

Figure 3.21: Excitation energy dependence of the absorption (left) and dispersion (right) coherent Raman components of the Mn^{2+} ion electron paramagnetic resonance signal, detected using a 13.7 GHz microwave source. The spectra are offset vertically so their zero level corresponds to the excitation energy shown on the y axis.

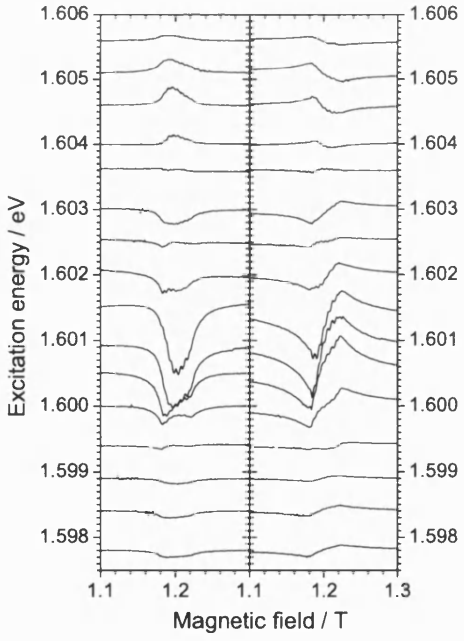

Figure 3.22: Excitation energy dependence of the absorption (left) and dispersion (right) coherent Raman components of the Mn^{2+} ion electron paramagnetic resonance signal, detected using a 33.7 GHz microwave source. The spectra are offset vertically so their zero level corresponds to the excitation energy shown on the y axis.

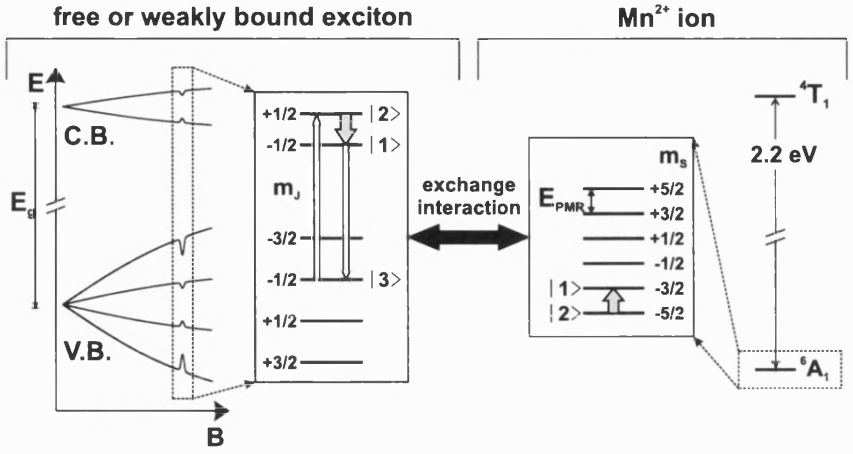

Figure 3.23: Expanded version of Fig. 3.8 showing schematically the scattering mechanism of the Mn^{2+} PMR signal. The changes in energy of the excitonic states (left) at magnetic resonance is due to microwave resonant heating effects. C.B. and V.B. refer to the conduction and valance band respectively.

An example of this is shown in Fig. 3.24, for three different excitation energies in resonance with the same exciton state. The change in energy of the exciton state with magnetic field is proportional to the change in CRESR signal intensity due to magnetic resonance. The change in signal intensity due to the change in optical resonance conditions only, i.e. the energy separation between the energy of the exciton E_{ex} and the laser E_{L}, can be seen in Fig. 3.24 (b). This has been weighted by a Lorentzian such that the intensity is

$$I_{\mathrm{op}} \propto \frac{1}{(E_{\mathrm{ex}} - E_{\mathrm{L}})^2 + \Gamma^2}, \tag{3.21}$$

where Γ is a broadening parameter. In the central plot the excitation energy crosses the exciton energy level at two magnetic fields, leading to two peaks in the optical resonance dependence, symmetric about the centre of the magnetic resonance. Figure 3.24 (c) shows the combined effect of the optical and spin resonance conditions on the coherent Raman signal intensity. Both the characteristic "dip" in the centre of the signal and the changing width of the signal have been observed in the experimental data. In these examples, the exciton level is assumed to have no magnetic field dependence in the absence of resonant heating effects. However, the field dependence of the excitonic states of $Cd_{1-x}Mn_xTe$ follow a Brillouin function, leading to a noticeable change in the optical resonance conditions as the magnetic field is swept.

In any Raman process, in addition to conservation of spin, energy must be con-

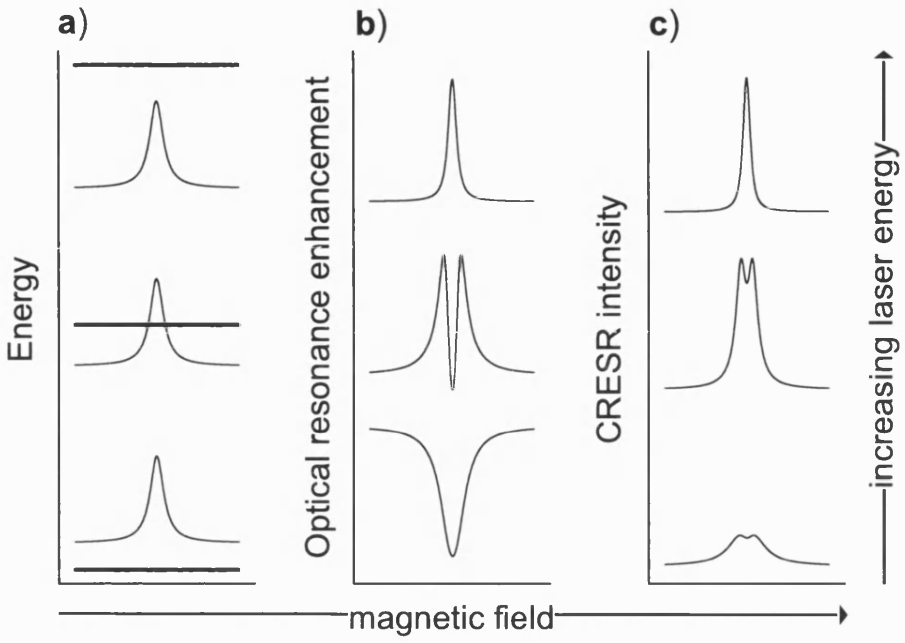

Figure 3.24: Schematic showing the possible changes in the absorption-like coherent Raman lineshape due to microwave resonant heating effects, for three different excitation energies: a) the relative energies of the excitonic transition (thin line) and the excitation source (thick line) as a function of magnetic field; b) the magnetic field dependence of the optical resonance; c) the resultant coherent Raman lineshape.

served. However, the spin splitting of the conduction and valence bands (ΔC and ΔV) are not equal in energy to the separation of the Mn^{2+} $3d^5$ electron states (E_{PMR}). At 1.2 T, the signal centre for the 33.7 GHz microwave source, $\Delta C = 1.05$ meV and $\Delta V = 1.5$ meV (neglecting resonant heating effects) are significantly larger than the $3d^5$ electron spin splitting ($E_{\mathrm{PMR}} = 0.14$ meV). The difference in energy is taken into account by the incoming and outgoing optical photons, shown schematically in Fig. 3.25. The peaks (Lorentzians, Eq. 2.7) on the right represent the scattering cross sections of the electric dipole transitions E_1 and E_2. The energy separation of the dashed lines is equal to the spin splitting of the $3d^5$ electron Zeeman multiplet. Here the Stokes process is shown, with incoming and outgoing photons in optical resonance with E_2 and E_1 respectively.

Assuming the electric dipole transitions E_1 and E_2 are π and σ polarised respectively, Fig. 3.25 shows only one of the four possible allowed scattering processes for an incoming photon of energy E_{L}. Remembering, that in the CRESR ex-

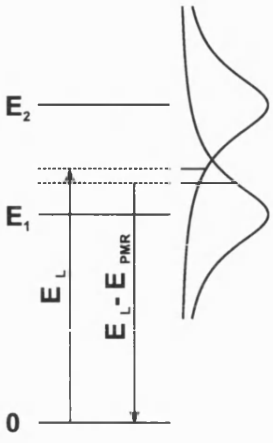

Figure 3.25: Incoming (E_{L}) and outgoing ($E_{\mathrm{L}} - E_{\mathrm{PMR}}$) photons in optical resonance with electric dipole transitions E_2 and E_1 respectively.

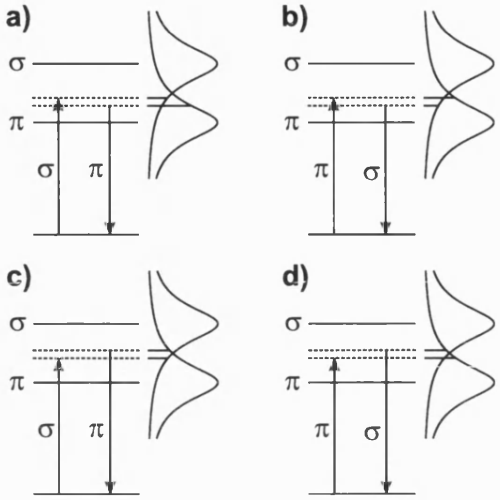

Figure 3.26: Raman scattering mechanisms: a) Stokes, $z(\sigma,\pi)\bar{z}$; b) Stokes, $z(\pi,\sigma)\bar{z}$; c) anti-Stokes, $z(\sigma,\pi)\bar{z}$; and d) anti-Stokes, $z(\pi,\sigma)\bar{z}$.

periment the sample is simultaneously excited with σ and π polarised light, the following mechanisms are allowed (Fig. 3.26): Stokes process, $z(\sigma,\pi)\bar{z}$; Stokes process, $z(\pi,\sigma)\bar{z}$; anti-Stokes process, $z(\sigma,\pi)\bar{z}$; and anti-Stokes process, $z(\pi,\sigma)\bar{z}$. The relative scattering intensities of these mechanisms, for a given laser energy E_{L}, is proportional to [68]

$$I \propto \left| \frac{M_{\mathrm{inc}} S_{\mathrm{ex}} M_{\mathrm{out}}}{\left((E_{\mathrm{L}} - E_{\mathrm{inc}}) - i\frac{\Gamma_{\mathrm{inc}}}{2}\right)\left((E_{\mathrm{L}} \pm E_{\mathrm{EPR}} - E_{\mathrm{out}}) - i\frac{\Gamma_{\mathrm{out}}}{2}\right)} \right|^2 . \tag{3.22}$$

Here M_{inc} and M_{out} are the electric dipole transition matrix elements of incoming and outgoing transitions, E_{inc} and E_{out} are the energy separations of the optically resonant states between which these transitions occur, S_{ex} is the $sp-d$ exchange interaction matrix element, and Γ_{inc} and Γ_{out} are the optical broadening terms; plus and minus E_{EPR} refer to anti-Stokes and Stokes processes respectively.

Between the six levels of the free exciton there are two electron (conduction band) and four hole (valence band) spin-flip processes allowed (Fig. 3.27). Multiplying this by the four different combinations (Stokes/anti-Stokes, $z(\pi,\sigma)\bar{z}/z(\sigma,\pi)\bar{z}$) possible for each spin-flip, yields a total of 24 coherent Raman mechanisms. To calculate the relative intensity of the coherent Raman ESR signal for a given

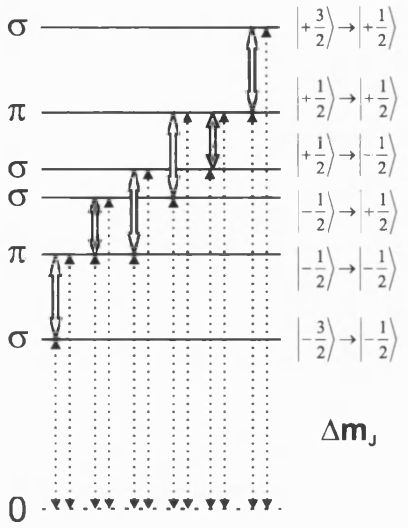

Figure 3.27: Allowed excitonic Raman transitions: two electron-flip processes, light grey; and four hole-flip processes, dark grey. Dashed lines show electric dipole transitions.

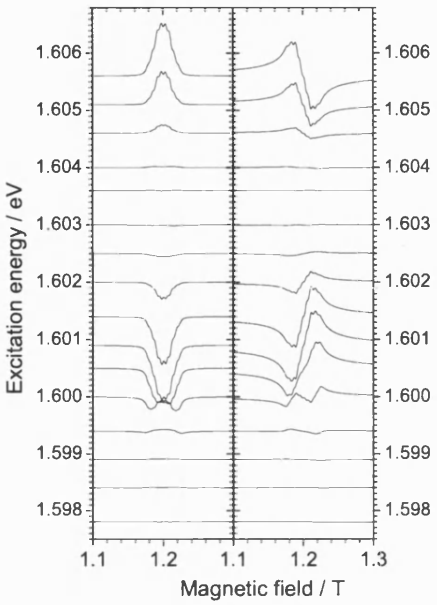

Figure 3.28: Simulation of the spectra presented in Fig. 3.22. All allowed PMR Raman processes (Fig. 3.9 and Fig. 3.27) are included in the fit.

excitation energy, the relative probability of all of these transitions must be taken into account, as follows

$$I \propto \left| \sum_{\substack{\mathrm{AS} \\ \pi\rightarrow\sigma}} x \right|^2 - \left| \sum_{\substack{\mathrm{AS} \\ \sigma\rightarrow\pi}} x \right|^2 - \left| \sum_{\substack{\mathrm{S} \\ \pi\rightarrow\sigma}} x \right|^2 + \left| \sum_{\substack{\mathrm{S} \\ \sigma\rightarrow\pi}} x \right|^2, \tag{3.23}$$

where

$$x = \frac{M_{\mathrm{out}} S_{\mathrm{ex}} M_{\mathrm{inc}}}{\left((E_{\mathrm{L}} - E_{\mathrm{inc}}) - i\frac{\Gamma_{\mathrm{inc}}}{2}\right)\left((E_{\mathrm{L}} \pm E_{\mathrm{EPR}} - E_{\mathrm{out}}) - i\frac{\Gamma_{\mathrm{out}}}{2}\right)}. \tag{3.24}$$

Here AS and S are the Stokes and anti-Stokes processes respectively, and $\pi \rightarrow \sigma$ ($\sigma \rightarrow \pi$) is where the incoming photon is in resonance with a π (σ) transition and the outgoing photon is in resonance with a σ (π) transition. The opposing signs of these different mechanisms originates from the 50 kHz polarization modulation of the laser. The calculation also assumes that heavy-hole processes are three times more likely than light-hole processes (appendix A).

The spectra in Fig. 3.22 (33.7 GHz microwave source) are simulated using Eq. 3.23, as shown in Fig. 3.28. A good fit to the experimental data is produced, with the inclusion of all thirty hyperfine and cubic crystal field components, and resonant

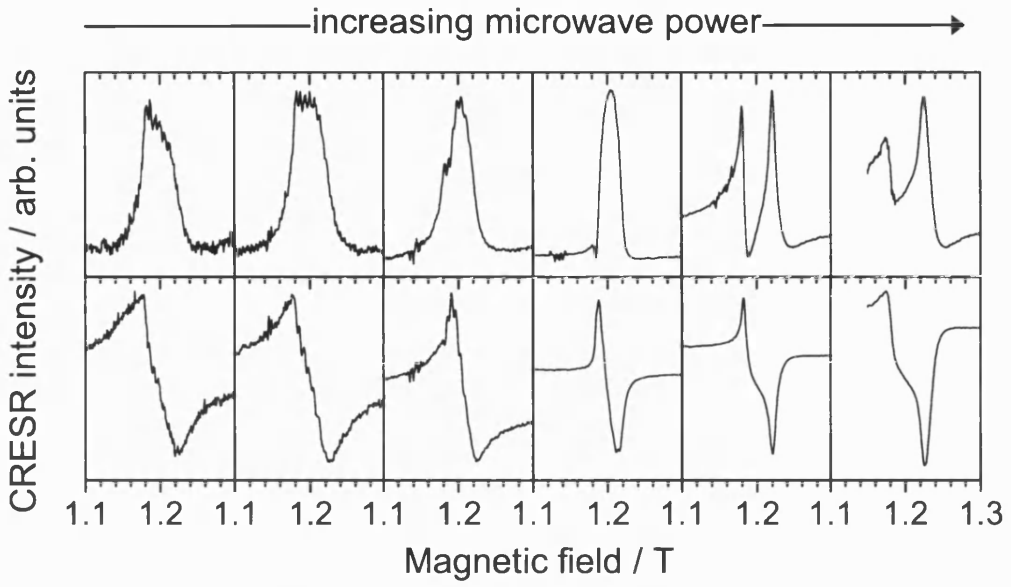

Figure 3.29: Microwave power dependence of the absorptive-like (top) and dispersive-like components of coherent Raman-detected Mn^{2+} paramagnetic resonance. The microwave power of each spectra is double the previous one.

heating effects. Unlike the simulated data, the signal intensity of the experimental spectra are not symmetric about the excitonic bandgap. At higher energies the laser is approaching the bandedge, so that direct excitation of e-h pairs becomes possible; the consequent absorption thus reduces the intensity of the resonant Raman scattering.

3.3.4 Microwave power dependence

The microwave power dependence of the coherent Raman-detected Mn^{2+} PMR signal in CdTe, at a microwave frequency of 33.7 GHz and a laser energy of 1.6018 eV, is shown in Fig. 3.29. The microwave power has been doubled in each successive spectrum, from left to right. When the microwave power is increased the sample temperature is also increased. As previously stated, the energies of excitonic states in a DMS are temperature dependent; hence, with each increase in microwave power, the optical resonance conditions will change. The observed effects are consistent with a changing exciton transition energy with respect to a fixed excitation energy, i.e. a changing FWHM followed by a separation into two peaks (Fig. 3.24).

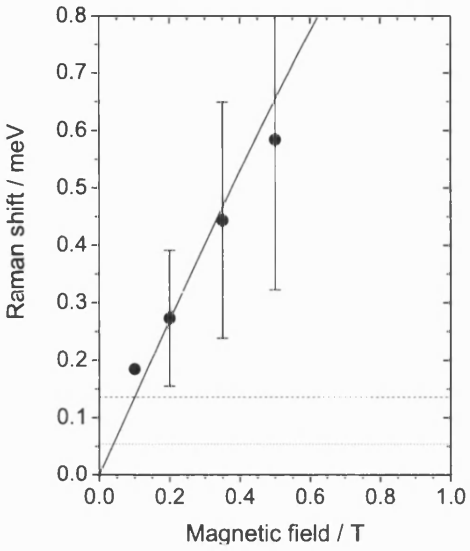

Figure 3.30: Experimental (points) and calculated (solid line) spin-flip Raman shift of the conduction band electron in $Cd_{0.995}Mn_{0.005}Te$, as a function of magnetic field. The error bars represent the FWHM of the SFR peak. The dotted and dashed horizontal lines show the energy of a 13.7 GHz and a 33.7 GHz microwave source respectively.

3.4 Absence of CRESR-detected ESF

In the spin-flip Raman spectra of the bulk $Cd_{0.995}Mn_{0.005}Te$ sample (section 3.2, Fig. 3.5), signals have been observed originating from Mn^{2+} electron paramagnetic resonance (PMR) and conduction band electron spin-flip (ESF). However, only the PMR signal has been detected by CRESR. Figure 3.30, shows the Raman shift of the ESF peak as a function of magnetic field. The FWHM of the Raman signal is represented by the error bars; it is proportional to the Zeeman splitting [78] and is significantly larger than the spin-flip Raman-detected PMR signal. The horizontal lines, in Fig. 3.30, are positioned at the energy of the 13.7 GHz and 33.7 GHz microwave sources respectively. The spin resonance condition is fulfilled at the magnetic field where these lines intercept the conduction band spin spitting (solid line). The large enhancement of the Zeeman shift, typical of DMS, means that the spin resonance magnetic field is very small for either of the microwave sources ($\sim$ 0.04 T and $\sim$ 0.1 T). This, coupled with the large linewidths associated with the ESF signal, is likely to be the main reason why no ESF has been detected by CRESR in this sample.

3.5 Summary

In this chapter, the first application of the coherent Raman ESR technique to a diluted magnetic semiconductor has been reported, using a bulk $Cd_{1-x}Mn_xTe$ sample, with $\bar{x} = 0.0048$ (measured by electron spin-flip Raman spectroscopy, Fig. 3.6). Figures 3.19 and 3.20 show coherent Raman-detected PMR, with a microwave frequency of 13.7 GHz and 33.7 GHz respectively. A good fit to the experimental data is obtained when all thirty components emanating from the hyperfine interaction between the Mn^{2+} $3d^5$ electrons and the Mn^{2+} nucleus, and the cubic crystal field are included (subsection 3.3.1). This additional structure is completely unresolvable in the spin-flip Raman spectra of the same signal (subsection 3.2.2).

The laser energy dependence of the CRESR PMR signal is plotted in figures 3.21 and 3.22. The incoming photons are in optical resonance with free or weakly bound exciton states, via the *sp-d* exchange interaction (Fig. 3.23), confirmed by photoluminescence and photoluminescence excitation spectroscopy data (section 3.1). Deviations from the typical Lorentzian lineshapes are found to be due to spin resonant heating effects (subsection 3.3.3). To satisfactorily simulate the excitation energy dependence (Fig. 3.28) the energy difference between the conduction or valence band splitting and the spin splitting of the $3d^5$ Mn^{2+} Zeeman multiplet must be taken into account (Eq. 3.21). An increase in microwave power increases the temperature of the system; hence, there is a change in the excitonic transition energies. For a fixed excitation energy, this leads to dramatic changes in the coherent Raman lineshape (Fig. 3.29).

The understanding gained in the CRESR work based on bulk $Cd_{1-x}Mn_xTe$ presented in this chapter, creates a good basis for the study of coherent Raman signals in more complicated structures, such as the finite quantum well structures discussed in chapter 5.

Chapter 4

Microwave-modulated magneto-reflectivity

In many of the coherent Raman ESR spectra, secondary, often much broader, signals are observed. These are attributed to microwave-modulated magneto-reflectivity (MMMR) effects. This chapter begins by considering the possible origin of these additional signals (section 4.1), before discussing the MMMR signals observed in a range of semiconductors. In bulk $Cd_{1-x}Mn_xTe$, the MMMR signals can be used to determine the energy of excitonic transitions (section 4.2). In GaAs and GaMnAs (section 4.3) no coherent Raman signals are detected, but strong MMMR signals relating to excitonic and Landau energy levels are observed.

4.1 Introduction to MMMR

The exact origin of the microwave-modulated magneto-reflectivity signals is still unclear, but they most likely arise from non-idealities in the experimental setup. For MMMR to be detectable by the experiment, the signal must be modulated at both the microwave frequency and the PEM (photoelastic modulator) frequency. Any model proposed must incorporate this modulation. A reasonable fit to MMMR signals, observed in ZnSe, has been shown [76] using both amplitude modulation of magnetic linear dichroism (MLD) and magnetic circular dichro-

ism (MCD). Dichroism is the polarisation dependent change in light absorption; hence, the reflected signal intensity is $I_{\mathrm{MLD}} = I_{\sigma} - I_{\pi}$ ($I_{\mathrm{MCD}} = I_{\sigma^+} - I_{\sigma^-}$) in the former (latter) case.

Strictly in an ideal system, MLD and MCD signals should be undetectable by the coherent Raman experiment. The MLD signals will not be modulated at 50 kHz, therefore not detected by the lock-in amplifier, but imperfections in the PEM could cause partial modulation of the σ and π components. The system is in the Voigt geometry ($\mathbf{B} \perp \mathbf{k}$), where σ^+ and σ^- components are indistinguishable; there should be no MCD signal either. However, if the sample is angled slightly, such that there is a component of the magnetic field B_0 parallel to the sample's growth axis ($\mathbf{B} \parallel \mathrm{k}$), an MCD signal could be detected. In both cases, to obtain an output from the quadrature mixer the reflected signal has to be modulated at the microwave frequency. It is possible that there is a microwave electric field component, in addition to the microwave magnetic field component, at the sample. This could amplitude-modulate the properties, such as linewidth, energy or intensity, of the electric dipole (excitonic or Landau level) transitions.

4.2 MMMR in bulk $Cd_{1-x}Mn_xTe$

Figure 4.1 is an expanded (in magnetic field and excitation energy) version of Fig. 3.21 (right), showing the CRESR signal intensity for bulk $Cd_{0.995}Mn_{0.005}Te$ (chapter 3) as a function of magnetic field, for a series of fixed excitation energies. The spectra have been offset vertically so that the zero field crossing of each spectrum corresponds to the excitation energy on the left-hand axis. The midpoint of the coherent Raman-detected Mn^{2+} PMR signal remains at 0.48 T (13.7 GHz microwave source), seen centrally in Fig. 4.1. The magnetic field position at which the significantly broader microwave-modulated magneto-reflectivity (MMMR) signal is centred is dependent upon the excitation energy.

The spectra in Fig. 4.2 have been taken under the same conditions as the spectra in Fig. 4.1, except here the signal intensity (dispersion channel) is monitored whilst the magnetic field is kept fixed and the laser energy is tuned. To do this a stepper-motor is used to scan the laser in incremental steps. The minimum feasible step size is ~ 0.25 Å or ~ 0.05 meV (in this energy region). The

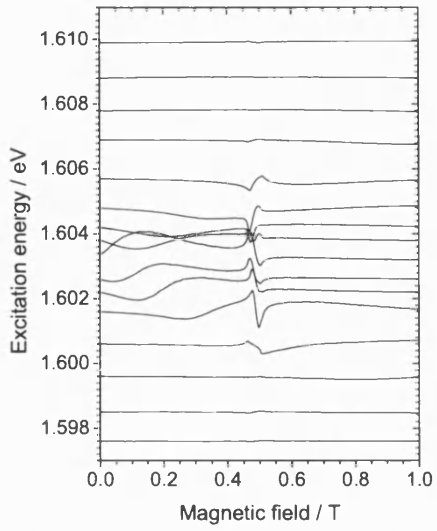

Figure 4.1: Expanded version of Fig. 3.21 (dispersion component). Coherent Raman ESR signal is centred at 0.48 T. The broader peaks (prominent at low magnetic fields) are due to microwave-modulated magneto-reflectivity signals. The microwave frequency is 13.7 GHz.

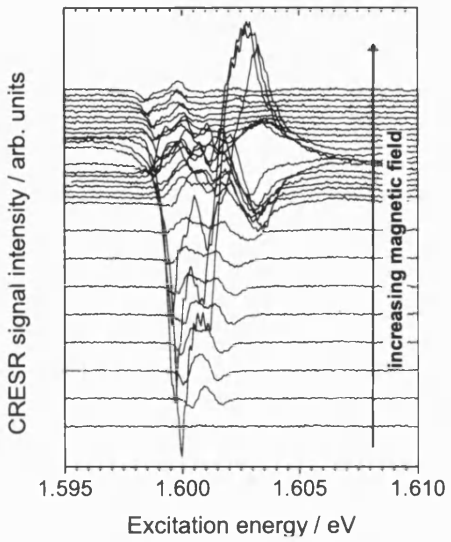

Figure 4.2: Coherent Raman signal intensity (dispersion channel) as a function of excitation energy, for a series of fixed magnetic fields (ranging from 0 T to 0.5 T) in bulk $Cd_{0.995}Mn_{0.005}Te$, at a microwave frequency of 13.7 GHz.

start and end excitation energies are measured using a diffraction based spectrometer, and the energy of individual data points are interpolated from this. Consequently, the resolution and accuracy of this method is less than that of the conventional coherent Raman ESR setup. However, it is a much more practical way of investigating these signals. For clarity purposes, the data in Fig. 4.2 and the equivalent in-phase data are shown as colour maps in Fig. 4.3 (bottom) and Fig. 4.3 (top) respectively. Superimposed onto these plots are the calculated σ (black lines) and π (white lines) polarised exciton transitions (Fig. 3.4). These have been calculated using the same method as has been used to fit the PLE data (Fig. 3.2) in section 3.1. The bandgap energy has been taken to be 1.6034 eV, in good agreement with theory (1.6036 eV), PL measurements (1.6038 eV) and PLE measurements (1.6034 eV). Neglecting the magnetic field region around the PMR signal (~ 0.44 T $\rightarrow \sim 0.54$ T), the σ and π polarised transitions correspond to troughs and peaks in the intensity of the reflected signal respectively. This would suggest that in this case the MMMR signal originates predominately from an amplitude modulated MLD process.

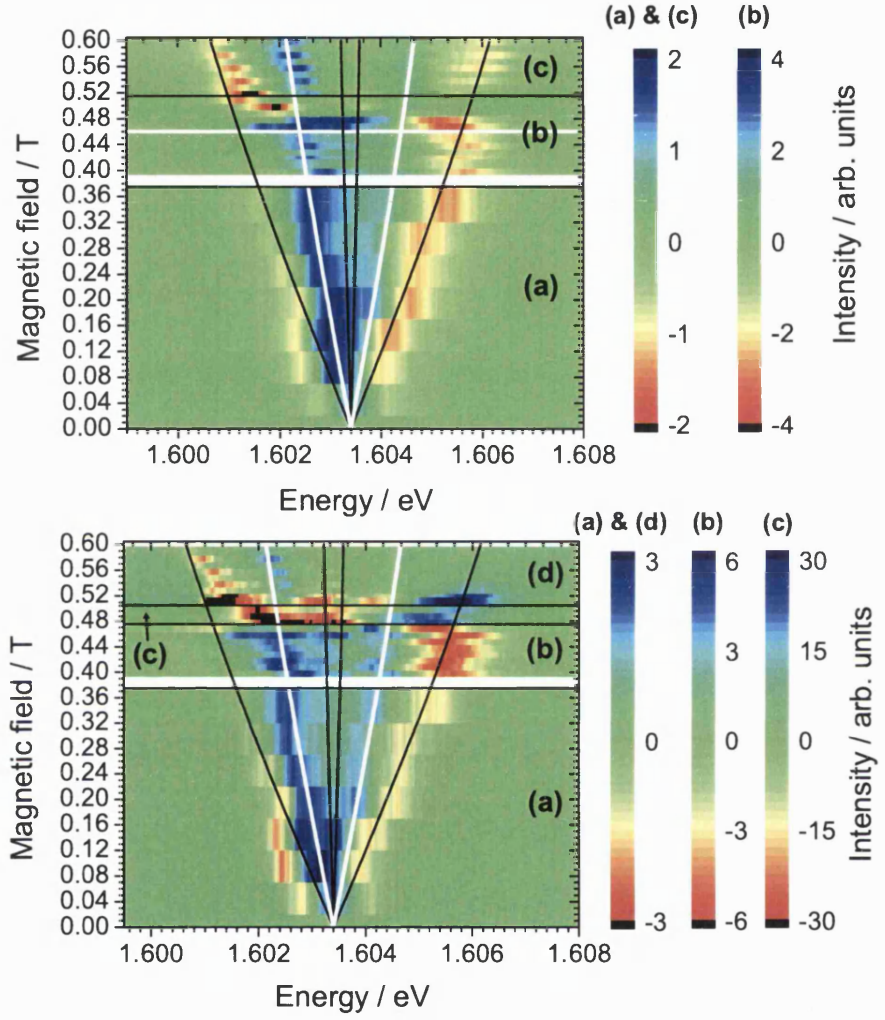

Figure 4.3: Colour map showing peaks (blue) and troughs (yellow & red) in the reflected signal intensity as a function of excitation energy and magnetic field; above) absorption channel; and below) dispersion channel (same data as Fig. 4.2). The microwave frequency is 13.7 GHz. Appropriate scaling for the different regions ((a), (b), (c) & (d)) have been chosen so trends can easily be observed. Superimposed are the calculated σ (black lines) and π (white lines) polarised free or weakly bound exciton transitions. The coherent Raman-detected PMR signal is in the magnetic field range ~ 0.44 T $\rightarrow \sim 0.54$ T. The change in magnetic field step size at 0.4 T is responsible for the white lines.

4.3 MMMR in GaAs and $Ga_{1-x}Mn_xAs$

In both GaAs and GaMnAs strong MMMR signals have been detected relating to excitonic and Landau level structure (subsections 4.3.2 and 4.3.3). However, no coherent Raman ESR signals have been detected in any GaAs based semiconductor. Possible explanations for this are discussed at the end of subsection 4.3.3. The section begins by giving an overview of these materials (subsection 4.3.1).

4.3.1 Introduction to GaAs and $Ga_{1-x}Mn_xAs$

The use of GaAs is widespread throughout the semiconductor industry, with particular focus on the application to optoelectronic and high speed electronic devices. It is a III-V semiconductor, with a tetrahedrally bonded zinc-blende structure [79, 80] and a lattice constant of 5.6533 Å [80]. The conduction band, light- and heavy-hole valence band, and spin split-off band have Γ_6, Γ_8 and Γ_7 symmetries respectively. GaAs has a direct bandgap ($\Gamma_8 - \Gamma_6$), which has a low temperature energy value of $E_g = 1.5195$ eV [81], and a valence band spin-orbit splitting of $\Delta_0 = 340$ meV [79]. The exciton binding energy in GaAs is $E_b = 4.2$ meV [81][82].

The current interest in DMS is largely due to their applicability to the area of spintronics (section ??). These are electronic devices which utilise the spin as well as the charge of carriers. $Ga_{1-x}Mn_xAs$ is of particular interest due to its compatibility with existing III-V electronics. Currently, Curie temperatures (the transition temperature between the ferromagnetic and paramagnetic phase) of $T_C \sim 160$ K have been achieved for $Ga_{1-x}Mn_xAs$ thin films [83]. Although above room temperature Curie temperatures have been measured in both MnAs/GaAs hybrid structures and paramagnetic $Ga_{1-x}Mn_xAs$ which contains ferromagnetic MnAs clusters [84, 85]. The ferromagnetism is most likely originating from a Ruderman-Kittel-Kasuya-Yosida (RKKY) type interaction [86]. In the case of $Ga_{1-x}Mn_xAs$, it is an indirect exchange interaction between Mn ions mediated by the holes. In pure $Ga_{1-x}Mn_xAs$, both an increase in Mn ion and hole concentrations is currently believed to be the key to raising T_C higher. Traditionally, $Ga_{1-x}Mn_xAs$ is grown using molecular beam epitaxy (MBE) [87]. However, the results reported in this thesis are based on a sample (appendix C) grown by

metal-organic-vapor-phase epitaxy (MOVPE) [88].

When there is no additional co-doping, Mn acts as an acceptor in GaAs, giving rise to a p-type material. The electronic configuration of the Mn ions is $3d^5 + h$ [89, 90]. Here manganese is a neutral acceptor (A^0). Co-doping can be used to produce n-type $Ga_{1-x}Mn_xAs$, for example $Ga_{1-x}Mn_xAs$:Te. In this case, the manganese ions are ionised acceptors (A^-), with a $3d^5$ configuration [89, 90]. It is also possible for the Mn ions to occupy interstitial sites in GaAs, which can then act as a double donor. Not only do these ions not contribute to the ferromagnetism, but they also decrease the T_C by reducing the number of holes, and by forming antiferromagnetic aligned pairs with nearby Mn ions on Ga lattice sites [91]. The *s-d* exchange interaction, like II-VI DMS, is ferromagnetic, with $N_0\alpha = 0.2$ eV [90]. On the other hand, the *p-d* exchange interaction is less understood in $Ga_{1-x}Mn_xAs$. In the p-type material the interaction is ferromagnetic, i.e. leading to a positive $N_0\alpha$: 3.3 eV [86]; 1.0–1.25 eV [90]; 2.5 eV [92]; 2.5 eV [93]; and 3–3.5 eV [94]. However, the *p-d* exchange interaction in n-type $Ga_{1-x}Mn_xAs$ is antiferromagnetic, with $N_0\alpha < 0$ [89, 92].

4.3.2 MMMR (GaAs)

Microwave-modulated magneto reflectivity signals have been detected (in a GaAs substrate) using the CRESR setup. The excitation energy dependence of these signals for a series of fixed magnetic fields is shown in Fig. 4.4. The data is acquired as described on page 58. The most intense-sharp set of peaks, observed at low energies, is assigned to the $1s$ exciton transitions. The energies of these transitions is given by the solutions of the Hamiltonian

$$H_{\text{ex}} = g_e\mu_B\mathbf{S}_{1/2}\cdot\mathbf{B} + \kappa\mu_B\mathbf{J}_{3/2}\cdot\mathbf{B} - \Delta_{eh}\mathbf{J}_{3/2}\cdot\mathbf{S}_{1/2} + DB^2. \qquad (4.1)$$

Here, the first and second terms are the conduction and valence band Zeeman terms respectively, the third term is due to the exchange interaction between the electron and hole, and the last term is the diamagnetic shift. The electron-hole exchange interaction term leads to a zero magnetic field splitting and an intermixing of the light- and heavy-hole valence band states. In bulk GaAs, Δ_{eh} is of the order of 0.1 meV [95].

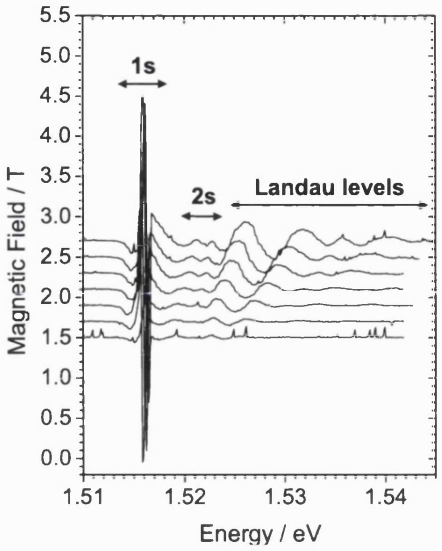

Figure 4.4: Microwave-modulated magneto-reflectivity signals in GaAs originating from $1s$ & $2s$ exciton states, and Landau levels. Spectra have been offset vertically such that their zero level corresponds to the external magnetic field on the y axis. The microwave frequency is 13.7 GHz.

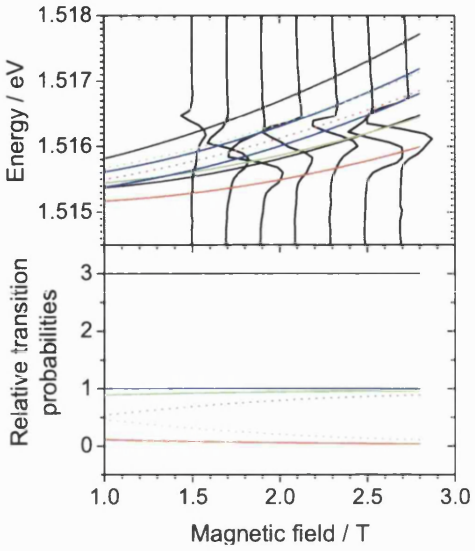

Figure 4.5: Top) calculated energies of the $1s$ exciton transitions (coloured lines) overlayed on the GaAs MMMR spectra. Bottom) calculated relative $1s$ excitonic transition probabilities as a function of magnetic field. See text for discussion.

In the Voigt configuration the diamagnetic shift of the π and σ components are given by [96]

$$D_\pi = \left(\frac{1}{2} - \frac{2}{5}\phi N - \frac{1}{2}\frac{\mu_0}{\mu_1}\right)\frac{e^2\hbar^2}{4\mu_0^2 R_0}, \tag{4.2}$$

$$D_\sigma = \left(\frac{1}{2} - \frac{2}{5}\phi N + \frac{1}{4}\frac{\mu_0}{\mu_1}\right)\frac{e^2\hbar^2}{4\mu_0^2 R_0}, \tag{4.3}$$

where

$$\phi = 8\left(\frac{\mu_0}{\mu_1}\right)^2 + \left(\frac{\mu_0}{\mu_2}\right)^2, \tag{4.4}$$

and

$$\frac{1}{\mu_0} = \frac{1}{m_e^*} + \frac{\gamma_1}{m_0}, \tag{4.5}$$

$$\frac{1}{\mu_1} = \frac{\gamma_2}{m_0}, \tag{4.6}$$

$$\frac{1}{\mu_2} = 2\sqrt{3}\frac{\gamma_3}{m_0}. \tag{4.7}$$

Here γ_1, γ_2 and γ_3 are the Luttinger parameters, m_e^* is the effective mass of

the electron, m_0 is the electron rest mass and R_0 is the effective Rydberg energy. Values of $D_\pi = 0.17$ meVT^{-2} and $D_\sigma = 0.22$ meVT^{-2} are obtained for GaAs using the following parameters [96, 97]: $\mu_0/m_0 = 0.044$, $\mu_1/m_0 = 0.415$, $\mu_2/m_0 = 0.088$, $R_0 = 3.86$ meV and $N = 0.4687$. The effective mass parameters are based on the following values [98, 97]: $m_e^* = 0.0665m_0$, $\gamma_1 = 7.65$, $\gamma_2 = 2.41$ and $\gamma_3 = 3.28$. In cadmium telluride the diamagnetic shift is significantly smaller, and hence has been neglected: $D_\pi = 0.03$ meVT^{-2} and $D_\sigma = 0.04$ meVT^{-2} (assuming $R_0 = 9.20$ meV [96], $\gamma_1 = 4.78$, $\gamma_2 = 1.77$ (section 1.1) and $\gamma_3 = 2.46$ [97], leading to $\mu_0/m_0 = 0.066$, $\mu_1/m_0 = 0.565$ and $\mu_2/m_0 = 0.117$).

The $1s$ exciton transition energies, and their associated relative probabilities, calculated using Eq. 4.1 are plotted in Fig. 4.5. The values $g_e = -0.44$ [99] and $\kappa = -2.4$ [81, 100] have been assumed. As the magnetic field increases the valence band transitions are tending towards their decoupled state: six allowed (two heavy-hole and four light-hol e exciton) transitions; and two forbidden transitions. This is seen clearly in the plot of the relative transition probabilities, which have been calculated from the squares of the dipole matrix elements. Overlaying the simulated $1s$ exciton transitions on top of the MMMR spectra (Fig. 4.5 top) shows agreement between the two. However, it is difficult to assign single transitions to individual maxima and minima due to the quality of the experimental data. The data points are separated in energy by ~ 0.8 meV, equating to approximately 6 data points for the main peaks in this energy region. Also, as discussed previously in section 4.2, the energies of the data points are interpolated from the measured excitation energies at the start and end of the scan. This method is based on the assumption that the stepper motor increases the energy of the laser by the same increment each time, which is unlikely to be the case. Since the acquisition of these sets of data, the experimental setup has been improved, such that the energy of the laser at each step is measured.

The second set of peaks in Fig. 4.4 have been assigned to the $2s$ exciton transitions. This is consistent with an energy separation of $E_x(1s) - E_x(2s) = 3.15 \pm 0.15$ meV measured by Sell [82]. The higher energy oscillations are attributed to transitions between the Γ_6 conduction band and Γ_8 valence band Landau levels [101]. The energy positions of the maxima and minima of these oscillations are plotted as solid and open circles respectively in Fig. 4.6. The following expression has been used to calculate the energies of the transitions

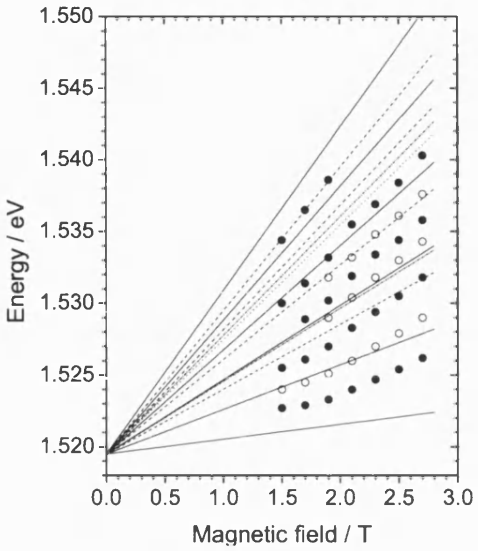

Figure 4.6: Maxima (solid circles) and minima (open circles) of the MMMR spectra (Fig. 4.4) in the Landau level energy region. The landau transitions (lines) have been calculated using Eq. 4.8: heavy-hole, $\Delta n = 0$ (solid line); heavy-hole, $\Delta n = 2$ (dashed line); light-hole, $\Delta n = 0$ (dotted line);and light-hole, $\Delta n = 2$ (dash-dot line).

between the Landau levels (Fig. 4.4 lines):

$$E_{\text{Lan}} = E_g + \frac{\hbar e B}{m_e^*}\left(n + \frac{1}{2}\right) + \frac{\hbar e B}{m_V^*}\left(n + \frac{1}{2}\right). \tag{4.8}$$

Here E_g is the energy gap, m_e^* ($0.0665m_0$ [98]) is the electron effective mass and m_V^* is the appropriate valence band effective mass ($m_{hh}^* = 0.35m_0$ and $m_{lh}^* = 0.08m_0$[1]). The Landau quantum number is $n = 0, 1, 2\ldots$ or $n = 2, 3, 4\ldots$ for the heavy- or light-holes respectively [102]. The selection rules for transitions between the conduction and valence Landau subbands at $\mathbf{k} = 0$ are [102, 103]: $\Delta n = 0$ and $\Delta n = 2$.

The inconsistencies between the experimental and simulated data observed in Fig. 4.4 are predominantly due to the failure of Eq. 4.8 to take into account the competition between exciton and Landau level effects. Nevertheless, it is clear that this is the correct assignment of these MMMR features. There are several likely reasons why Landau level structure is observed in the GaAs based materials, but is absent in the $Cd_{1-x}Mn_xTe$ MMMR spectra. Firstly, the exciton binding energy in GaAs is smaller than in CdTe, 4.2 meV compared to 10 meV; for $Cd_{1-x}Mn_xTe$, the excitation energy (in resonance with the free exciton) is sig-

[1] Assuming $1/m_{hh}^* = \gamma_1 - 2\gamma_2$ and $1/m_{lh}^* = \gamma_1 + 2\gamma_2$.

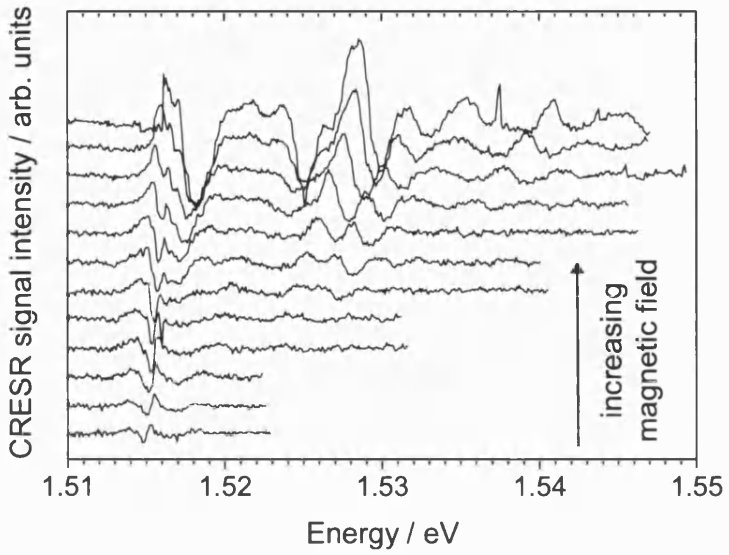

Figure 4.7: Microwave-modulated magneto-reflectivity spectra for $Ga_{1-x}Mn_xAs$ (#12697 appendix C) for a series of fixed magnetic fields ranging from 0.6 T to 2.8 T and for a microwave frequency of 13.7 GHz.

nificantly different from the energy of the Landau level transitions. Secondly, the number of carriers available to occupy the quantised Landau levels is significantly higher.

4.3.3 MMMR ($Ga_{1-x}Mn_xAs$)

Analogous to GaAs, MMMR spectra originating from excitonic and Landau level transitions has been detected in $Ga_{1-x}Mn_xAs$ (#12697 appendix C). Figure 4.7 shows the MMMR signal intensity as a function of excitation energy for a series of fixed magnetic fields ranging from 0.6 T to 2.8 T. Compared to the GaAs substrate the ratio of signal-to-noise is lower. For clarity, as in the case of the $Cd_{1-x}Mn_xTe$ spectra, the data in Fig. 4.7 has been shown as a colour map (Fig. 4.8). Overlaid are the six exciton transitions allowed by optical selection rules: four σ transitions (black lines); two π transitions (white lines). These have been calculated using a modified form of Eq. 4.1, where the electron and hole Zeeman terms are replaced with

$$\mathbf{S}_{1/2} \cdot (g_e \mu_B B - N_0 \alpha x_{\text{eff}} S_{\text{Mn}} B_S[g_{\text{Mn}} \mu_B S_{\text{Mn}} B/(k_B T_{\text{eff}})]) \tag{4.9}$$

and

$$\mathbf{J}_{3/2} \cdot (\kappa \mu_B B - \tfrac{1}{3} N_0 \beta x_{\text{eff}} S_{\text{Mn}} B_S[g_{\text{Mn}} \mu_B S_{\text{Mn}} B/(k_B T_{\text{eff}})]) \tag{4.10}$$

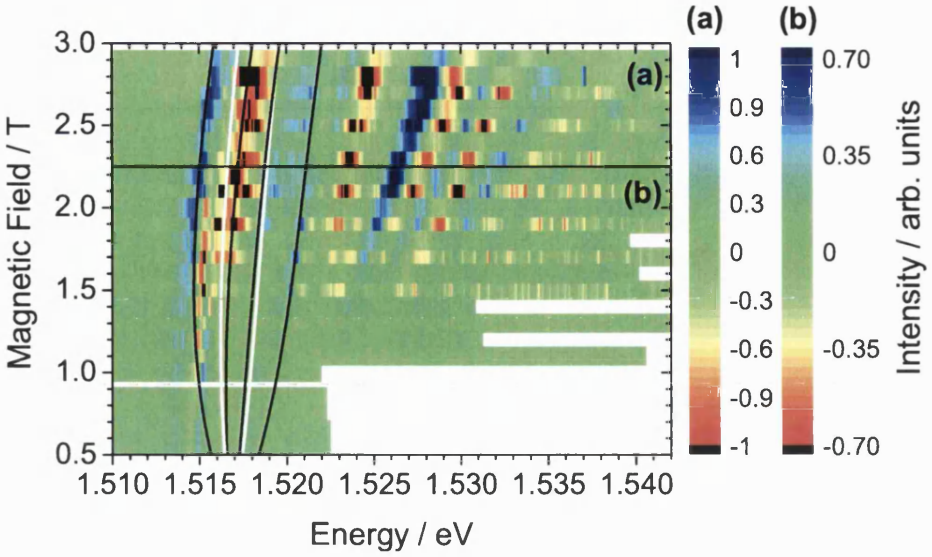

Figure 4.8: Colour map of the data in Fig. 4.7. Calculated energies as a function of magnetic field of the σ (black lines) and π (white lines) $1s$ exciton transitions have been overlayed.

respectively. Here g_e, κ, D_π, D_σ and Δ_{eh} are the same value as in GaAs (subsection 4.3.2). The precise manganese concentration is unknown, but it is thought to be between 0.1 % and 0.3 %. In addition, as discussed in subsection 4.3.1, there is still much debate on the value of $N_0\beta$. There is no co-doping in this sample; it is p-type and $N_0\beta$ will be positive. A good fit to the experimental data is found when $\bar{x} = 0.001$ and $N_0\beta = 3$ eV is assumed. The remaining structure is attributed to higher order excitonic and Landau level transitions. However, as in the case of GaAs, simulating this structure would be difficult.

Unlike $Cd_{1-x}Mn_xTe$, no CRESR signals have been detected in either GaAs or $Ga_{1-x}Mn_xAs$. For the 13.7 GHz microwave source used, coherent Raman signals are expected to be centred at a magnetic field of 2.2 T in GaAs (g_e) and 1.2 T in $Ga_{1-x}Mn_xAs$ (g_{Mn}). This is likely to be due to gallium arsenide's higher carrier mobilities [1, 104], and/or a larger carrier concentration in the GaAs based samples, influencing the microwave cavity resonance. When the laser is tuned into optical resonance with the sample, the cavity resonance broadens and shifts in frequency. This is caused by optically excited carriers, and could be preventing the observation of the CRESR signals. The next step would be to design a sample with a view to limiting the total number of carriers in the cavity.

4.4 Summary

In summary, microwave-modulated magneto-reflectivity signals have been detected, with the coherent Raman ESR experimental setup, in $Cd_{1-x}Mn_xTe$, GaAs and $Ga_{1-x}Mn_xAs$. These signals are believed to be a form of amplitude-modulated magnetic linear or circular dichroism. Although, both are strictly forbidden in the CRESR configuration, it is possible to explain their existence based on experimental non-idealities. Either there is a partial modulation of the σ and π components caused by an imperfect PEM, leading to an MLD signal, or the sample is at a slight angle such that there is a component of B_0 along the growth axis, leading to a MCD signal.

In $Cd_{1-x}Mn_xTe$, the energy position of the MMMR signals as a function of magnetic field strength are found to be consistent with free or weakly bound exciton transitions. The sign of the MMMR signal is different for the σ and π exciton transitions, suggesting that here the MLD process is prominent. In GaAs and $Ga_{1-x}Mn_xAs$ the spectra is much more complicated, with additional signals originating from higher order excitonic and Landau level transitions.

Importantly, all of the signals observed in the CRESR spectra, both expected and unexpected, have now been discussed.

Chapter 5

$Cd_{1-x}Mn_xTe/Cd_{1-x-y}Mn_xMg_yTe$ quantum wells

This chapter focuses on Raman scattering in $Cd_{1-x}Mn_xTe/Cd_{1-x-y}Mn_xMg_yTe$ single quantum wells (SQW). The energy of the excitonic states in the quantum well material differ from those of bulk $Cd_{1-x}Mn_xTe$ due to quantum confinement effects (section 5.1). The quantum well exciton levels are dependent upon the quantum well width, barrier height, and the effective mass of electrons and holes. Section 5.1 compares calculated values of the heavy-hole exciton ground state to photoluminescence and reflectivity spectra. Good agreement is found for a series of samples with a range of Mn and Mg concentrations, each containing four single quantum wells of varying well widths.

It is well known that large numbers of spin-flip Raman PMR overtones are often observed in $Cd_{1-x}Mn_xTe$ quantum wells in the Voigt configuration (section 5.2), the number of which increases as the quantum well width decreases. This is due to an exchange field $\mathbf{B}_{\text{exch}}$, created normal to the plane of the quantum well and perpendicular to the external magnetic field $\mathbf{B}_{\text{ext}}$. In the literature, spectra are only shown for $\mathbf{B}_{\text{exch}} \perp \mathbf{B}_{\text{ext}}$, the Voigt configuration. In section 5.3 the dependence of the number of multiple spin-flips n on the angle between the exchange and external magnetic fields is investigated. A reduction in n is found as the angle is decreased, consistent with theoretical predictions.

The key result of this chapter is the detection of the Mn^{2+} PMR signal in

$Cd_{1-x}Mn_xTe/Cd_{1-x-y}Mn_xMg_yTe$ single quantum wells by coherent Raman ESR (section 5.4). At very low microwave powers, saturation and resonant heating effects become negligible, allowing the CRESR signal to be fitted in accord with standard ESR theory. When the microwave power is increased, these effects are clearly evident (subsection 5.4.1). Like bulk $Cd_{1-x}Mn_xTe$ (chapter 3), the quantum well CRESR spectra are observed when the excitation source is tuned into resonance with free or weakly bound exciton states. In subsection 5.4.2, the ground state transitions of light- and heavy-hole excitons (for the widest quantum well), and their associated relative transition probabilities, have been calculated and compared directly to the optical resonance profile of the coherent Raman signal. Mn^{2+} PMR has been detected in single quantum wells with widths ranging from 301 Å to 45 Å (subsection 5.4.3). Even in the narrowest well a good signal-to-noise ratio is observed, emphasising the sensitivity of this technique.

5.1 Excitonic states in finite QWs

This section describes one method of calculating the energy of excitonic states at zero magnetic field in semiconductor based finite quantum wells [105]. The results of these calculations have been compared to photoluminescence and reflectivity data.

5.1.1 Theory

Consider the quantum well in Fig. 5.1. A carrier, with an effective mass m^* (appendix A), will be subjected to a potential V, such that

$$V(z) = \begin{cases} 0 & |z| > \frac{L}{2} \\ -V_b & |z| < \frac{L}{2} \end{cases} \tag{5.1}$$

where V_b is the potential barrier height of a finite quantum well of width L. Remembering the momentum operator is $p_z = -i\hbar\frac{\mathrm{d}}{\mathrm{d}z}$, the time independent Schrödinger equation is

$$\left(-\frac{\hbar^2}{2m^*}\frac{\mathrm{d}^2}{\mathrm{d}z^2} + V(z)\right)\phi(z) = E\phi(z), \tag{5.2}$$

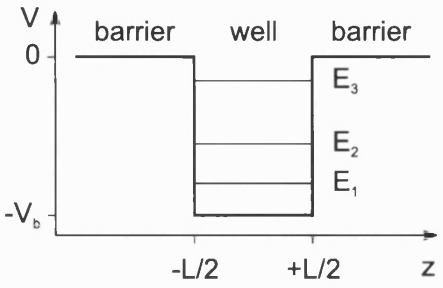

Figure 5.1: Energy schematic of a single finite quantum well of width L. Adapted from Ref. [105].

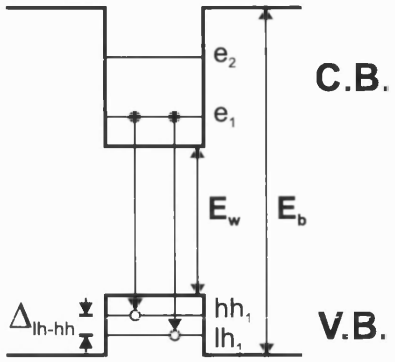

Figure 5.2: Type 1 quantum well with a 30% valence band offset. Terms are defined in the text.

and is equivalent to

$$\frac{\mathrm{d}^2}{\mathrm{d}z^2}\phi(z) + k(z)^2\phi(z) = 0, \tag{5.3}$$

where the wavevector $k(z)$ is

$$k(z) = \sqrt{\frac{2m^*}{\hbar^2}(E - V(z))}. \tag{5.4}$$

The solutions to Eq. 5.2 take the form

$$\phi(z) = A\sin(k_w x) + B\cos(k_w x) \qquad \text{in the well,} \tag{5.5}$$

$$\phi(z) = Ce^{-\kappa_b} + De^{+\kappa_b} \qquad \text{in the barrier,} \tag{5.6}$$

where the wavevectors of the well (k_w) and barrier (κ_B) are

$$k_w = \sqrt{\frac{2m^*}{\hbar^2}(E + V_b)}, \tag{5.7}$$

$$\kappa_b = \sqrt{-\frac{2m^*}{\hbar^2}E}. \tag{5.8}$$

The wavefunction $\phi(z)$ must satisfy the following boundary conditions:

1. $\phi(z)$ is continuous everywhere;
2. $\frac{1}{m^*}\frac{\mathrm{d}\phi(z)}{\mathrm{d}z}$ is continuous everywhere;
3. $\lim_{z\to\pm\infty}|\phi(z)|$ is finite.

Applying these boundary conditions, at the barrier-well interfaces ($z = \pm L/2$), gives

$$k_w \tan\left(k_w \frac{L}{2}\right) = \kappa_b \qquad \text{for even states,} \tag{5.9}$$

$$k_w \cot\left(k_w \frac{L}{2}\right) = -\kappa_b \qquad \text{for odd states.} \tag{5.10}$$

The solutions of Eq. 5.9 and Eq. 5.10 give the energy E of the

$$n = 1 + \text{Int}\left[\sqrt{\frac{2m^* V_b L^2}{\pi^2 \hbar^2}}\right] \tag{5.11}$$

bound states.

In $Cd_{1-x}Mn_xTe/Cd_{1-x-y}Mn_xMg_yTe$ quantum wells, the barrier height V_b is

$$V_b = (E_{ba} - E_w) \times 0.7 \qquad \text{for the electrons,} \tag{5.12}$$

$$V_b = (E_{ba} - E_w) \times 0.3 \qquad \text{for the holes,} \tag{5.13}$$

where E_{ba} and E_w are the energy gaps of the barrier and well material respectively (Fig. 5.2). This is equivalent to a valence band offset (VBO) of 30% [52]. The heavy-hole and light-hole excitonic groundstates are calculated from

$$E_g(hh) = E_w + E_{e1} + E_{hh1} - E_{bhh}, \tag{5.14}$$

$$E_g(lh) = E_w + E_{e1} + E_{lh1} - E_{blh}, \tag{5.15}$$

where E_{bhh} and E_{blh} are the heavy- and light-hole exciton binding energies respectively (expressions given in appendix B).

5.1.2 Comparison with experiment

Using Eq. 5.14 and Eq. 5.15 the ground state energies of the heavy- and light-hole excitons have been plotted (lines), as a function of quantum well width, in Fig. 5.3, for three different $Cd_{1-x}Mn_xTe/Cd_{1-x-y}Mn_xMg_yTe$ type quantum well structures (see figure caption). The following parameters have been used [5, 8, 52]: $m^*_{eb}/m_0 = 0.096(1-y) + 0.209y$, $m^*_{ew}/m_0 = 0.096$, $\gamma_{1w} = \gamma_{1b} = 4.78$, $\gamma_{2w} = \gamma_{2b} = 1.77$, $\epsilon/\epsilon_0 = 9.6$, and VBO = 30%. The energy gaps of the well [17]

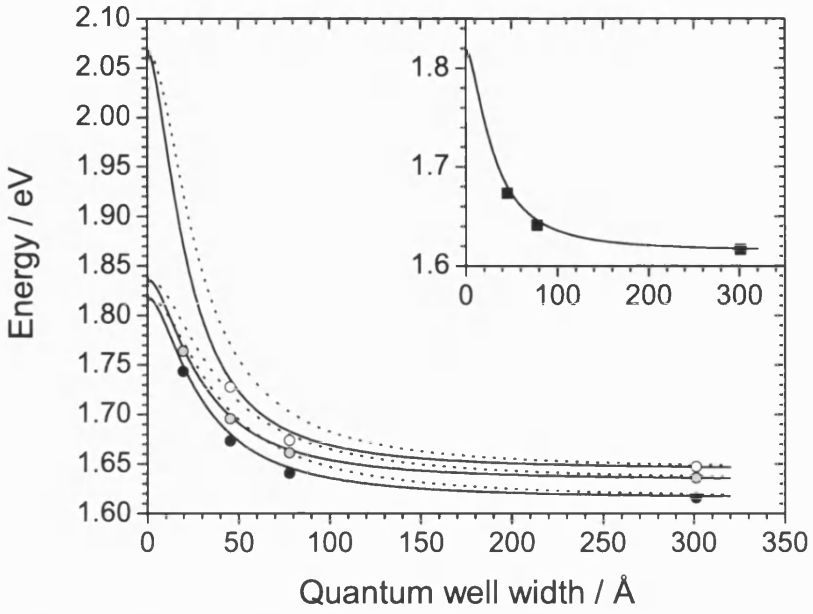

Figure 5.3: Plot of calculated heavy-hole (solid lines) and light hole (dotted lines) exciton ground state energies as a function of well width for a series of $Cd_{1-x}Mn_xTe/Cd_{1-x-y}Mn_xMg_yTe$ quantum wells: $x_{Mn} = 0.0116$ and $y_{Mg} = 0.12$ (bottom); $x_{Mn} = 0.023$ and $y_{Mg} = 0.12$ (middle); and $x_{Mn} = 0.03$ and $y_{Mg} = 0.25$ (top). Circles show the energy of the heavy-hole exciton ground state acquired from photoluminescence spectra (acquired at the University of Würzburg): $x_{Mn} = 0.0116$ and $y_{Mg} = 0.12$ (black); $x_{Mn} = 0.023$ and $y_{Mg} = 0.12$ (grey); and $x_{Mn} = 0.03$ and $y_{Mg} = 0.25$ (white). The inset compares the simulated line (same as lowest energy line in main plot) to reflectivity data (squares) for the heavy-hole exciton in the $Cd_{0.9884}Mn_{0.0116}Te/Cd_{0.8684}Mn_{0.0116}Mg_{0.12}Te$ quantum well. The reflectivity spectra have been acquired by D. Wolverson at the University of Bath.

(Eq. 1.5) and barrier [106] materials are:

$$E_w = (1.606(1-x) + 3.198x)\ \text{eV}, \tag{5.16}$$

$$E_{ba} = (1.606(1-x-y) + 3.198x + 3.306y)\ \text{eV}. \tag{5.17}$$

Analogous to bulk $Cd_{1-x}Mn_xTe$, there is a linear change in the exciton energy with manganese concentration. This is because x_{Mn} is constant throughout the structure; therefore, an increase in Mn will increases the bandgap of both the well and barrier materials, but does not change the potential barrier height. However, an increase in the concentration of magnesium will only increase barrier height, reducing the spread of the electron and hole envelope functions into the barrier and increasing the exciton energy for narrow quantum wells. By changing the Mn and Mg concentrations, and the width of the quantum well, it is possible to tune the bandgap of these structures over a significant energy range.

In Fig. 5.3, the calculated heavy-hole exciton energies are compared to experimental values obtained from photoluminescence (circles) and reflectivity (squares) experiments. The reflectivity results have been plotted separately (inset), because these overlap with the photoluminescence data points. Three samples have been included (appendix C): black) $x = 0.0116$ / $y = 0.12$ (#505A); grey) $x = 0.023$ / $y = 0.12$ (#505B); and white) $x = 0.03$ / $y = 0.25$ (#105A). Each sample contains four single quantum wells: 94 ML, 24 ML, 14 ML and 6 ML wide, where 1 monolayer of CdTe is equal to 3.24 Å. For all of the quantum wells[1] there is good agreement between theory and experiment.

5.2 Multiple Mn^{2+} spin-flip Raman scattering

In bulk $Cd_{1-x}Mn_xTe$ the optical selection rules, derived from conservation of angular momentum, only allow the Mn^{2+} PMR and 2PMR signals to be detected by spin-flip Raman spectroscopy (section 3.2). These signals correspond to one ($\Delta m_S = 1$) and two ($\Delta m_S = 2$) spin-flips, respectively, within the Zeeman energy levels of the ground state of the Mn^{2+} ion. By comparison, up to 13 simultaneous spin-flips have been observed in the spin-flip Raman spectra of a 19 Å wide $Cd_{0.9884}Mn_{0.0116}Te/Cd_{0.8684}Mn_{0.0116}Mg_{0.12}Te$ single quantum well, as shown in Fig. 5.4. Here, the laser has been systematically tuned through the energy range of the free or weakly bound heavy-hole exciton (X_{hh}), and the donor bound (D^0, X_{hh}) heavy-hole exciton dipole transitions. Analogous to the bulk material, the multiple PMR signals in this quantum well reach a maximum (in number and intensity) when the excitation source is in resonance with X_{hh}. In the same energy range, the conduction band electron spin-flip signal is also observed (circled in Fig. 5.4). From the magnetic field dependence of this signal a Mn^{2+} concentration of $x = 0.0116$ is obtained for this sample.

The number n of multiple spin-flip signals observed decreases with increasing quantum well width, as can be seen in Fig. 5.5. The Raman shift of the nth peak is

$$\Delta E_n = n g_{\mathrm{Mn}} \mu_B B. \tag{5.18}$$

The maximum number of possible simultaneous spin-flips within the ground state

[1]Note, no PL data is available for the 6 ML wide $Cd_{0.97}Mn_{0.03}Te/Cd_{0.72}Mn_{0.03}Mg_{0.25}$ quantum well because the exciton energy lies outside the tuning range of the laser.

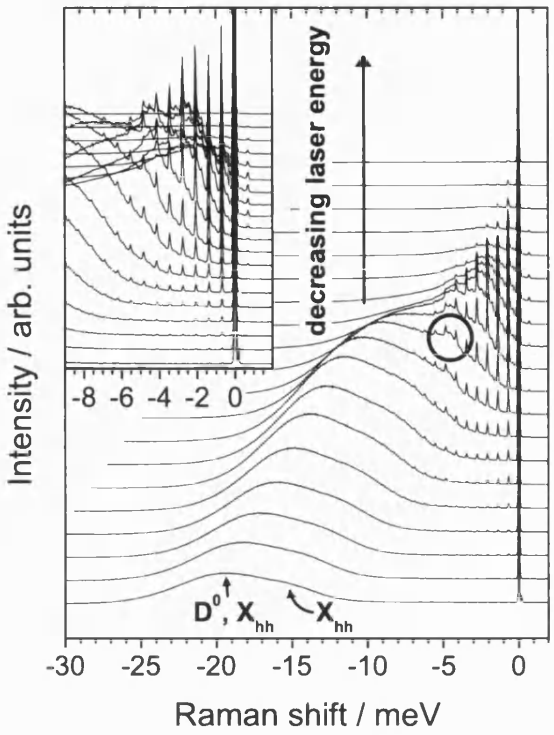

Figure 5.4: Excitation energy dependence of the multiple PMR signals and the broader conduction band electron spin-flip signal (circled) at 6 T for a 19 Å wide CdMnTe/CdMnMgTe ($x_{\mathrm{Mn}} = 0.0116$ and $x_{\mathrm{Mg}} = 0.12$) quantum well (#505A, appendix C). The PL peaks originating from the heavy-hole free and donor bound excitons are labeled (D^0, X_{hh}) and (X_{hh}) respectively. Data was acquired at the University of Würzburg.

Zeeman multiplet of a single Mn^{2+} ion is 5, but in the narrower wells $n > 5$ spin-flips are observed. Hence, the Raman mechanism must involve the simultaneous spin-flip of multiple Mn^{2+} ions [107, 108, 109]. In materials where there is a large splitting of the heavy- and light-hole states, such as in narrow quantum wells, the creation of a localised heavy-hole exciton will align the spins of the heavy-holes perpendicular to the external magnetic field, leading to an exchange field B_{exch} ($\perp B_{\mathrm{ext}}$). In the Voigt geometry the external magnetic field is parallel to the plane of the quantum well ($B_{\mathrm{ext}} \parallel x$). The spins of the Mn^{2+} ions inside the heavy-hole orbit precess around the effective magnetic field

$$\mathbf{B}_{\mathrm{eff}} = \mathbf{B}_{\mathrm{ext}} + \mathbf{B}_{\mathrm{exch}}. \tag{5.19}$$

When the exciton recombines there is no exchange field and only the external magnetic field along the x axis remains. Therefore, the initial and final eigenstates of the total spin of the $3d^5$ electrons S are no longer orthogonal, opening up new

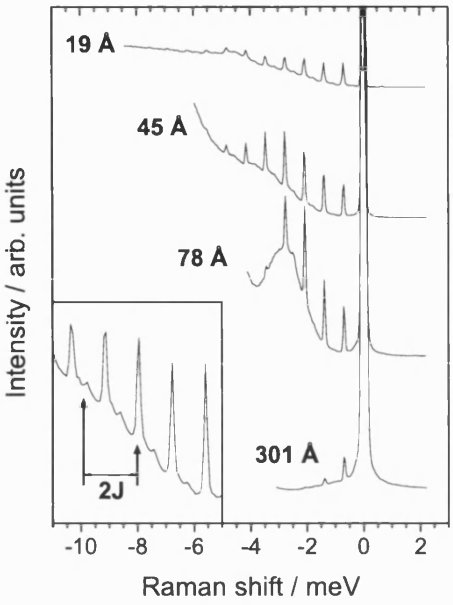

Figure 5.5: Spin-flip Raman spectra for CdMnTe/CdMnMgTe ($x_{\mathrm{Mn}} = 0.0116$ and $x_{\mathrm{Mg}} = 0.12$) single quantum wells (#505A, appendix C) at 6 T. The number of Mn^{2+} PMR overtones increases with decreasing quantum well width. The smaller peaks between PMR signals (inset) are due to nearest neighbour exchange effects. Data was acquired at the University of Würzburg.

optical paths. The outgoing photon is Raman shifted by the energy required to reorient the Mn^{2+} ions. The magnitude of the exchange field increases as the quantum well width decreases, therefore the number of spin-flips observed also increases.

Between every nth and nth+1 PMR overtone a second much weaker peak is observed, seen clearly in the inset of Fig. 5.5. These signals are due to the spin-flip of antiferromagnetically aligned Mn^{2+} pairs (subsection 3.2.3), and have a Raman shift of

$$\Delta E_{\mathrm{pair}(n)} = 2J + n g_{\mathrm{Mn}} \mu_B B, \tag{5.20}$$

where J is the nearest neighbour exchange integral.

5.3 Angle dependent PL and SFRS

This section looks at how the angle θ, between the external magnetic field and the z axis (parallel to the plane of the quantum well), affects both the PL spectrum

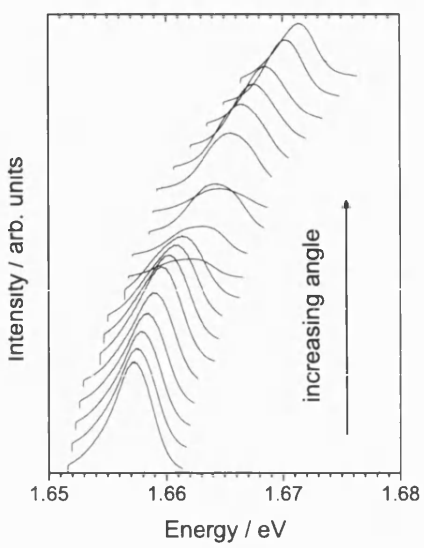

Figure 5.6: Photoluminescence spectra at 6 T as a function of the angle θ for a 45 Å wide CdMnTe/CdMnMgTe ($x_{\mathrm{Mn}} = 0.0116$ and $x_{\mathrm{Mg}} = 0.12$) quantum well (#505A, appendix C). θ ranges from 0° ($\mathbf{B}_{\mathrm{ext}} \parallel \mathbf{k}$) to 90° ($\mathbf{B}_{\mathrm{ext}} \perp \mathbf{k}$).

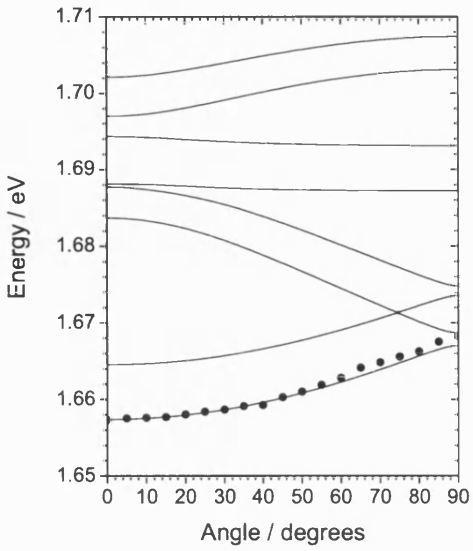

Figure 5.7: Comparison between the simulated (lines) excitonic transitions and PL data (points), as a function of angle θ, for a 45 Å wide CdMnTe/CdMnMgTe ($x_{\mathrm{Mn}} = 0.0116$ and $x_{\mathrm{Mg}} = 0.12$) SQW at 6 T.

(subsection 5.3.1) and the multiple PMR signals (subsection 5.3.2). Using the appropriate Hamiltonian, the energy of the lowest exciton transition as a function of angle, acquired from photoluminescence data, can be effectively modelled. The number of PMR overtone signals detected by spin-flip Raman Spectroscopy is directly related to θ. The number of overtones is at a maximum in the Voigt geometry ($\mathbf{B}_{\mathrm{ext}} \perp \mathbf{k}$) and decreases to just one peak when in the Faraday configuration ($\mathbf{B}_{\mathrm{ext}} \parallel \mathbf{k}$). Good agreement is found between experiment and theoretical predictions.

5.3.1 Angle dependent PL

Figure 5.6 shows the PL spectra for a 45 Å wide CdMnTe/CdMnMgTe ($x_{\mathrm{Mn}} = 0.0116$ and $x_{\mathrm{Mg}} = 0.12$) SQW as a function of angle θ, for an external magnetic field of 6 T. Here θ ranges from 0° (B_{ext} aligned along the growth axis, z direction) to 90° (B_{ext} aligned normal the growth axis, x direction), corresponding to the Faraday ($\mathbf{B}_{\mathrm{ext}} \parallel \mathbf{k}$) and the Voigt ($\mathbf{B}_{\mathrm{ext}} \perp \mathbf{k}$) configurations respectively. The broad PL band is the sum of two peaks originating from the lowest energy tran-

sition of both a donor bound and a weakly localised exciton. The peak position of the latter is plotted in Fig. 5.7 (points). The anisotropy of the excitonic transitions originates from the intermixing of the light- and heavy-hole states [110]. The degree of intermixing of these states, for a given quantum well, is dependent upon θ and the external magnetic field strength. Only when B_{ext} is aligned along the growth direction ($\theta = 0°$) do the light- and heavy-hole states decouple.

The energies of the excitonic transitions can be calculated (Fig. 5.7 (lines)) from the Hamiltonian

$$H_{\text{qw}} = H_{Ze} + H_{Zh} + H_{e-h} + H_{\text{con}}. \tag{5.21}$$

Here the first and second terms are the electron and hole Zeeman contributions respectively:

$$H_{Ze} = \mathbf{S}_{1/2} \cdot (g_e \mu_B B - N_0 \alpha x_{\text{eff}} S_{\text{Mn}} B_S[g_{\text{Mn}} \mu_B S_{\text{Mn}} B/(k_B T_{\text{eff}})]), \tag{5.22}$$

$$H_{Zh} = \mathbf{J}_{3/2} \cdot (\kappa \mu_B B - \tfrac{1}{3} N_0 \beta x_{\text{eff}} S_{\text{Mn}} B_S[g_{\text{Mn}} \mu_B S_{\text{Mn}} B/(k_B T_{\text{eff}})]). \tag{5.23}$$

The exchange interaction term H_{e-h} is given by

$$H_{e-h} = -\Delta_{eh} \mathbf{J}_{3/2} \cdot \mathbf{S}_{1/2} = -\Delta_{eh}(J^z S^z + \frac{1}{2} J^+ S^- + \frac{1}{2} J^- S^+), \tag{5.24}$$

where J^+ (S^+) and J^- (S^-) are the angular momentum raising and lowering operators for the hole (electron) respectively. The increased overlap of the electron and hole wavefunctions enhances the electron-hole exchange energy in quantum wells compared to the bulk value. Exact values of Δ_{eh} are not well known for CdTe. Here, a value of $\Delta_{eh} \sim 1$ meV has been assumed, based on calculations on GaAs/$Ga_{1-x}As_xAs$ quantum wells [95].

The final term in Eq. 5.21 is due to confinement effects. In CdTe, the light- and heavy hole states (Γ_8) can be considered separately from the spin split-off band (Γ_7) due to the large spin-orbit coupling; hence, the confinement term is given by [105, 111]

$$H_{\Gamma_8} = -\begin{bmatrix} H_{hh} & b & c & 0 \\ b^* & H_{lh} & 0 & c \\ c^* & 0 & H_{lh} & -b \\ 0 & c^* & -b^* & H_{hh} \end{bmatrix} \begin{bmatrix} \Phi_{3/2,3/2} \\ \Phi_{3/2,1/2} \\ \Phi_{3/2,-1/2} \\ \Phi_{3/2,-3/2} \end{bmatrix} = E \begin{bmatrix} \Phi_{3/2,3/2} \\ \Phi_{3/2,1/2} \\ \Phi_{3/2,-1/2} \\ \Phi_{3/2,-3/2} \end{bmatrix}, \tag{5.25}$$

where

$$H_{hh} = \frac{\hbar^2}{2m_0}[(\gamma_1+\gamma_2)(k_x^2+k_y^2)+(\gamma_1-2\gamma_2)k_z^2]+V_b(z), \quad (5.26)$$

$$H_{lh} = \frac{\hbar^2}{2m_0}[(\gamma_1-\gamma_2)(k_x^2+k_y^2)+(\gamma_1+2\gamma_2)k_z^2]+V_b(z), \quad (5.27)$$

$$b = -\frac{\sqrt{3}i\hbar^2}{m_0}\gamma_3(k_x-ik_y)k_z, \quad (5.28)$$

$$c = \frac{\sqrt{3}\hbar^2}{m_0}[\gamma_2(k_x^2-k_y^2)-2i\gamma_3 k_x k_y]. \quad (5.29)$$

Here γ_1, γ_2 and γ_3 are the Luttinger parameters, and k_x, k_y and k_z are the wavevectors in the x, y and z directions. The excitonic transitions measured by PL experiments occur near or at the Γ point, therefore $k_x = k_y = 0$ can be assumed [110], and the matrix in Eq. 5.25 can be simplified to

$$H_{\Gamma_8} = -\begin{bmatrix} \frac{\hbar^2k_z^2}{2m^*_{hh}}+V_b(z) & 0 & 0 & 0 \\ 0 & \frac{\hbar^2k_z^2}{2m^*_{lh}}+V_b(z) & 0 & 0 \\ 0 & 0 & \frac{\hbar^2k_z^2}{2m^*_{lh}}+V_b(z) & 0 \\ 0 & 0 & 0 & \frac{\hbar^2k_z^2}{2m^*_{hh}}+V_b(z) \end{bmatrix}. \quad (5.30)$$

This matrix takes the same form as the strain Hamiltonian (Eq. 2.11), i.e.

$$H_{\Gamma_8} = -\frac{1}{2}\Delta_{\text{lh-hh}}\left(J_z^2-\frac{1}{3}J^2\right), \quad (5.31)$$

where $\Delta_{\text{lh-hh}}$ is the energy separation of the light- and heavy-hole states. Solving Eq. 5.31 and the other terms in Eq. 5.21 leads to the simulated excitonic transitions in Fig. 5.7 (lines). Good agreement is found between the calculated lowest energy exciton transition and the PL data Fig. 5.7 (points).

5.3.2 Angle dependent SFRS

The number n spin-flip Raman-detected Mn^{2+} PMR overtones decreases as the angle θ between $\mathbf{B}_{\text{ext}}$ and $\mathbf{B}_{\text{exch}}$ decreases (Fig. 5.8). The maximum value of n is found in the Voigt configuration ($\mathbf{B}_{\text{ext}} \perp \mathbf{k}$). The energy positions of the excitonic transitions, and hence the optical resonance conditions, are dependent upon θ (subsection 5.3.1). This is taken into account, in the acquisition of the spectra in Fig. 5.8, by tuning the excitation source to maximise the number of

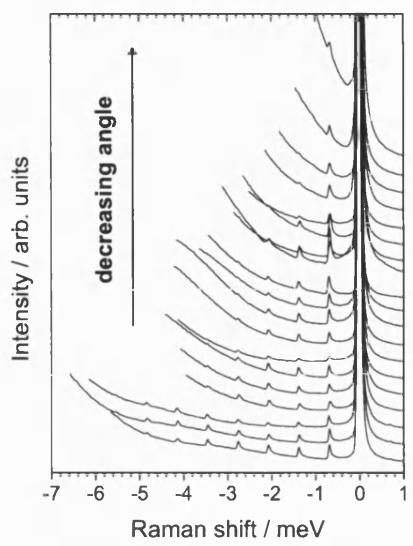

Figure 5.8: Spin-flip Raman spectra as a function of angle θ for a 45 Å single wide CdMnTe/CdMnMgTe ($x_{\mathrm{Mn}} = 0.0116$ and $x_{\mathrm{Mg}} = 0.12$) quantum well (#505A, appendix C) and a magnetic field of 6 T. The angle θ ranges from 0° to 90°.

peaks observed at every angle. In addition, over the energy range of the multiple PMR peaks there is more than one resonance present. This can be observed in the Voigt geometry as an enhancement of the Raman signal intensity around the $n = 4$ peak. Both the angle dependence of the excitonic transitions and the multiple optical resonances, make direct comparison with theoretical simulations difficult.

It has been shown previously (section 5.2), that the multiple PMR peaks in the Voigt configuration are due to the production of an exchange field normal to the plane of the quantum well by localised heavy-hole excitons. The external magnetic field ($\mathbf{B}_{\mathrm{ext}} \parallel x$) is normal to the growth axis; therefore, the Mn^{2+} ions precess about to an effective magnetic field $\mathbf{B}_{\mathrm{eff}}$ (Eq. 5.19). The intensity $P_n(\tau)$ of the nth peak can be calculated using a Poisson distribution [107, 112, 113]

$$P_n(\tau) = \frac{1}{\tau}\int_0^\infty \mathrm{d}t\, e^{-t/\tau}\frac{N(t)^n}{n!}e^{-N(t)}, \tag{5.32}$$

where τ is the lifetime of the exciton and $N(t)$ is the average change in the total spin of the Mn^{2+} ions interacting with the exciton, given by

$$N(t) = \int_V \mathrm{d}V\; n'_{\mathrm{Mn}} S \sin\delta(1 - \cos(\omega_L t)). \tag{5.33}$$

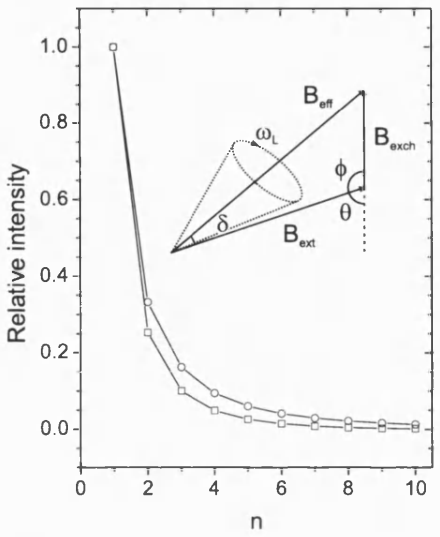

Figure 5.9: Relative intensity (simulated) of n simultaneous spin-flips for $\mathbf{B}_{\text{ext}} = 6$ T in the Voigt configuration ($\theta = 90°$): circles) $\mathbf{B}_{\text{exch}} = 2$ T; and squares) $\mathbf{B}_{\text{exch}} = 1.2$ T. The Mn^{2+} ions precess about an effective magnetic field $\mathbf{B}_{\text{eff}} = \mathbf{B}_{\text{ext}} + \mathbf{B}_{\text{exch}}$ at a frequency of ω_L (inset).

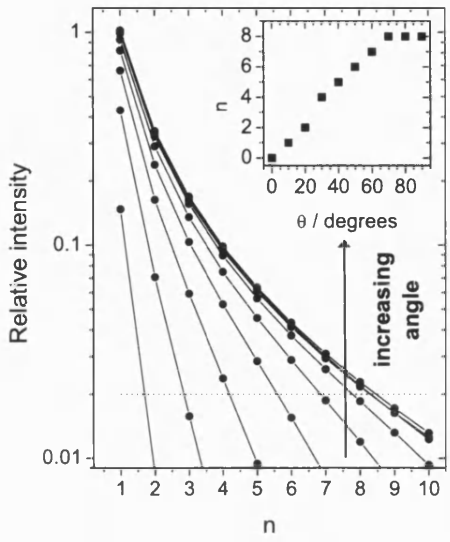

Figure 5.10: Relative intensity (simulated) of n simultaneous spin-flips ($\mathbf{B}_{\text{ext}} = 6$ T). The angle between $\mathbf{B}_{\text{ext}}$ and $\mathbf{B}_{\text{exch}}$ ranges from $\theta = 10°$ to $\theta = 90°$ (relative intensity tends to for 0° (Faraday)). The inset shows number n peaks above a threshold intensity (dashed line in main plot) as a function of θ.

Here V is the volume of the exciton, n'_{Mn} is the density of Mn^{2+} ions, S is the total angular momentum of the ground state of Mn^{2+} and the angle δ is between $\mathbf{B}_{\text{eff}}$ and $\mathbf{B}_{\text{ext}}$ (Fig. 5.9). The precession frequency of the manganese ions ω_L is given by

$$w_L = \frac{g_{\text{Mn}}\mu_B}{\hbar}\mathbf{B}_{\text{eff}} = \frac{g_{\text{Mn}}\mu_B}{\hbar}\sqrt{(\mathbf{B}_{\text{ext}}^2 + \mathbf{B}_{\text{exch}}^2 - 2\mathbf{B}_{\text{ext}}\mathbf{B}_{\text{exch}}\cos\phi)}, \tag{5.34}$$

where ϕ is the angle between $\mathbf{B}_{\text{ext}}$ and $\mathbf{B}_{\text{exch}}$, such that $\theta = 180° - \phi$ (Fig. 5.9).

Using Eq. 5.32, the relative intensities of the Raman peaks ($n = 1 \ldots 10$) have been calculated for $\mathbf{B}_{\text{ext}} = 6$ T, based on the parameters used by *Stühler* [107] et al for similar quantum wells: $\tau = 0.3$ ps, $(a_0)_{x,y} = 30$ Å (exciton center of mass localisation radius), and $\mathbf{B}_{\text{exch}} = 1.2$ T $\rightarrow$ 2 T [113]. The relative intensities for the two extreme values of the exchange field are plotted for $\theta = 90°$ in Fig. 5.9. As expected, an increase in the exchange field leads to an increase in the number of overtones observed. The large intensity difference between $n = 1$ and $n = 2$ predicted by the theory is not observed in the experimental data. The same discrepancy is also found in Ref. [107]. This is most likely due to inhomogeneous

broadening effects.

The behavior of the multiple PMR signal in the Voigt geometry has been well documented, but this is the first investigation into the angle dependence of these signals. In Fig. 5.10, the relative intensities of the Raman peaks have been plotted for θ ranging from $10° \rightarrow 90°$, using the upper value of $\mathbf{B}_{\text{exch}}$ (2 T). In Faraday geometry ($\theta = 0°$), $P_n(\tau) \rightarrow 0$ for all values of n, therefore has not been included in this plot. The dashed line represents a cut-off point under which the Raman signal is not expected to be observed. The number of simultaneous spin-flips above this line as a function of θ is shown in the inset of Fig. 5.10. The number of overtones steadily increases with θ, reaching a constant value ($n = 8$) at 70°. This agrees well with the experimental data (Fig. 5.8).

5.4 Coherent Raman ESR signals in single QWs

This section focuses on the coherent Raman-detected Mn^{2+} PMR signals in single $Cd_{1-x}Mn_xTe/Cd_{1-x-y}Mn_xMg_yTe$ quantum wells.

5.4.1 Coherent Raman in a wide SQW

Mn^{2+} paramagnetic resonance has been detected by CRESR in resonance with a 301 Å wide $Cd_{1-x}Mn_xTe/Cd_{1-x-y}Mn_xMg_yTe$ ($x = 0.0116$ and $y = 0.12$) single quantum well (#505A, appendix C). The absorptive- and dispersive-like components of the coherent Raman spectra are shown in Fig. 5.11 for a low microwave power. Reducing the microwave power has two main effects: the absorption of microwaves is below the saturation limit and microwave resonant heating effects (subsection 3.3.3) are negligible. Consequently, a good fit to the experimental data (Fig. 5.11 (lines)) has been found using standard ESR theory. The absorption component has been simulated using a single Lorentzian, centred at a magnetic field of 1.167 T. The microwave frequency is fixed at 32.94 GHz, leading to a g factor of $g = 2.02$.

The absorption and dispersion spectra in Fig. 5.11 have been redrawn in Fig. 5.12 (a). In each subsequent spectra ((b) to (d)) the microwave power is double that of

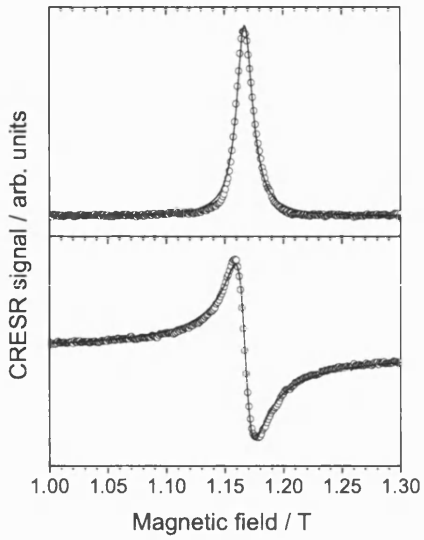

Figure 5.11: Coherent Raman-detected Mn^{2+} PMR signal (points) in a 301 Å wide $Cd_{1-x}Mn_xTe/Cd_{1-x-y}Mn_xMg_yTe$ ($x = 0.0116$ and $y = 0.12$) single quantum well (#505A) at a microwave frequency of 32.9 GHz and a low microwave power: top) absorptive component; bottom) dispersive component. The lines are simulated fits.

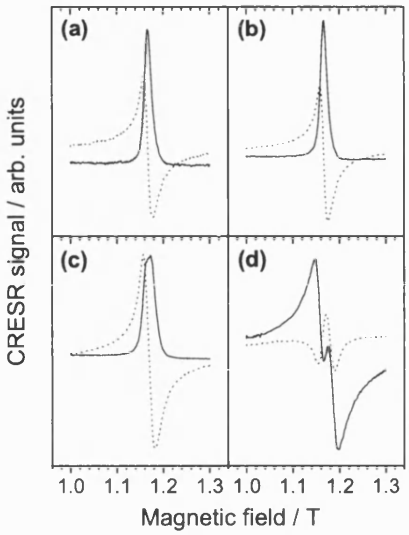

Figure 5.12: Coherent Raman ESR PMR spectra for a 301 Å wide $Cd_{1-x}Mn_xTe/Cd_{1-x-y}Mn_xMg_yTe$ ($x = 0.0116$ and $y = 0.12$) SQW (#505A). For (a) to (d) the microwave power is double that of the previous spectra, i.e. the power in (d) is 8 times that of (a). The microwave frequency is 32.9 GHz

the previous spectra, but the excitation energy remains unchanged (1.6136 eV). Any direct comparisons of the signal intensity of individual components would be meaningless, as a change in microwave power shifts the energy of the excitonic transitions (due to the temperature change), changing the optical resonance conditions. However, the ratio in intensity of the absorption to dispersion components will not be affected by the change in transition energy, but as discussed previously (subsection 2.3.5), microwave saturation of the absorption component at high microwave powers will change the ratio. The intensity ratio is the same in (a) as (b), suggesting that both signals are unsaturated, but in (c) microwave saturation leads to the relative strength of the absorption component decreasing with respect to the dispersion component. In the coherent Raman signal in Fig. 5.12 (d), the highest microwave power, both saturation and resonant heating effects are clearly observed.

A coherent Raman signal originating from the first overtone ($n = 1$) would be centered at half the magnetic field of the original Mn^{2+} PMR spectra. In investigating this magnetic field region no signal could be detected. Any of the

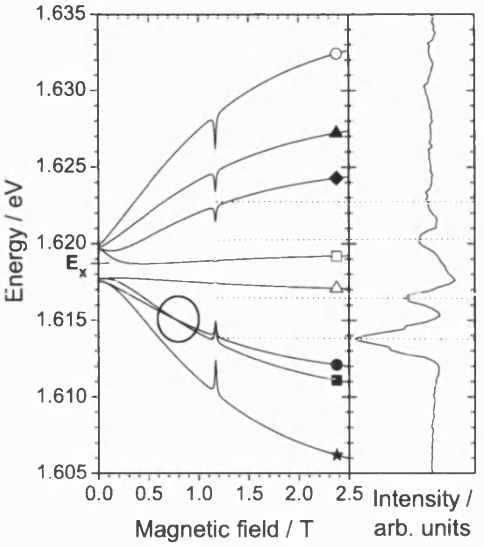

Figure 5.13: Left) calculated energy of the QW ground state (e_1–hh_1,lh_1) exciton levels as a function of magnetic field. Microwave heating causes "dips" at magnetic resonance. The symbols connect these levels to their associated transition probabilities in Fig 5.14. Right) coherent Raman (absorption) signal intensity at 1.165 T & a microwave frequency of 32.9 GHz as a function of excitation energy. QW details are given in the text.

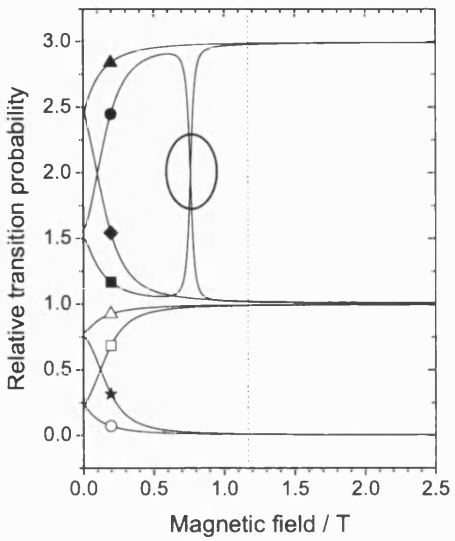

Figure 5.14: The relative transition probabilities (calculated) of the excitonic states in Fig. 5.13 (connected by the corresponding symbol) as a function of magnetic field. The dotted line marks the magnetic field position at which magnetic resonance occurs.

higher order overtones ($n > 1$), that have been observed in SFRS (section 5.2), are forbidden in the CRESR scattering process due to the selection rules of the microwave photon.

5.4.2 Coherent Raman optical resonance profile (wide SQW)

The spectra in Fig. 5.13 (right) are acquired by scanning the laser whilst recording the in-phase channel (corresponding to the absorptive-like signal) of the lock-in detector, at a fixed magnetic field and microwave frequency (chapter 4). The external magnetic field is fixed at 1.165 T, very close to magnetic resonance for the Mn^{2+} PMR signal (1.169 T for a microwave frequency of $\nu = 32.9$ GHz). The excitation energy is in resonance with 301 Å wide $Cd_{1-x}Mn_xTe/Cd_{1-x-y}Mn_xMg_yTe$ ($x = 0.0116$ and $y = 0.12$) single quantum well (#505A, appendix C). The lines

in Fig. 5.13 (left) are the e_1–hh_1,lh_1 exciton states, calculated from the eigenstates of the Hamiltonian given in Eq. 5.21. The energy position of these at magnetic resonance (indicated by the horizontal dashed lines) is consistent with the experimental data. The Raman scattering mechanism is analogous to that of the bulk material (Fig. 3.23). For a quantum well of this width the exciton binding energy is tending towards the bulk value (Fig. B.1); therefore, it is justified to assume that Δ_{eh} is also close to its bulk value. As previously stated, this is not known for CdTe, so it has been assumed to be of the order of ~ 0.1 meV based on work on GaAs [95] and CdSe [114] structures.

Using the calculations described in subsection 5.1.1 the light- and heavy-hole energy splitting, and the central energy at 0 T (marked E_χ in Fig. 5.13) can be determined. For a well width of 93 ML (301 Å), as specified by the growers, this gives $E_\chi = 1.6294$ eV. However, much better agreement with the experimental data is found by using a well width of 94 ML (305 Å), which gives $E_\chi = 1.6187$ eV (as plotted). Both of these quantum well widths lead to $\Delta_{\mathrm{lh-hh}} = 2.1$ meV. The relative transition probabilities of these states can be calculated from the squares of the dipole matrix elements [115], as plotted in Fig. 5.14. At low magnetic fields it is easy see the effects of the intermixing of light- and heavy hole states. At the anticrossing of two excitonic transitions these states will swop character. This is clearly observed for the solid square and circle lines, at the point circled in both Fig. 5.13 (left) and Fig. 5.14. The plot of the relative transition probabilities shows that at magnetic resonance (Fig. 5.14 (dotted line)) the excitonic transitions are tending towards their decoupled states: two forbidden transitions (star, open circle); four light-hole excitonic transitions (open square, open triangle, diamond, closed circle); and two heavy-hole excitonic transitions (closed triangle, closed square).

As stated above, the calculated excitonic transitions shown in Fig. 5.13 (right) are for the e_1–lh_1,hh_1 states assuming a 94ML wide QW, but these are not the only possible transitions in this energy range. The next set of transitions (e_1–lh_3,hh_3) for the 94 ML wide well are centred at an energy of $E_\chi = 1.6305$ eV with $\Delta_{\mathrm{lh-hh}} = 18.5$ meV. This places the lower energy subset of these transitions at 1.6211 eV at 0 T; therefore, they will overlap the e_1–lh_1,hh_1 transitions. Also, it is reasonable to assume that the well width will not be uniform, i.e. a proportion of the sample could be 93 ML wide. The lower energy subset of these transitions ($E_\chi = 1.6294$ eV, $\Delta_{\mathrm{lh-hh}} = 2.1$ meV) will overlap the upper energy group of the

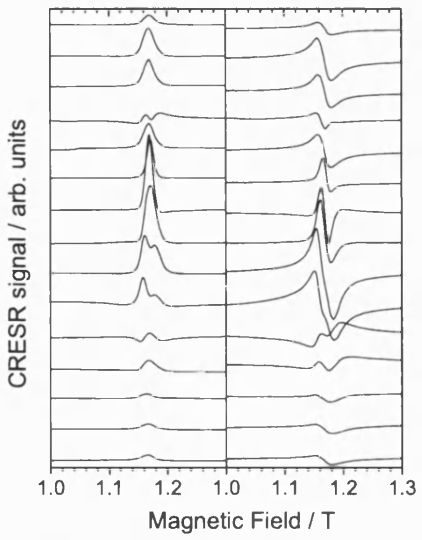

Figure 5.15: Absorption (left) and dispersion (right) coherent Raman components of the Mn^{2+} PMR signal for a 301 Å wide $Cd_{1-x}Mn_xTe/Cd_{1-x-y}Mn_xMg_yTe$ ($x = 0.0116$ and $y = 0.12$) SQW (#505A) for a series of excitation energies. The laser energy ranges from 1.6118 eV (bottom) to 1.6176 eV (top) & the microwave frequency is 32.9 GHz.

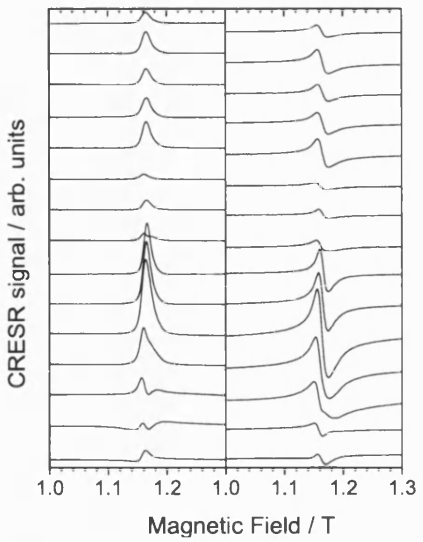

Figure 5.16: Excitation energy dependence of the absorption (left) and dispersion (right) components of the CRESR signal for a 301 Å wide $Cd_{1-x}Mn_xTe/Cd_{1-x-y}Mn_xMg_yTe$ ($x = 0.0116$ and $y = 0.12$) SQW (#505A). The laser energy ranges from 1.6118 eV (bottom) to 1.6176 eV (top) & the microwave frequency is 32.9 GHz. The microwave power is half that of Fig. 5.15.

94 ML wide exciton transitions. In addition, all these transitions are temperature dependent, hence accurately simulating the optical resonance profile of the coherent Raman-detected PMR signal would be extremely difficult.

The effect a change in temperature has on the excitonic energy levels, and hence the optical resonance conditions, can be observed in comparing Fig. 5.15 and Fig. 5.16. Both these figures show the absorptive- and dispersive-like components of the Mn^{2+} PMR signal ($\nu = 32.9$ GHz) for a series of excitation energies ranging from 1.6118 eV (bottom) to 1.6176 eV (top). This is in the energy range of the lowest exciton transitions. The microwave power in Fig. 5.15 is double that of Fig. 5.16, hence the peak in optical resonance in Fig. 5.16 is shifted down in energy compared to that of Fig. 5.15. As with bulk $Cd_{1-x}Mn_xTe$ (subsection 3.3.3), microwave resonant heating leads to deviations from the standard Lorentzian lineshape. This is most easily seen in Fig. 5.15 by the characteristic "dips" in signal intensity at magnetic resonance.

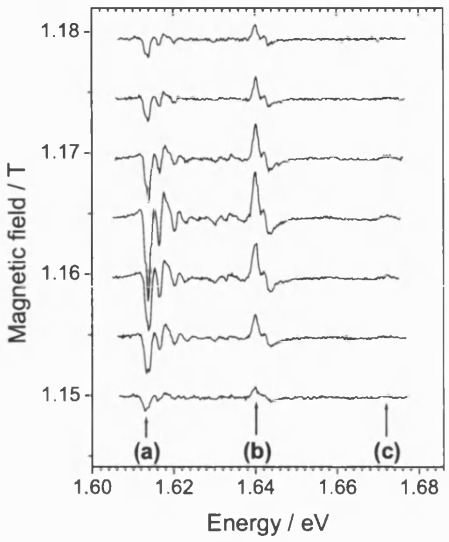

Figure 5.17: Coherent Raman (absorption component) signal intensity as a function of the excitation energy. Spectra have been offset vertically so their zero level corresponds to the magnetic field shown on the y axis. (a), (b) and (c) correspond to the lowest energy transitions of the 301 Å, 78 Å and 45 Å wide SQWs respectively. The microwave frequency is 32.9 GHz.

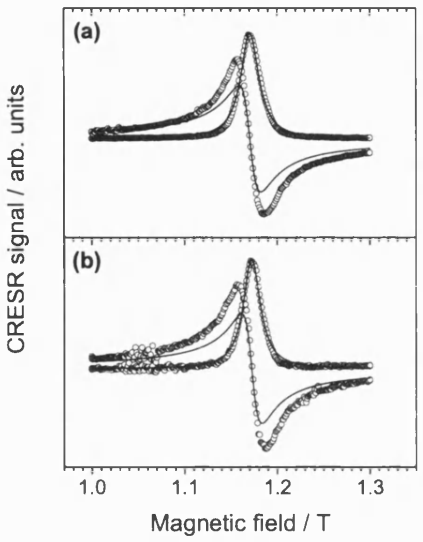

Figure 5.18: Mn^{2+} paramagnetic resonance signal detected by coherent Raman ESR for two single quantum wells ($Cd_{1-x}Mn_xTe/Cd_{1-x-y}Mn_xMg_yTe$, $x = 0.0116$ and $y = 0.12$): a) 78 Å wide; b) 45 Å wide. Points and lines correspond to the experimental and simulated data respectively. The microwave frequency is 32.9 GHz.

5.4.3 Coherent Raman in narrow SQWs

In Fig. 5.17 the signal intensity of the absorption component of the Mn^{2+} PMR signal for the sample #505A (appendix C) has been plotted as a function of excitation energy for a series of fixed magnetic fields, and a fixed microwave frequency of $\nu = 32.9$ GHz. The sample contains four $Cd_{1-x}Mn_xTe/Cd_{1-x-y}Mn_xMg_yTe$ ($x = 0.0116$ and $y = 0.12$) single quantum wells of varying well width. The widest of which (301 Å) has been previously discussed in detail in subsections 5.4.1 and 5.4.2. The peak labeled (a) corresponds to the energy of the lowest excitonic transition in this well. Above this energy and below ~ 1.638 eV the laser is resonant with a series of higher order excitonic states within the same 301 Å well. The energy positions labeled (b) and (c) correspond to the lowest excitonic transitions of the 78 Å and 45 Å wide quantum wells respectively. As the well width decreases there is a reduction in the total number of spins leading to a decrease in the signal intensity. This clearly demonstrates the optical selectivity of the CRESR technique, with the ability to tune into different quantum wells

contained within the same structure.

Typical coherent Raman spectra for the excitation energy in resonance with the 78 Å and 45 Å wide quantum wells are shown in Fig. 5.18 (a) and (b) respectively. In both cases the absorption component has been fitted using a single Lorentzian (line). These are centred at a magnetic field of 1.17 T, for a microwave frequency of 39.2 GHz this leads to a g factor of $g = 2.01$. The signal-to-noise of these signals is still good despite the reduction in well width. The narrowest quantum well (45 Å) has a linewidth (absorption component) of 22.2 mT, and approximately 10^{11} spins within the laser volume. Standard ESR instruments can typically detect 10^{12} spins (300 K), and about 10^{10} spins at low temperatures, for linewidths of 1 mT. Here, there are ten times that number of spins but the linewidth is ten times larger. Hence this is at the limit of the sensitivity of conventional ESR.

5.5 Summary

It has been shown, that the excitonic states of $Cd_{1-x}Mn_xTe/Cd_{1-x-y}Mn_xMg_yTe$ single quantum well can be calculated, in good agreement with experiment, using the theory outlined in subsection 5.1.1. Multiple spin-flip Raman scattering has been observed in resonance with a series of quantum wells with varying well width (section 5.2). The number of spin-flips is shown to decrease as the angle between the applied magnetic field and the quantum well growth axis is reduced, as predicted from theoretical calculations (subsection 5.3.2). In section 5.4 coherent Raman-detected Mn^{2+} PMR signal is shown to be in optical resonance with the excitonic states of these SQWs. The excitation energy can be separately tuned into resonance with three different QWs, of varying well widths (300 Å, 78 Å and 45 Å), within the same structure. The number of spins in the narrowest of these quantum wells is at the detection limit of convention ESR, highlighting the sensitivity of the coherent Raman ESR method.

Chapter 6

Conclusions and future work

For the first part of this final chapter the main conclusions of the three previous experimental chapters (3 – 5) are summarised (section 6.1). This is followed by look at how this work could develop in the future (section 6.2).

6.1 Conclusions

In chapter 3, the first application of coherent Raman ESR to a DMS is reported. Mn^{2+} electron paramagnetic resonance has been detected in CdTe, in optical resonance with free or weakly bound exciton states, via the *sp-d* exchange interaction. This signal has been detected with both a 13.7 GHz and 33.7 GHz microwave source, in a bulk $Cd_{0.995}Mn_{0.005}Te$ sample. The spectra acquired using the 33.7 GHz source contains additional structure due to the hyperfine interaction between the Mn^{2+} $3d^5$ electrons and the Mn^{2+} nucleus, and the cubic crystal field. The hyperfine interaction leads to six equally spaced lines, which are each split into a further five lines by the cubic crystal field. Taking into account all thirty components a good fit to the experimental data is achieved. This signal is centred at a magnetic field of 1.201 T leading to a g factor of $g = 2.01$, consistent with typical SFRS and ESR literature values.

Deviations from the typical Lorentzian lineshape expected for the absorption component, typified by either an enhancement or reduction of signal intensity

at the centre of the signal, is shown to be due to spin resonant heating effects. The Mn^{2+} ions are partially depolarised at magnetic resonance leading to a reduction in the conduction and valence band spin splitting, and hence a change in the optical resonance conditions. The optical site-selective nature of the coherent Raman method is demonstrated by plotting the PMR signal for a series of fixed excitation energies. Comparisons with photoluminescence and photoluminescence excitation spectroscopy data for the same sample show the laser is tuned into resonance with free or weakly bound exciton states. Good agreement between simulation and experiment for the excitation dependent series is found, taking into account the energy difference between the conduction or valence band spin splitting and the spin splitting of the $3d^5$ Mn^{2+} Zeeman multiplet. Signal intensity and lineshape are shown to change with a change in microwave power at a fixed excitation energy. This is due to the associated temperature change that acts to shift the energy position of exciton states, leading to a change in the optical resonance conditions.

In chapter 4, the microwave-modulated magneto-reflectivity signals that can be observed in coherent Raman ESR spectra, have been investigated. Although the exact origin of these signals still remains unclear, it appears likely that they are a form of amplitude modulated magnetic linear or circular dichroism. Both of these theories rely on the assumption of there being non-idealities in the CRESR experimental setup. The MMMR signals have been observed in $Cd_{x-1}Mn_xTe$, GaAs and $Ga_{1-x}Mn_xAs$ samples. The signals in the former semiconductor have been shown to originate from free or weakly bound exciton transitions. In the gallium arsenide based structures, MMMR signals have been attributed to $1s$ and $2s$ excitonic and Landau level structure. Some basic modeling of the Landau level transitions has been possible, but this fails to take into account any excitonic effects. Currently, no coherent Raman signals have been detected in a GaAs based structure.

In chapter 5, the focus is on $Cd_{1-x}Mn_xTe/Cd_{1-x-y}Mn_xMg_yTe$ single quantum wells. Two important sets of results have been presented: angle dependence of multiple PMR lines detected by SFRS; and coherent Raman-detected Mn^{2+} electron paramagnetic resonance.

First, the spin-flip Raman spectroscopy results are considered. In the Voigt configuration nPMR lines ($n > 2$) are observed in $Cd_{1-x}Mn_xTe/Cd_{1-x-y}Mn_xMg_yTe$

($x = 0.0116$ and $y = 0.12$) single quantum wells, for a range of well widths: 300 Å, 78 Å, 45 Å and 19 Å. The creation of a localised heavy-hole exciton leads to the production of an exchange field perpendicular to the external magnetic field. The effective magnetic field is now the vector sum of these two magnetic fields, and is no longer aligned with the external magnetic field, allowing new optical paths to be opened. The magnitude of the exchange field is proportional to light- and heavy-hole energy splitting; an increase in the number n of PMR lines is observed as the well width is decreased.

For the 45 Å wide quantum well the dependence of n on the angle between the external magnetic field and the growth direction (parallel to the exchange field) is investigated. In accord with theoretical predictions a decrease in n is observed as the angle changes from 90° (Voigt configuration) to 0° (Faraday configuration). The excitation source is in resonance with excitonic states, which are in themselves angle dependent. Therefore, the energy of the laser needs to be shifted back to the peak of the resonance for each new angle. This, combined with the fact, there is often more than one resonance process present, means quantitative comparisons between experiment and theory are difficult.

The most important result of chapter 5 is the detection of Mn^{2+} PMR by CRESR in $Cd_{1-x}Mn_xTe/Cd_{1-x-y}Mn_xMg_yTe$ ($x = 0.0116$ and $y = 0.12$) single quantum wells. Coherent Raman spectra have been shown for 301 Å, 78 Å and 45 Å wide quantum wells, using a 32.9 GHz microwave source. The energy of the lowest heavy- and light-hole exciton transitions, and their relative transition probabilities, have been calculated as a function of magnetic field for the widest of these wells. When the energy of these transitions, at the magnetic resonance field, is compared to the optical resonance profile of the coherent Raman absorption component, a correlation is found between the two. Therefore, analogous to bulk $Cd_{1-x}Mn_xTe$, the laser is in optical resonance with the lowest energy exciton states via the *sp-d* exchange interaction. If the laser is tuned to higher energies, the signal is observed to be resonant with higher order exciton states. The three quantum wells are contained within the same sample; therefore, tuning the laser to even higher energies put it in resonance with first the 78 Å wide and then the 45 Å wide quantum well. The optical selectivity of the coherent Raman ESR technique is clearly apparent in the spectra shown.

At very low microwave powers spin resonant heating and microwave saturation

effects are found to be negligible, and the coherent Raman spectra can be simulated using standard ESR theory. For the widest well, a single Lorentzian centred at a magnetic field of 1.167 T is used, to give $g = 2.02$. As the microwave power is increased, and hence the temperature, the trademark changes to lineshape and signal intensity due to these effects are once again observed. The number of spins, for this linewidth, in the narrowest quantum well (45 Å) is right at the limit required for conventional ESR. However, the signal-to-noise level of the CRESR signal is still very good, illustrating the superior sensitivity of the method. The obvious next step would be to reduce the number of spins even further to really test the sensitivity.

In summary, coherent Raman electron spin resonance has successfully been applied to the dilute magnetic semiconductor $Cd_{1-x}Mn_xTe$, both for bulk and quantum well structures. This is the first application of this technique to a DMS. Throughout the thesis, the optical selectivity, high energy resolution and sensitivity that is indicative of the CRESR method is clearly demonstrated.

6.2 Future work

For the first application of this technique to DMS it is logical to use such an archetypal material as $Cd_{1-x}Mn_xTe$. However, the experience gained from this work can now be applied to new materials, structures and problems. When considering possible candidates for experiments it is important they meet three basic requirements:

1. the sample must be nonconductive - so a microwave cavity resonance can be produced;
2. a resonant excitation source must be available;
3. the Raman process must allow the microwave photons to interact with a spin system.

The second of these requirements unfortunately currently rules out any work on GaN or ZnTe based samples, where a tunable excitation source is required in

the ultra violet and the green region of the spectrum respectively. The natural progression after the detection of CRESR signals in quantum wells is to use the method to investigate quantum dots structures, where the sensitivity of standard ESR is an issue. Interest in semimagnetic quantum dot is fuelled by the prospect of creating quantum bits for quantum computers (section 1.3). CRESR could potentially allow one to optically select different sized quantum dots by varying the excitation energy. However, again there could be potential problems. This is highlighted by the work of *Sirenko* et al [116] on spin-flip Raman spectroscopy of CdS quantum dots. Here, it was discovered that the Raman process is mediated by acoustic phonons; hence, the third requirement is potentially not satisfied.

As outlined in section 1.3, there is presently a great deal of interest in III-V DMS, such as GaMnAs, with the view to producing spintronics devices which can be easily incorporated into current technologies. Still under debate is the charge state of Mn ions in GaAs. ESR and SFRS spectra in different GaMnAs samples show signals relating to different g factors [92]. CRESR would appear to be the ideal method to study this problem; however, before this is possible some technical constraints regarding the conductivity of GaAs need to be overcome (chapter 4). A good possible direction in which to take this research is the investigation of new paramagnetic ion impurities in semiconductors, such as the rare earth element gadolinium in GaAs [117]. Presently, the magnetic ion concentrations achievable in this material are below that required for detection by standard ESR.

Appendix A

$\vec{\mathbf{k}} \cdot \vec{\mathbf{p}}$ perturbation theory

$\vec{\mathbf{k}} \cdot \vec{\mathbf{p}}$ perturbation theory [111, 118] is a band structure theory, from which analytical expressions for the effective masses and g values of semiconductors can be derived. The method begins by considering the one-electron Schrödinger equation,

$$\mathbf{H}_e \Psi_{n\mathbf{k}}(\mathbf{r}) = \left(\frac{p^2}{2m} + V(\mathbf{r}) \right) \Psi_{n\mathbf{k}}(\mathbf{r}) = E_{n\mathbf{k}} \Psi_{n\mathbf{k}}(\mathbf{r}), \tag{A.1}$$

where $\mathbf{H}_e$ is the one-electron Hamiltonian, $\mathbf{p}$ is the momentum, m is the free electron mass and $V(\mathbf{r})$ is the one-electron potential. $\Psi_{n\mathbf{k}}(\mathbf{r})$ and $E_{n\mathbf{k}}$ are the wavefunction and energy of an electron, respectively, for a given wavevector ($\mathbf{k}$) and the band index (n). The Bloch solution to Eq. A.1 takes the form of

$$\Psi_{n\mathbf{k}}(\mathbf{r}) = e^{i\mathbf{k}\cdot\mathbf{r}} u_{n\mathbf{k}}(\mathbf{r}). \tag{A.2}$$

Here $\mathbf{k}$ lies within the first Brillouin zone and $u_{n\mathbf{k}}(\mathbf{r})$ has the periodicity of the lattice. Remembering that $\mathbf{p} = -i\hbar\nabla$, substituting Eq. A.2 into Eq. A.1 yields

$$\left(\frac{p^2}{2m} + \frac{\hbar \mathbf{k} \cdot \mathbf{p}}{m} + \frac{\hbar^2 k^2}{2m} + V(\mathbf{r}) \right) u_{n\mathbf{k}}(\mathbf{r}) = E_{n\mathbf{k}} u_{n\mathbf{k}}(\mathbf{r}). \tag{A.3}$$

When $\mathbf{k} = \mathbf{k}_0 = (0, 0, 0)$, Eq. A.3 reduces to

$$\mathbf{H}_{\mathbf{k}_0} u_{n0}(\mathbf{r}) = \left(\frac{p^2}{2m} + V(\mathbf{r}) \right) u_{n0}(\mathbf{r}) = E_{n0} u_{n0}(\mathbf{r}). \tag{A.4}$$

This can be substituted back into Eq. A.3 to get

$$\left(\mathbf{H}_{\mathbf{k}_0} + \frac{\hbar\mathbf{k}\cdot\mathbf{p}}{m} + \frac{\hbar^2k^2}{2m}\right) u_{n\mathbf{k}} = E_{n\mathbf{k}} u_{n\mathbf{k}}. \tag{A.5}$$

Equation A.5 can be treated using standard perturbation theory [119, 120], where $\mathbf{H}_{\mathbf{k}_0}$ is the unperturbed Hamiltonian, and $\mathbf{H}_1 = \hbar\mathbf{k}\cdot\mathbf{p}/m$ and $\mathbf{H}_2 = \hbar^2k^2/2m$ are the first and second order perturbation terms respectively. For a nondegenerate system, for example the conduction band minimum in a direct bandgap semiconductor, the wave functions $u_{n\mathbf{k}}$ and the energies $E_{n\mathbf{k}}$, to the first order, are given by

$$u_{n\mathbf{k}} = u_{n0} + \sum_{n\neq n'} \frac{\langle u_{n'0}|\mathbf{k}\cdot\mathbf{p}|u_{n0}\rangle}{E_{n0} - E_{n'0}} u_{n'0}, \tag{A.6}$$

$$E_{n\mathbf{k}} = E_{n0} + \frac{\hbar}{m}\langle u_{n0}|\mathbf{k}\cdot\mathbf{p}|u_{n0}\rangle. \tag{A.7}$$

The first order correction to the wavefunctions is inversely proportional to the energy separation $E_{n0} - E_{n'0}$; the more the remote the band the less influence it will have.

To the second order, $E_{n\mathbf{k}}$ is

$$E_{n\mathbf{k}} = E_{n0} + \frac{\hbar^2k^2}{2m} + \frac{\hbar^2}{m^2}\sum_{n\neq n'} \frac{|\langle u_{n0}|\mathbf{k}\cdot\mathbf{p}|u_{n'0}\rangle|^2}{E_{n0} - E_{n'0}}. \tag{A.8}$$

This is equivalent to

$$E_{n\mathbf{k}} = E_{n0} + \frac{\hbar^2k^2}{2m^*}, \tag{A.9}$$

where the effective mass m^*, is defined as

$$\frac{1}{m^*} = \frac{1}{m} + \frac{2}{m^2k^2}\sum_{n\neq n'} \frac{|\langle u_{n0}|\mathbf{k}\cdot\mathbf{p}|u_{n'0}\rangle|^2}{E_{n0} - E_{n'0}}. \tag{A.10}$$

From Eq. A.10, it is clear that the mass of an electron in a semiconductor will deviate from the free electron mass due to coupling between the energy bands via the $\mathbf{k}\cdot\mathbf{p}$ term. If $E_{n0} > E_{n'0}$, the effective mass will be less than the free electron mass, on the other hand if $E_{n0} < E_{n'0}$, then either the effective mass will be greater than the free electron mass or the effective mass becomes negative. In

cubic semiconductors with a direct-bandgap, Eq. A.10 can be approximated by

$$\frac{m}{m^*} = 1 + \frac{2P^2}{mE_g} = 1 + \frac{E_p}{E_g}, \tag{A.11}$$

where E_g is the energy gap of the semiconductor and P is equal to

$$iP = \langle X|p_x|\sigma\rangle = \langle Y|p_y|\sigma\rangle = \langle Z|p_z|\sigma\rangle. \tag{A.12}$$

Here σ is the wavefunction corresponding to the bottom of the conduction band, and X, Y and Z are the wavefunctions at the top of the valence band. Typically, for most semiconductors, the band parameter is $E_p \approx 20$ eV.

For CdTe the conduction band effective mass is $m_e/m_0 = 0.096$ [8]. Assuming 1.606 eV [5, 6] and $E_p \approx 21$ eV [9], Eq. A.11 gives $m_e/m_0 = 0.071$. The theoretical value of the electron effective mass can be improved by taking into account the more remote conduction bands Γ_7^C and Γ_8^C to give

$$m^* = m_0 \left[1 + \frac{E_p}{3}\left(\frac{2}{E_g} + \frac{1}{E_g + \Delta_0}\right) - \frac{E_p'}{3}\left(\frac{2}{E(\Gamma_8^C) - E_g} + \frac{1}{E(\Gamma_7^C) - E_g}\right) + C\right]. \tag{A.13}$$

This is known as either five-level or fourteen-band $\mathbf{k}\cdot\mathbf{p}$ perturbation theory and leads to $m_e/m_0 = 0.110$ when the following parameters are used [9, 48, 49]: $E_p' = 5.1$ eV, $\Delta_0 = 0.93$ eV, $E(\Gamma_7^C) = 5.6$ eV, $E(\Gamma_8^C) = 5.3$ eV, $C = -2$.

The relative electric dipole transition probabilities of the light- and heavy hole states can be calculated as follows. The light-hole ($m_J = \pm 1/2$) and heavy-hole ($m_J = \pm 3/2$) valence band states can be written as follows:

$$\Phi_{3/2,3/2} = \frac{-1}{\sqrt{2}}(|X\rangle + i|Y\rangle)\uparrow, \tag{A.14}$$

$$\Phi_{3/2,-3/2} = \frac{1}{\sqrt{2}}(|X\rangle - i|Y\rangle)\downarrow, \tag{A.15}$$

$$\Phi_{3/2,1/2} = \frac{-1}{\sqrt{6}}[(|X\rangle + i|Y\rangle)\downarrow -2|Z\rangle\uparrow], \tag{A.16}$$

$$\Phi_{3/2,-1/2} = \frac{1}{\sqrt{6}}[(|X\rangle - i|Y\rangle)\downarrow +2|Z\rangle\downarrow]. \tag{A.17}$$

The nonzero matrix elements are of the form $\langle X|p_x|\sigma\rangle = \langle Y|p_y|\sigma\rangle = \langle Z|p_z|\sigma\rangle$,

therefore

$$\langle \pm 3/2|p_x| \pm \sigma\rangle = \langle \pm 3/2|p_y| \pm \sigma\rangle = \frac{1}{\sqrt{2}}\langle x|p_x|\sigma\rangle, \tag{A.18}$$

$$\langle \pm 1/2|p_x| \mp \sigma\rangle = \langle \pm 1/2|p_y| \mp \sigma\rangle = \frac{1}{\sqrt{6}}\langle x|p_x|\sigma\rangle, \tag{A.19}$$

$$\langle \pm 3/2|p_z| \pm \sigma\rangle = \frac{2}{\sqrt{6}}\langle x|p_x|\sigma\rangle, \tag{A.20}$$

where $|\sigma\rangle$ is the twofold degenerate ($m_S = \pm 1/2$) s-like conduction bandedge state. The probability of a transition between the valence and conduction bands is proportional to the square of the matrix element. Hence, light polarised in the x-y plane couples three times more strongly to the heavy-hole states compared to the light hole states.

A similar perturbation procedure, incorporating spin-orbit interactions, can be carried out to give an analytical expression for the effective g factor in semiconductors g [102, 121]. For conduction band electrons this is found to be

$$\frac{g}{g_0} = 1 + \frac{2}{im}\sum_{n\neq n'} \frac{\langle u_{n0}|p_x|u_{n'0}\rangle\langle u_{n'0}|p_y|u_{n0}\rangle - \langle u_{n0}|p_y|u_{n'0}\rangle\langle u_{n'0}|p_x|u_{n0}\rangle}{E_{n0} - E_{n'0}}, \tag{A.21}$$

where g_0 is the Landé g factor and the magnetic field is along the z axis. In cubic semiconductors g is isotropic, and to the first approximation is equal to

$$\frac{g}{g_0} = 1 - \frac{E_p}{3}\left(\frac{1}{E_g} - \frac{1}{E_g + \Delta_0}\right), \tag{A.22}$$

where Δ_0 is the valence band spin-orbit splitting. Analogous to the effective mass, a closer fit to the experimental values of g is obtained by five-level $\mathbf{k}\cdot\mathbf{p}$ perturbation theory[9, 48]:

$$\begin{aligned} g &= g_0\left[1 - \frac{E_p}{3}\left(\frac{1}{E_g} - \frac{1}{E_g + \Delta_0}\right) - \frac{E'_p}{3}\left(\frac{1}{E(\Gamma_7^C) - E_g} - \frac{1}{E(\Gamma_8^C) - E_g}\right) + C'\right. \\ &\quad \left. + \frac{2}{9}\frac{\sqrt{E_p E'_p}\Delta^-}{E(\Gamma_7^C) - E_g}\left(\frac{1}{E_g} + \frac{2}{E_g} + \Delta_0\right)\right]. \end{aligned}$$

A full account of the notation can be found in Ref. [48].

Appendix B

Exciton binding energy in a finite QW

Described here is the simple analytical model of *Mathieu* at al [122], for calculating the exciton binding energy in semiconductor quantum well structures.

Solving the hydrogenic Schrödinger equation gives a series of n quantised energy levels, of energy [123]

$$E_n = E_g - \frac{E_0}{[n + \frac{\alpha-3}{2}]^2}, \tag{B.1}$$

where E_g is the energy gap, E_0 is the effective Rydberg constant and α represents the spatial dimension. For the $1s$ exciton, the exciton binding energy E_b is

$$E_b = \left[\frac{2}{\alpha - 1}\right]^2 E_0 : \tag{B.2}$$

equal to E_0, $4E_0$ and ∞ in a 3, 2 and 1 dimensional system respectively. In a finite quantum well, α is used as a measure of the anisotropy of the electron-hole interaction. A decreasing quantum well width compresses the electron and hole envelope functions, leading to an anisotropic electron-hole Coulomb interaction and a decreasing α (from 3 to 2). As the well width continues to narrow, a point will be reached where the envelope functions will begin to spread into the barrier. The narrower the well, the greater the envelope functions will penetrate the barrier, consequently α starts to increase back towards 3.

The value of α is given by

$$\alpha = 3 - e^{-\frac{L^*}{2a_0^*}} = 3 - e^{-\beta}, \tag{B.3}$$

where a_0^* is the effective Bohr radius and L^* is the spatial extent of the particles motion along the x axis, given by

$$L^* = \frac{2}{\kappa_b} + L. \tag{B.4}$$

Here L is the quantum well width and κ_b is the wavevector of the barrier both sides (Eq. 5.8). In a square potential well the wavevector of the exciton in the barrier is given by

$$\frac{1}{\kappa_b} = \frac{1}{\kappa_{be}} + \frac{1}{\kappa_{bh}}, \tag{B.5}$$

where κ_{be} and κ_{bh} are the barrier wavevectors of the electron and hole respectively. The effective Bohr radius is

$$a_0^* = \frac{\epsilon}{\epsilon_0}\frac{m_0}{\mu^*}a_H, \tag{B.6}$$

where m_0 is the electron rest mass, μ^* is the effective mass of the exciton, a_H is the Bohr radius for hydrogen and ϵ/ϵ_0 is the ratio of the electric permittivity in the material and in free space, known as the dielectric constant.

In this method, the off diagonal terms of the Luttinger Hamiltonian are neglected. Therefore, in the 3D case heavy- and light-hole effective masses are both assumed to be $1/m_h = 1/\gamma_1$, and in the 2D case the heavy- and light-hole effective masses are given by $1/m_{hh} = 1/\gamma_1 + \gamma_2$ and $1/m_{lh} = 1/\gamma_1 - \gamma_2$. The heavy- and light-hole effective exciton masses are calculated by interpolating between these two cases

$$\frac{1}{\mu_{hh}^*} = \frac{1}{m_e^*} + \gamma_1^* + (3-\alpha)\gamma_2^*, \tag{B.7}$$

$$\frac{1}{\mu_{lh}^*} = \frac{1}{m_e^*} + \gamma_1^* - (3-\alpha)\gamma_2^*, \tag{B.8}$$

where γ_1^* and γ_2^* are the effective valence band (Luttinger) parameters and m_e^* is the effective mass of the electron. These are defined by

$$m_e^* = \beta_e m_{ew}^* + (1-\beta_e)m_{eb}^*, \tag{B.9}$$

$$\gamma_1^* = \beta_h \gamma_{1w} + (1-\beta_h)\gamma_{1b}, \tag{B.10}$$

$$\gamma_2^* = \beta_h \gamma_{2w} + (1-\beta_h)\gamma_{2b}, \tag{B.11}$$

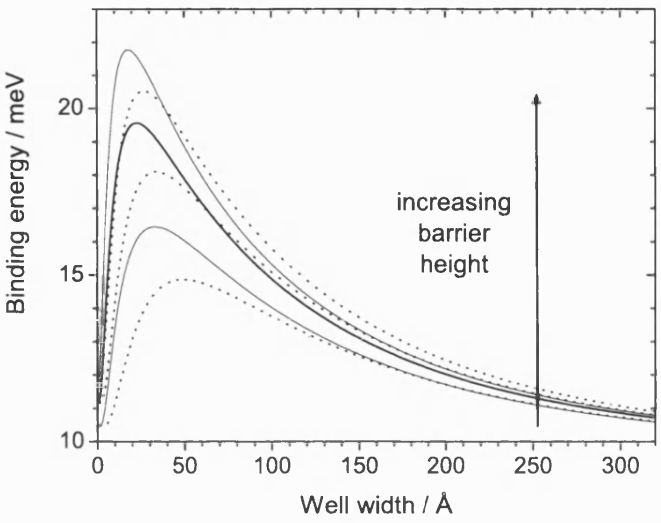

Figure B.1: Heavy-hole (lines) and light-hole (dots) exciton binding energies as a function of well width, for three different ($y = 0.1, 0.2, 0.3$) $Cd_{1-x}Mn_xTe/Cd_{1-x-y}Mn_xMg_yTe$ quantum wells.

where m^*_{ew} (γ_{1w} and γ_{2w}) and m^*_{eb} (γ_{1b} and γ_{2b}) are the electron effective masses (valence band parameters) in the well and barrier respectively, and

$$\beta_e = \frac{L}{(\frac{2}{\kappa_{be}} + L)}, \tag{B.12}$$

$$\beta_h = \frac{L}{(\frac{2}{\kappa_{bh}} + L)}. \tag{B.13}$$

The exciton binding energy in a finite quantum well is found by substituting in Eq. B.3 and Eq. B.4 into Eq. B.2, to give

$$E_b = \frac{E_0^*}{[1 - \frac{1}{2}e^{(-2/\kappa_b + L)/2a_0^*}]^2}, \tag{B.14}$$

where

$$E_0^* = \left(\frac{\epsilon_0}{\epsilon}\right)^2 \frac{\mu^*}{m_0} R_H. \tag{B.15}$$

Here R_H is the Rydberg constant for hydrogen. In Fig. B.1 the binding energies of both heavy- and light-hole excitons have been plotted for a series of $Cd_{1-x}Mn_xTe/Cd_{1-x-y}Mn_xMg_yTe$ quantum wells with varying barrier heights. The following parameters have been used [5, 8]: $m^*_{ew}/m_0 = 0.096$, $m^*_{eb}/m_0 = 0.096(1 - x_{\rm mg}) + 0.209x_{\rm mg}$, $\gamma_{1w} = \gamma_{1b} = 4.78$, $\gamma_{2w} = \gamma_{2b} = 1.77$, and $\epsilon/\epsilon_0 = 9.6$. Here the bulk CdTe values (section 1.1) of γ_1 and γ_2 are assumed for both the well and barrier materials.

Appendix C

Sample details

Sample	Well	Well width	Barrier	Buffer	Substrate
#505A	CdMnTe $x_{Mn} = 0.0116$	93 ML 24 ML 14 ML 6 ML	CdMgMnTe $x_{Mn} = 0.0116$ $y_{Mg} = 0.12$ (300 Å)	CdMgTe 1.1–1.3 μm	(100) GaAs thin layer of ZnTe CdTe (300 Å)
#505B	CdMnTe $x_{Mn} = 0.023$	93 ML 24 ML 14 ML 6 ML	CdMgMnTe $x_{Mn} = 0.023$ $y_{Mg} = 0.12$ (300 Å)	CdMgMnTe 1.1–1.3 μm	(100) GaAs thin layer of ZnTe CdTe (300 Å)
#105A	CdMnTe $x_{Mn} = 0.03$	93 ML 24 ML 14 ML 6 ML	CdMgMnTe $x_{Mn} = 0.03$ $y_{Mg} = 0.25$ (300 Å)	CdMgMnTe 1.1–1.3 μm	(100) GaAs thin layer of ZnTe CdTe (300 Å)
#305A	CdTe	93 ML 18 ML 10 ML 6 ML	CdMgTe $y_{Mg} = 0.2$ (300 Å)	CdMgTe 1 μm	(100) GaAs CdTe (4.5 μm)

Table C.1: Samples grown by MBE at the Institute of Physics, Polish Academy of Sciences, Warsaw, Poland, by T. Wojtowicz and G. Karczewski. 1 ML = 3.24 Å.

Sample	Structure	Substrate
#292	CdTe (2 μm)	InSb

Table C.2: Sample grown by MBE, at the Department of Engineering Design and Manufacture, University of Hull, UK, by D. E. Ashenford and B. Lunn.

Sample	Structure	Substrate
#12697	GaAs:Mn/MnAs	GaAs (001)

Table C.3: Sample grown by MOVPE, Department of Physics and Materials Sciences Center, Philipps University, Marburg, Germany, by W. Stolz.

References

[1] Kenneth Zanio. *Cadmium telluride*, volume 13 of *Semiconductors and semimetals*. Academic Press, 1978.

[2] Rudolf Frerichs. The photo-conductivity of "incomplete phosphors". *Phys. Rev.*, **72**(7):594–601, October 1947.

[3] O. Madelung, M. Schulz, and H. Weiss, editors. *Landort-Börnstein: Numerical data and functional relationships in science and technology.*, volume 17. Springer-Verlag, 1982.

[4] James R. Chelikowsky and Marvin L. Cohen. Nonlocal pseudopotential calculations for the electronic structure of eleven diamond and zinc-blende semiconductors. *Phys. Rev. B*, **14**(2):556–582, July 1976.

[5] Q. X. Zhao, M. Oestreich, and N. Magnea. Electron and hole g-factors in CdTe/CdMgTe quantum wells. *Appl. Phys. Lett*, **69**(24):3704–3706, December 1996.

[6] D.G. Thomas. Excitons and band splitting produced by uniaxial stress in CdTe. *J. Appl. Phys.*, **32**(10), October 1961.

[7] T Itoh, K Shinone, N Katagiri, M Furumiya, and T Tezuka. Stress-induced mixing of exciton states in thin films of CdTe and CdMnTe on GaAs. *J. Crystal Growth*, **117**:835–839, February 1992.

[8] R. Romestain and C. Weisbuch. Optical detection of cyclotron resonance in semiconductors. *Phys. Rev. Lett.*, **45**(25):2067–2070, December 1980.

[9] A. A. Sirenko, T. Ruf, M. Cardona, D. R. Yakovlev, W. Ossau, A. Waag, and G. Landwehr. Electron and hole g factors measured by spin-flip Raman scattering in CdTe/$Cd_{1-x}Mg_xTe$ single quantum wells. *Phys. Rev. B*, **56**(4):2114–2119, July 1997.

[10] S. Tsoi, I. Miotkowski, S. Rodriguez, A.K. Ramdas, H. Alawadhi, and T.M. Pekarek. Resonant electron spin-flip Raman scattering in CdTe and the diluted magnetic semiconductor $Cd_{1-x}V_xTe$. *Phys. Rev. B*, **69**(035209), 2004.

[11] M. V. Alekseenko and A. I. Veinger. Electron spin resonance of shallow donors in CdTe. *Sov. Phys. Semicond.*, **8**(1):143, January 1974.

[12] J.K. Furdyna. Diluted magnetic semiconductors. *J. Appl. Phys.*, **64**(4), August 1988.

[13] M.J. Seong, H. Alawadhi, I. Miotkowski, A.K. Ramdas, and S. Miotkowska. Raman electron paramagnetic resonance in $Zn_{1-x}Co_xTe$ and $Cd_{1-x}Co_xTe$. *Phys. Rev. B*, **63**(125208), March 2001.

[14] D.R. Yoder-Short, U. Debska, and J.K. Furdyna. Lattice parameters of $Zn_{1-x}Mn_xSe$ and tetrahedral bond lengths in $A_{1-x}Mn_xB$ alloys. *J. Appl. Phys.*, **48**(11), December 1985.

[15] N. Bottka, J. Stankiewicz, and W. Giriat. Electroreflectance studies in $Cd_{1-x}Mn_xTe$ solid solutions. *J. Appl. Phys.*, **52**(6), June 1981.

[16] S. M. Durbin, J. Han, Sungki O, M. Kobayashi, D. R. Menke, R. L. Gunshor, Q. Fu, N. Pelekanos, A. V. Nurmikko D. Li, J. Gonsalves, and N. Otsuka. Zinc-blende MnTe: Epilayers and quantum well structures. *Appl. Phys. Lett.*, **55**(20), November 1989.

[17] Y.R. Lee and A.K. Ramdas. A peizomodulation study of the absorption edge and Mn^{++} internal transition in $Cd_{1-x}Mn_xTe$, a prototype of diluted magnetic semiconductors. *Solid State Commun.*, **51**(11), 1984.

[18] J.K. Furdyna and N. Samarth. Magnetic properties of diluted magnetic semiconductors: A review (invited). *J. Appl. Phys.*, **61**(8), April 1987.

[19] R. R. Gałazka, Shoichi Nagata, and P. H. Keesom. Paramagnetic—spin-glass—antiferromagnetic phase transitions in $Cd_{1-x}Mn_xTe$ from specific heat and magnetic susceptibility measurements. *Phys. Rev. B*, **22**(7):3344–3355, October 1980.

[20] Y. Shapira, S. Foner, D. H. Ridgley, K. Dwight, and A. Wold. Technical saturation and magnetization steps in diluted magnetic semiconductors: Predictions and observations. *Phys. Rev. B*, 30(7):4021–4023, October 1984.

[21] R. L. Aggarwal, S. N. Jasperson, P. Becla, and R. R. Galazka. Optical determination of the antiferromagnetic exchange constant between nearest-neighbor Mn^{2+} ions in $Cd_{0.95}Mn_{0.05}Te$. *Phys. Rev. B*, **32**(8):5132–5137, October 1985.

[22] Y. Shapira, S. Foner, P. Becla, D. N. Domingues, M. J. Naughton, and J. S. Brooks. Nearest-neighbor exchange constant and Mn distribution in $Zn_{1-x}Mn_xTe$ from high-field magnetization step and low-field susceptibility. *Phys. Rev. B*, **33**(1):356–365, January 1986.

[23] B.E. Larson, K.C. Has, and R.L. Aggarwal. Effects of internal exchange fields on magnetisation steps in diluted magnetic semiconductors. *Phys. Rev. B*, **33**(3), February 1986.

[24] J.A. Gaj, J. Ginter, and R. R. Gałazka. Exchange interaction of manganese $3d^5$ states with band electrons in $Cd_{1-x}Mn_xTe$. *Phys. Stat. Sol. (b)*, **89**:655, 1978.

[25] J.A. Gaj, R. Planel, and G. Fishman. Relation of magneto-optical properties of free excitons to spin allignment of Mn^{2+} ions in $Cd_{1-x}Mn_xTe$. *Solid State Commun.*, **29**:435–438, 1979.

[26] A.K. Bhattacharjee, G. Fishman, and B. Coqblin. Virtual bound state model for the exchange interaction in semimagnetic semiconductors. *Physica*, **117B** & **118B**:449–451, 1983.

[27] SSP Parkin, KP Roche, MG Samant, PM Rice, RB Beyers, RE Scheuerlein, EJ OSullivan, SL Brown, J. Bucchigano, DW Abraham, et al. Exchange-biased magnetic tunnel junctions and application to nonvolatile magnetic random access memory (invited). *J. Appl. Phys.*, **85**:5828, 1999.

[28] S. Datta and B. Das. Electronic analog of the electric-optic modulator. *Appl. Phys. Lett.*, **56**(7), February 1990.

[29] R. Fiederling, M. Keim, G. Reuscher, G. Schmidt W. Ossau, A. Waag, and L.W. Molenkamp. Injection and detection of a spin-polarised current in a light-emitting diode. *Nature (London)*, **402**:787–790, December 1999.

[30] D. Ferrand, A. Wasiela, S. Tararenko, J. Cibert, G.Richter, P. Grabs, G. Schmidt, L.W. Molenkamp, and T. Dietl. Applications of II–VI diluted magnetic semiconductors for magneto-electronics. *Sol. St. Commun.*, **119**:237–244, 2001.

[31] Daniel Loss and David P. DiVincenzo. Quantum computation with quantum dots. *Phys. Rev. A*, **57**(1):120–126, January 1998.

[32] I. Žutić, J. Fabian, and S. Das Sarma. Spintronics: Fundamentals and applications. *Rev. Mod. Phys.*, **76**(2), April 2004.

[33] SA Wolf, DD Awschalom, RA Buhrman, JM Daughton, S. von Molnar, ML Roukes, AY Chtchelkanova, and DM Treger. Spintronics: A spin-based electronics vision for the future. *Science*, **294**(5546):1488 – 1495, 2001.

[34] M. N. Baibich, J. M. Broto, A. Fert, F. Nguyen Van Dau, F. Petroff, P. Eitenne, G. Creuzet, A. Friederich, and J. Chazelas. Giant magnetoresistance of (001)Fe/(001)Cr magnetic superlattices. *Phys. Rev. Lett.*, **61**(21):2472–2475, November 1988.

[35] GA Prinz. Magnetoelectronics. *Science*, **282**(5394):1660–1663, 1998.

[36] M. Oestreich, J. Hbner, D. Hgele, P. J. Klar, W. Heimbrodt, W. W. Rhle, D. E. Ashenford, , and B. Lunn. Spin injection into semiconductors. *Appl. Phys. Lett.*, **74**(9), March 1999.

[37] P. Van Dorpe, Z. Liu, W. Van Roy, V.F. Motsnyic, M. Sawicki, G. Borghs, and J. De Boeck. Very high spin polarization in GaAs by injection from a (Ga,Mn)As zener diode. *Appl. Phys. Lett.*, **84**(18), May 2004.

[38] C.V. Raman and K.S. Krishnan. A new type of secondary radiation. *Nature*, 1928.

[39] D.J. Gardiner and P.R. Graves (Eds.). *Practical Raman spectroscopy.* Springer-Verlag, 1989.

[40] S. Perkowitz. *Optical charecterisation of semiconductors: Infrared, Raman, and photoluminescence spectroscopy.* Academic press, 1993.

[41] D. Wolverson, P.J. Boyce, C.M. Townsley, B. Schlichtherle, and J.J. Davies. Spin-flip Raman scatering studies of doped epitaxial zinc selenide. *J. Crystal Growth*, **159**:229–237, 1996.

[42] J.J. Davies, D. Wolverson, O.Z. Karimov, and I.J. Griffin. Spin-flip Raman scattering studies of II-VI heterostructures. *J. Crystal Growth*, **214/215**:616–624, 2000.

[43] Y. Yafet. Raman scattering by carriers in Landau levals. *Phys. Rev.*, **152**(2), December 1966.

[44] P.A. Wolff. Thomson and Raman scattering by mobile electrons in crystals. *Phys. Rev. Lett.*, **16**(6), February 1966.

[45] R.E. Slusher, C.K.N. Patel, and P.A. Fleury. Inelastic light scattering from Landau-leval electrons in semiconductors. *Phys. Rev. Lett.*, **18**(3), January 1967.

[46] J. M. Francou, K. Saminadayar, and J. L. Pautrat. Shallow donors in CdTe. *Phys. Rev. B*, **41**(17):12035–12046, June 1990.

[47] A. A. Kiselev, E. L. Ivchenko, A. A. Sirenko, T. Ruf, M. Cardona, D.R. Yakovlev, W. Ossau, A. Waag, and G. Landwehr. Electron and hole g factor anisotropy in CdTe/CdMgTe quantum wells. *J. Crystal Growth*, **184/185**:831–834, 1998.

[48] Claudine Hermann and Claude Weisbuch. $\vec{\mathbf{k}} \cdot \vec{\mathbf{p}}$ perturbation theory in III-V compounds and alloys: a reexamination. *Phys. Rev. B*, **15**(2):823–833, January 1977.

[49] M. Willatzen, M. Cardona, and N. E. Christensen. Spin-orbit coupling parameters and electron g factor of II-VI zinc-blende materials. *Phys. Rev. B*, **51**(24):17992–17994, June 1995.

[50] Jaesun Lee, N.C. Giles, D. Rajavel, and C.J. Summers. Room-temperaure band-edge photoluminescence from cadmium telluride. *Phys. Rev. B*, **49**(3), August 1994.

[51] A. Nakamura, D. Paget, C. Hermann, C. Weisbuch, G. Lampel, and B.C. Cavenett. Optical detection of electron spin resonance in CdTe. *Solid State Commun.*, **30**(7):411–414, 1979.

[52] B. Kuhn-Heinrich, W. Ossau, H. Heinke, F. Fischer, T. Litz, A. Waag, and G. Landwehr. Optical investigation of confinement and strain effects in CdTe/(CdMg)Te quantum wells. *Appl. Phys. Lett.*, **63**(21), November 1993.

[53] J. M. Rowe, R. M. Nicklow, D. L. Price, and K. Zanio. Lattice dynamics of cadmium telluride. *Phys. Rev. B*, **10**(2):671–675, July 1974.

[54] S. Venugopalan, A. Petrou, R. R. Galazka, A. K. Ramdas, and S. Rodriguez. Raman scattering by phonons and magnons in semimagnetic semiconductors: $Cd_{1-x}Mn_xTe$. *Phys. Rev. B*, **25**(4):2681–2696, February 1982.

[55] S. Blundell. *Magnetism in condensed matter.* Oxford university press, 2001.

[56] C.P. Slichter. *Principles of magnetic resonance.* Solid-state sciences. Springer-Verlag, 1989.

[57] A. Abragam and B. Bleaney. *Electron Paramagnetic Resonance of Transition Metal Ions.* Oxford University Press, 1970.

[58] J.M. Spaeth and H. Overhof. *Point defects in semiconductors and insulators.* Springer, 2003.

[59] F. Bloch. Nuclear induction. *Phys. Rev.*, **70**(7-8):460–474, October 1946.

[60] R. Romestain, S. Geschwind, G. E. Devlin, and P. A. Wolff. Raman scattering from coherent spin states in n-type CdS. *Phys. Rev. Lett.*, 33(1):10–14, Jul 1974.

[61] S. Geschwind and R. Romestain. *High resolution spin-flip Raman scattering in CdS*, chapter 3, pages 151–201. Light scattering in solids VI. Springer-Verlag, 1984.

[62] S. J. Bingham, J.J. Davies, and D. Wolverson. High-resolution optical detection of electron spin resonance in eptaxial semiconductor layers by coherent Raman spectroscopy. *Phys. Rev. B.*, **65**(155301), March 2002.

[63] C.F. Klingshirm. *Semiconductor optics.* Springer-Verlag, 1995.

[64] M. Selders, E. Yi Chen, and R.K. Chang. Dispertion of Raman scattering in CdTe and InP below the absorption edge. *Solid State Commun.*, **12**:1057–1060, 1973.

[65] D.L. Peterson, D.U. Bartholomew, U. Debsha, A.K. Ramdas, and S. Rodriguez. Spin-flip Raman scattering in n-type diluted magnetic semiconductors. *Phys. Rev. B*, **32**(1), July 1985.

[66] A.k. Ramdas and S. Rodriguez. *Raman scattering in diluted magnetic semiconductors*, chapter 4, pages 137–206. Light scattering in solids VI. Springer-Verlag, 1991.

[67] A. Petrou, D.L. Peterson, S. Venugopalan, R.R. Galazka, A.K. Ramdas, and S. Rodriguez. Raman scattering study of the magnetic excitations in diluted magnetic semiconductors in the presence of an external magnetic field. *Phys. Rev. B*, **27**(6), March 1983.

[68] J. Stühler, M. Hirsch, G Schaak, and A. Waag. Raman spectroscopy of the paramagnetic spin flip in $Cd_{1-x}Mn_xTe$, the role of band-gap excitons as intermediate states, and optically detected electron-nuclear double resonance. *Phys. Rev. B*, **49**(11):7345–7356, March 1994.

[69] J. Puls and F. Henneberger. Interaction of localized excitons in semimagnetic quantum wells with manganese spin pairs. *J. Crys. Growth*, 214/215:432–435, 2000.

[70] S. Foner, Y. Shapira, D. Heiman, P. Becla, R. Kershaw, K. Dwight, and A. Wold. Magnetization steps in dilute magnetic semiconductors to 55 T: Mn^{2+} pair saturation in $Cd_{1-x}Mn_xTe$ and steps in $Zn_{1-x}Mn_xSe$, $Zn_{1-x}Mn_xTe$, and $Cd_{1-x}Mn_xSe$. *Phys. Rev. B*, **39**(16):11793–11799, June 1989.

[71] L.C. Smith, S.J. Bingham, J.J. Davies, and D. Wolverson. Electron paramagnetic resonance of manganese ions in CdTe detected by coherent Raman spectroscopy. *Appl. Phys. Lett.*, **87**(202101), November 2005.

[72] L.C. Smith, D. Wolverson, S.J. Bingham, and J.J. Davies. Electron paramagnetic resonance of Mn^{2+} ions in CdTe detected by coherent Raman spectroscopy. *Phys. stat. sol. (b)*, **243**(4):892–896, March 2006.

[73] Y. Tanabe and S. Sugano. On the absorption spectra of complex ions II. *J. Phys. Soc. Japan*, **9**:753–766, 1954.

[74] J.S. Griffith. *The theory of transition-metal ions.* Cambridge University Press, 1961.

[75] J. Lambe and C. Kikuchi. Paramagnetic resonance of CdTe : Mn and CdS : Mn*. *Phys. Rev.*, **114**(4):1256–1260, August 1960.

[76] D. Wolverson, L.C. Smith, S.J. Bingham, and J.J. Davies. Excitonic states of ZnSe detected by microwave-modulated reflectivity. *Phys. stat. sol. (b)*, **243**(4):897–901, February 2006.

[77] M.L. Sadowski, M. Byszewski, and M. Potemski. Optical detection of electron paramagnetic resonance in CdMnTe single quantum wells. *Appl. Phys. Lett.*, **82**(21):3719–3721, May 2003.

[78] S. Zeng, L.C. Smith, J.J. Davies, D. Wolverson, S.J. Bingham, and G.N. Aliev. Optically detected electron spin-flip resonance in CdMnTe. *phys. stat. sol. (b)*, **243**(4):887–891, February 2006.

[79] J. S. Blakemore. Semiconducting and other major properties of gallium arsenide. *J. Appl. Phys.*, **53**:R123–R181, May 1982.

[80] Sadao Adachi. GaAs, AlAs, and $Al_xGa_{1-x}As$: Material parameters for use in research and device applications. *J. Appl. Phys.*, **58**:R1–R29, April 1985.

[81] S. B. Nam, D. C. Reynolds, C. W. Litton, R. J. Almassy, T. C. Collins, and C. M. Wolfe. Free-exciton energy spectrum in GaAs. *Phys. Rev. B*, **13**(2):761–767, January 1976.

[82] D. D. Sell. Resolved free-exciton transitions in the optical-absorption spectrum of GaAs. *Phys. Rev. B*, **6**(10):3750–3753, November 1972.

[83] CT Foxon, RP Campion, KW Edmonds, L. Zhao, K. Wang, NRS Farley, CR Staddon, and BL Gallagher. The growth of high quality GaMnAs films by MBE. *Journal of Materials Science: Materials in Electronics*, **15**(11):727–731, 2005.

[84] S. Ye, PJ Klar, T. Henning, M. Lampalzer, W. Stolz, and W. Heimbrodt. Influence of codoping on the magnetoresistance of paramagnetic (Ga, Mn) As. *Journal of Superconductivity*, **16**(1):159–162, 2003.

[85] M. Tanaka. Ferromagnet (MnAs)/IIIV semiconductor hybrid structures. *Semicond. Sci. Technol.*, **17**:327–341, March 2002.

[86] F. Matsukura, H. Ohno, A. Shen, and Y. Sugawara. Transport properties and origin of ferromagnetism in (Ga,Mn)As. *Phys. Rev. B*, **57**(4):R2037–R2040, January 1998.

[87] H. Ohno. Making nonmagnetic semiconductors ferromagnetic. *Science*, **281**(5379):951–956, 1998.

[88] T. Hartmann, M. Lampalzer, W. Stolz, K. Megges, J. Lorberth, PJ Klar, and W. Heimbrodt. Optical characterisation of MOVPE-grown

$Ga_{1-x}Mn_xAs$ semimagnetic semiconductor layers. *Thin Solid Films*, 364(1-2):209–212, 2000.

[89] T. Hartmann, S. Ye, T. Henning, PJ Klar, M. Lampalzer, W. Stolz, and W. Heimbrodt. Magneto-optical spectroscopy on (Ga, Mn) As based layers—correlation between the p–d exchange integral and doping. *Journal of Superconductivity*, **16**(2):423–426, 2003.

[90] J. Szczytko, W. Mac, A. Twardowski, F. Matsukura, and H. Ohno. Antiferromagnetic $p-d$ exchange in ferromagnetic $Ga_{1-x}Mn_xAs$ epilayers. *Phys. Rev. B*, **59**(20):12935–12939, May 1999.

[91] J. Blinowski and P. Kacman. Spin interactions of interstitial Mn ions in ferromagnetic GaMnAs. *Phys. Rev. B*, **67**(12):121204, 2003.

[92] T. Hartmann, S. Ye, PJ Klar, W. Heimbrodt, M. Lampalzer, W. Stolz, T. Kurz, A. Loidl, H.A. Krug von Nidda, D. Wolverson, et al. Tuning of the average *p-d* exchange in (Ga, Mn) As by modification of the Mn electronic structure. *Phys. Rev. B*, **70**(23):233201, 2004.

[93] W. Heimbrodt, T. Hartmann, PJ Klar, M. Lampalzer, W. Stolz, K. Volz, A. Schaper, W. Treutmann, H.A.K. von Nidda, A. Loidl, et al. Monitoring the sign reversal of the valence band exchange integral in (Ga, Mn) As. *Physica E: Low-dimensional Systems and Nanostructures*, **10**(1-3):175–180, 2001.

[94] Y. Satoh, D. Okazawa, A. Nagashima, and J. Yoshino. Carrier concentration dependence of electronic and magnetic properties of Sn-doped GaMnAs. *Physica E: Low-dimensional Systems and Nanostructures*, **10**(1-3):196–200, 2001.

[95] Y. Chen, B. Gil, P. Lefebvre, and H. Mathieu. Exchange effects on excitons in quantum wells. *Phys. Rev. B*, **37**(11):6429–6432, April 1988.

[96] M. Altarelli and Nunzio O. Lipari. Perturbation-theory investigation of the exciton ground state of cubic semiconductors in a magnetic field. *Phys. Rev. B*, **7**(8):3798–3802, April 1973.

[97] P. Lawaetz. Valence-band parameters in cubic semiconductors. *Phys. Rev. B*, **4**(10):3460–3467, November 1971.

[98] G. Ambrazevicius, M. Cardona, and R. Merlin. Resonant Raman scattering by phonons in a strong magnetic field: GaAs. *Phys. Rev. Lett.*, **59**(6):700–703, August 1987.

[99] Claude Weisbuch and Claudine Hermann. Optical detection of conduction-electron spin resonance in GaAs, $Ga_{1-x}In_xAs$, and $Ga_{1-x}Al_xAs$. *Phys. Rev. B*, **15**(2):816–822, January 1977.

[100] M. Reine, R. L. Aggarwal, B. Lax, and C. M. Wolfe. Split-off valence-band parameters for GaAs from stress-modulated magnetoreflectivity. *Phys. Rev. B*, **2**(2):458–463, July 1970.

[101] M. Reine, R. L. Aggarwal, and B. Lax. Stress-modulated magnetoreflectivity of gallium antimonide and gallium arsenide. *Phys. Rev. B*, **5**(8):3033–3049, April 1972.

[102] Laura M. Roth, Benjamin Lax, and Solomon Zwerdling. Theory of optical magneto-absorption effects in semiconductors. *Phys. Rev.*, **114**(1):90, April 1959.

[103] E. Burstein, G. S. Picus, R. F. Wallis, and F. Blatt. Zeeman-type magneto-optical studies of interband transitions in semiconductors. *Phys. Rev.*, **113**(1):15–33, January 1959.

[104] D.L. Rode. *Transport phenomena*, volume 10 of *Semiconductors and semimetals*. Academic Press, 1975.

[105] Gerald Bastard. *Wave mechanics applied to semiconductor heterostructures*. Les Editions de Physique and Halsted Press, 1988.

[106] S. Maćkowski, E. Janik, F. Kyrychenko, and J. Kossut. Magnetooptical properties of CdTe quantum well structures with quaternary CdMnMgTe barriers. *Semicond. Sci. Technol.*, **14**:979–983, August 1999.

[107] J. Stühler, G. Schaack, M. Dahl, A. Waag, G. Landwehr, K. V. Kavokin, and I. A. Merkulov. Multiple Mn^{2+}-spin-flip Raman scattering at high fields via magnetic polaron states in semimagnetic quantum wells. *Phys. Rev. Lett.*, **74**(13):2567–2570, March 1995.

[108] Jiming Bao, Andrea V. Bragas, Jacek K. Furdyna, and Roberto Merlin. Optically induced multispin entanglement in a semiconductor quantum well. *Nature Materials*, **2**:175–179, March 2003.

[109] M. Byszewski, D. Plantier, M.L. Sadowski, M. Potemski, A. Sachrajda, Z. Wilamowski, and G. Karczewski. Optical studies of Mn^{2+} spin resonance in (Cd,Mn)Te quantum wells. *Physica E*, **22**:652–655, 2004.

[110] D. Suisky, W. Heimbrodt, C. Santos, F. Neugebauer, M. Happ, B. Lunn, J. E. Nicholls, and D. E. Ashenford. Anisotropic Zeeman splitting in semimagnetic quantum-well structures. *Phys. Rev. B*, **58**(7):3969–3976, August 1998.

[111] J. Singh. *The physics of semiconductors and their heterostructures.* McGraw-Hill, 1193.

[112] J. Stühler, G. Schaack, M. Dahl, A. Waag, G. Landwehr, K. V. Kavokin, and I. A. Merkulov. Polarization properties of multiple Mn^{2+}-spin-flip Raman scattering in semimagnetic quantum wells. *J. Cryst. Growth*, **159**:1001–1004, 1996.

[113] K. V. Kavokin and I. A. Merkulov. Multispin Raman paramagnetic resonance: Quantum dynamics of classically large angular momenta. *Phys. Rev. B*, **55**(12):R7371–R7374, March 1997.

[114] M. Nirmal, D. J. Norris, M. Kuno, M. G. Bawendi, Al. L. Efros, and M. Rosen. Observation of the "dark exciton" in CdSe quantum dots. *Phys. Rev. Lett.*, **75**(20):3728–3731, November 1995.

[115] R. Meyer, M. Dahl, G. Schaack, and A. Waag. Spin-flip Raman scattering from donor-bound electrons in $Cd_{1-x}Mn_xTe/Cd_{1-y}Mg_yTe$ single quantum wells. *Phys. Rev. B*, **55**(24):16376–16384, June 1997.

[116] A. A. Sirenko, V. I. Belitsky, T. Ruf, M. Cardona, A. I. Ekimov, and C. Trallero-Giner. Spin-flip and acoustic-phonon raman scattering in CdS nanocrystals. *Phys. Rev. B*, **58**(4):2077–2087, July 1998.

[117] S.L. Song, N.F. Chen, J.P. Zhou, YL Li, C.L. Chai, S.Y. Yang, and Z.K. Liu. (Ga, Gd, As) film growth on GaAs substrate by low-energy ion-beam deposit. *Journal of Crystal Growth*, **260**(3):451–455, 2004.

[118] P.Y. Yu and M. Cardona. *Fundermentals of semiconductors: physics and material properties.* Springer, 1996.

[119] Leonard I. Schiff. *Quantum mechanics.* McGraw-Hill, 3rd edition, 1968.

[120] F. Mandl. *Quantum mechanics.* John Wiley and Sons, 1996.

[121] C. Kittel. *Quantum theory of solids.* John Wiley and Sons, 2nd edition, 1987.

[122] Henry Mathieu, Pierre Lefebvre, and Philippe Christol. Simple analytical method for calculating exciton binding energies in semiconductor quantum wells. *Phys. Rev. B*, **46**(7):4092–4101, August 1992.

[123] Xing-Fei He. Excitons in anisotropic solids: The model of fractional-dimensional space. *Phys. Rev. B*, **43**(3):2063–2069, January 1991.